

DISS. ETH NO. 25571

# Colloidal Polymer Particles as Building Blocks for Functional Composite Materials

A thesis submitted to attain the degree of  
DOCTOR OF SCIENCES of ETH ZURICH  
(Dr. sc. ETH Zurich)

presented by

**Stefano Caimi**

Master of Science ETH in Chemical and Bioengineering  
born on 10.06.1991  
citizen of Italy

accepted on the recommendation of  
Prof. Dr. Massimo Morbidelli, ETH Zurich  
Prof. Dr. Mark Tibbitt, ETH Zurich

2018



*"Success is not the key to happiness, happiness is the key to success. If you love what you are doing, you will be successful"*

— Herman Cain.



*To my wife Elsa and my son Giorgio.*



# Abstract

Composites are a class of materials characterized by the simultaneous presence of two or more components, which, when properly combined, lead to a new product. As the different constituents can be selected so to meet specific needs, the range of possible applications of these materials is practically infinite. These include reinforcing structures for high-impact strength, lightweight and flexible components, and insulating materials, just to mention a few. However, the synthesis of functional composites is far from being straightforward. To target these applications, indeed, the materials have to be carefully chosen, specifically engineered and tailored designed. A variety of composite materials employs a polymer as one of the constituents. This is because of the versatility of this class of components, which may have positive/negative charge, soft/hard surfaces, brittle/elastic properties, hydrophobic/hydrophilic nature, *etc.*

This work starts from the synthesis of targeted polymeric dispersions to understand the aggregation phenomena occurring when polymers are subjected to intense shear during their processing. In particular, polystyrene-based nanoparticles are prepared and used as model system to study the kinetics of aggregation into a microchannel and to investigate the role of the physical and chemical properties of the particle surface in aggregation/breakage experiments under shear. More specifically, the aim of this first project is to elucidate the effect of the residence time into a microchannel (*i.e.*, the time during which the particles are subjected to in-

tense shear) on the conversion of the primary particles to clusters, the average size and compactness of the formed aggregates. In the second part of these fundamental studies, shear-induced aggregation experiments of polymer colloidal particles have been devised with the specific objective of highlighting material transfer and clarifying the role of the softness of the particle surface. To achieve this goal, polymer particles with a core-shell structure comprising fluorescent groups have been prepared so that the surface softness could be tuned by the addition of monomer acting as a plasticizer and the percentage of fluorescent particles could be recorded over time *via* confocal microscopy to detect possible material transfer among different particles. For the first time, material exchange occurring on the soft surface of core-shell polymer microparticles upon aggregation under shear was observed and proved.

Following these fundamental studies, this thesis focuses on the synthesis of a composite material made from a polymer (PVdF-HFP), a functional filler (silica), and an ionic liquid (Pyr13TFSI) to be assembled as a separator for lithium-ion batteries (LIBs). Indeed, LIBs are the key for modern electricity-based transportation systems and more generally for sustainable large-scale energy applications. However, typical commercial batteries seldom meet safety regulations because of the presence of organic, flammable, and volatile liquid electrolytes, and viable alternatives need to be found. Ionic liquids (ILs) are considered to be one of the most promising candidates, because of their low flammability, negligible vapor pressure, and low toxicity. However, the process to form freestanding IL-based separators is not straightforward. Therefore, in the first part of this project, a new methodology to form these membranes is presented and optimized, starting from the production of polymer clusters with a microchannel. In the second part, the performances of the IL-based separator are enhanced through a precise and controlled addition of the silica nanoparticles into the polymer matrix at the nanoscale level, which



contribute to increase the ionic conductivity of the membrane. The resulting electrochemical performances of the battery assembled with these separators were excellent not only at low but also at high current densities.

In the last part of the thesis, a composite material is prepared to improve the crack-resistance properties of existing commercial construction materials. In particular, redispersible powders based on soft core-hard shell polymer particles of styrene/2-ethylhexyl acrylate are prepared as additives for cement mortars. Different polymer latexes at high solid content with varied core-shell ratio, shell thickness and chemical composition (hardness) were prepared *via* semi-batch emulsion polymerization and spray dried to identify the optimal particle design which guarantees both good spray-ability and enhanced crack-bridging properties.



# Sommario

I compositi sono una classe di materiali caratterizzati dalla presenza simultanea di due o più componenti che, se opportunamente combinati, danno luogo ad un nuovo prodotto. Poiché i diversi componenti possono essere selezionati in base alle specifiche esigenze, la gamma di applicazioni possibili di questi materiali è praticamente infinita. Si tratta, ad esempio, di strutture di rinforzo ad alta resistenza agli urti, di componenti leggeri e flessibili, di materiali isolanti, solo per citarne alcuni. Tuttavia, la sintesi dei questi compositi funzionali è tutt'altro che semplice. Per essere impiegati, infatti, i materiali devono essere scelti con cura, appositamente disegnati e progettati su misura. Un numero sempre crescente di materiali compositi impiega un polimero come uno dei costituenti principali. Questa scelta è dovuta alla versatilità di questa classe di componenti, che possono avere carica positiva/negativa, superfici morbide/dure, proprietà fragili/elastiche, natura idrofobica/idrofila, *ecc.*

Questa tesi inizia dalla sintesi mirata di dispersioni polimeriche per comprendere i fenomeni di aggregazione che si verificano quando i polimeri sono sottoposti a sforzo intenso durante la loro lavorazione. In particolare, le nanoparticelle a base di polistirene vengono preparate e utilizzate come sistema modello per studiare la cinetica dell'aggregazione in microcanali e il ruolo delle proprietà fisiche e chimiche della superficie delle particelle in esperimenti di aggregazione/rottura sotto sforzo. Più precisamente, lo scopo di questo primo progetto è quello di chiarire l'effetto

del tempo di permanenza in un microcanale (ossia il tempo in cui le particelle sono soggette ad un intenso sforzo di taglio) sulla conversione delle particelle primarie in aggregati, e sulla loro dimensione media e compattezza. Nella seconda parte di questo studio fondamentale, sono stati eseguiti esperimenti di aggregazione indotta da sforzi di taglio di particelle polimeriche colloidali, con l'obiettivo specifico di evidenziare il trasferimento di materia e chiarire il ruolo della morbidezza della superficie della particella. Per raggiungere questo obiettivo, sono state preparate particelle polimeriche con una struttura a guscio che comprende gruppi fluorescenti in modo che la morbidezza superficiale possa essere regolata dall'aggiunta di monomero, che funge da plastificante, e che la percentuale di particelle fluorescenti possa essere registrata nel tempo attraverso microscopia confocale, per rilevare possibili trasferimenti di materiale tra le diverse particelle. Per la prima volta, è stato osservato e dimostrato lo scambio di materia tra la superficie morbida di microparticelle polimeriche con struttura a guscio durante l'aggregazione sotto sforzo.

A seguito di questi studi di base, questa tesi si concentra sulla sintesi di un materiale composito costituito da un polimero (PVdF-HFP), un filler funzionale (silice) e un liquido ionico (Pyr13TFSI) da assemblare come separatore per batterie agli ioni di litio (BIL). Le BIL sono infatti la chiave per i moderni sistemi elettrici di trasporto e, più in generale, per applicazioni energetiche sostenibili di massa. Tuttavia, le tipiche batterie commerciali raramente soddisfano le norme di sicurezza a causa della presenza di elettroliti liquidi organici, che sono infiammabili e volatili, e per questo motivo è necessario trovare valide alternative. I liquidi ionici (LI) sono considerati uno dei candidati più promettenti, grazie alla loro bassa infiammabilità, una pressione di vapore trascurabile e una bassa tossicità. Tuttavia, il processo di formazione di separatori basati su LI non è semplice. Pertanto, nella prima parte di questo progetto viene presentato e ottimizzato un nuovo metodo

per la formazione di queste membrane, a partire dalla produzione di aggregati di polimero prodotti attraverso un microcanale. Nella seconda parte, le prestazioni del separatore a base di LI sono migliorate attraverso una precisa e controllata aggiunta delle nanoparticelle di silice nella matrice polimerica a livello di nanoscala, le quali contribuiscono ad aumentare la conducibilità ionica della membrana. Le prestazioni elettrochimiche della batteria assemblata con questi separatori sono risultate eccellenti non solo a bassa ma anche ad alta densità di corrente.

Nell'ultima parte della tesi viene preparato un materiale composito per migliorare le proprietà di resistenza alla frattura dei materiali da costruzione commerciali esistenti. In particolare, sono state preparate polveri ridispersibili a base di particelle polimeriche a guscio morbido e duro prodotte a partire da stirene e 2-etilesil acrilato, come additivi per malte cementizie. Sono stati sintetizzati diversi lattici polimerici ad alto contenuto solido con diversi rapporti nucleo-guscio, spessore e composizione chimica (durezza) del guscio, attraverso polimerizzazione semi-continua in emulsione. I lattici ottenuti sono stati seccati mediante atomizzazione per identificare la morfologia ottimale delle particelle in grado di garantire sia una buona polvere risultante sia ottime proprietà di resistenza alla frattura.



# Acknowledgments

I would like to express my gratitude towards the following people who have provided me with invaluable help, support and advice throughout this thesis.

First and foremost, I wish to express my sincere gratitude to Prof. Massimo Morbidelli who offered me the opportunity to pursue a doctoral work in his research group and for trusting me in all challenging situations.

I am extremely grateful to Prof. Giuseppe Storti and Dr. Hua Wu for being my supervisors and mentors throughout these years and for their constant support.

I want to thank Prof. Mark Tibbitt for accepting to be my co-examiner, for his availability and comprehension.

Many thanks to my industrial collaborators, and in particular to Dr. Christine Hamon (Solvay), Dr. Riccardo Pieri (Solvay), Dr. Roger Zurbruggen (AkzoNobel), Livio Hegglin (AkzoNobel) and Dr. Raffael La Fauci (EWZ).

Special thanks go to Alberto, Baptiste and Antoine for collaborating with me in countless challenging circumstances and for their invaluable scientific discussions and expertise.

The constant support and advice from Prof. Marco Lattuada and Prof. Paolo

Arosio are highly appreciated.

My gratitude should also be expressed to Ernesto, Ruben, Gabriele, Gioele, Isabella, Jakub and Guido for the pleasant time spent in the lab and outside of it. I am also deeply thankful to Navanshu, Dario, Elias and Michela who worked with me during their theses and research projects. Without their help and ideas, it would have been impossible to work on all these projects at the same time.

Many thanks the whole team of the Morbidelli Group for having made this thesis an enjoyable and pleasant experience.

Finally, I wish to truly thank my parents for their unending support and encouragements throughout my studies and my wife Elsa for always loving me and for having given me the most treasured gift, Giorgio.



# Contents

	Page
Abstract	I
Sommario	V
Acknowledgments	IX
Abbreviations	XVII
Symbols	XIX
List of figures	XXI
List of tables	XXV
<b>1 Introduction</b>	<b>1</b>
1.1 Colloids: definition and properties . . . . .	2
1.2 Polymer latexes: synthesis and applications . . . . .	7
1.3 Composite materials . . . . .	10
1.4 Scope of the thesis . . . . .	11
<b>2 Aggregation of Stable Colloidal Dispersions under Short High-Shear Conditions</b>	<b>13</b>

<b>3</b>	<b>Tracking of Fluorescently Labeled Polymer Particles Reveals Surface Effects during Shear-Controlled Aggregation</b>	<b>27</b>
3.1	Introduction . . . . .	28
3.2	Experimental . . . . .	31
3.2.1	Materials . . . . .	31
3.2.2	Synthesis of colloidal core-shell polymer nanoparticles . . . . .	31
3.2.3	Synthesis and purification of rhodamine B - HEMA precursor	35
3.2.4	Synthesis of core-shell polymer microparticles . . . . .	35
3.2.5	Processing of the particles . . . . .	37
3.2.6	Characterization methods . . . . .	38
3.3	Results and Discussion . . . . .	41
3.3.1	Shear-controlled aggregation . . . . .	41
3.3.2	Aggregation of nanoparticles . . . . .	42
3.3.3	Aggregation of microparticles . . . . .	44
3.4	Conclusion . . . . .	49
 <b>4</b>	 <b>PVdF-HFP and Ionic-Liquid-Based, Freestanding Thin Separator for Lithium-Ion Batteries</b>	 <b>51</b>
4.1	Introduction . . . . .	52
4.2	Experimental . . . . .	55
4.2.1	Materials . . . . .	55
4.2.2	Methods . . . . .	56
4.3	Results and Discussion . . . . .	59
4.3.1	Preparation of the PCIL membranes . . . . .	59
4.3.2	Electrochemical characterization of the PCIL membranes . . . . .	64
4.4	Conclusion . . . . .	74

<b>5</b>	<b>Effect of SiO<sub>2</sub> Nanoparticles on the Performance of PVdF-HFP/Ionic Liquid Separator for Lithium-Ion Batteries</b>	<b>77</b>
5.1	Introduction . . . . .	78
5.2	Experimental . . . . .	80
5.2.1	Materials . . . . .	80
5.2.2	Methods . . . . .	80
5.3	Results and Discussion . . . . .	83
5.3.1	Preparation of the PSiCIL membranes . . . . .	83
5.3.2	Electrochemical characterization of the PSiCIL membranes . . . . .	90
5.4	Conclusion . . . . .	94
<b>6</b>	<b>Core-Shell Morphology of Redispersible Powders in Polymer-Cement Waterproof Mortars</b>	<b>97</b>
6.1	Introduction . . . . .	98
6.2	Experimental . . . . .	101
6.2.1	Materials . . . . .	101
6.2.2	Syntheses . . . . .	101
6.2.3	Characterization of polymer dispersions . . . . .	102
6.2.4	Spray drying . . . . .	103
6.2.5	Polymer-cement mortars . . . . .	104
6.2.6	Crack-bridging ability of the polymer-cement mortar . . . . .	104
6.3	Results and Discussion . . . . .	105
6.3.1	Synthesis of core-shell polymer nanoparticles . . . . .	105
6.3.2	Spray drying and redispersibility . . . . .	111
6.3.3	Crack-bridging and polymer-cement compatibility . . . . .	115
6.4	Conclusion . . . . .	118
<b>7</b>	<b>Conclusions and outlook</b>	<b>121</b>

<b>8</b>	<b>Appendix</b>	<b>127</b>
8.1	Aggregation of Stable Colloidal Dispersions under Short High-Shear Conditions . . . . .	128
8.1.1	Synthesis and characterization of the polystyrene nanoparticles	128
8.1.2	Manufacturing of the quartz microchannels . . . . .	128
8.1.3	Measurement of degree of aggregation and morphology of clusters . . . . .	129
8.1.4	Evaluation of the average distance between two neighbor free NPs . . . . .	131
8.1.5	Details on the computational fluid dynamic simulations . . .	132
8.2	PVdF-HFP and Ionic Liquid-Based, Freestanding Thin Separator for Lithium-Ion Batteries . . . . .	134
8.2.1	Properties of the aqueous dispersion of PVdF-HFP NPs . .	134
8.2.2	DSC results . . . . .	135
8.2.3	Morphology of the PCIL membrane prepared at PC/IL = 20/80 . . . . .	136
8.3	Effect of SiO <sub>2</sub> Nanoparticles on the Performance of PVdF-HFP/Ionic liquid Separator for Lithium-Ion Batteries . . . . .	137
8.3.1	Ionic conductivity results . . . . .	137
8.4	Core-Shell Morphology of Redispersible Powders in Polymer-Cement Waterproof Mortars . . . . .	138
8.4.1	Syntheses conditions . . . . .	138
8.4.2	Syntheses results . . . . .	141
8.4.3	Polymer-cement membranes . . . . .	142
8.4.4	NMR results and evaluation . . . . .	142
	<b>Bibliography</b>	<b>145</b>

## CONTENTS

---

<b>Curriculum Vitae</b>	<b>163</b>
<b>List of publications</b>	<b>165</b>
<b>Conference and Poster proceedings</b>	<b>167</b>



# Abbreviations

Abbreviation	Description
AIBN	Azobis(isobutyro-nitrile)
ccc	Critical coagulation concentration
CF	Core feed
DCC	Dicyclohexylcarbodiimide
DCM	Dichloromethane
DLCA	Diffusion Limited Cluster Aggregation
DLS	Dynamic light scattering
DMAP	4-(di-methylamino)-pyridine
DMC	Dimethyl carbonate
DSC	Differential scanning calorimetry
DVB	Divinylbenzene
DZ-MC	Double Z-shape microchannel
EC	Ethylene carbonate
2-EHA	2-Ethylhexyl acrylate
ESW	Electrochemical stability window
GPE	Gel-polymer membrane
HEMA	2-hydroxyethyl methacrylate
IC	Initial conditions
IF	Initiator feed
IL	Ionic liquid
IS	Initiator solution
KPS	Potassium peroxydisulfate
LFP	LiFePO <sub>4</sub>
LIB	Lithium-ion battery
LiPF <sub>6</sub>	Lithium hexafluorophosphate
LiTFSI	Bis(trifluoromethane)-sulfonamide lithium salt
MAPTAC	[3-(Methacryloylamino)propyl]trimethylammonium chloride

NMR	Nuclear magnetic resonance
NP	Nanoparticle
PC	Polymer clusters
PCIL	Polymer clusters impregnated with ionic liquid
PCM	Polymer-cement mortars
PDI	Polydispersity index
PSiC	Polymer-silica clusters
PSiCIL	Polymer-silica clusters impregnated with ionic liquid
PVA	Poly(vinyl alcohol)
PVdF-HFP	Poly(vinylidene fluoride- <i>co</i> -hexafluoro propylene)
PVP	Poly vinylpyrrolidone 40k MW
Pyr13TFSI	N-Propyl-N-Methylpyrrolidinium bis(trifluoromethane sulfonyl)-imide
RhB	Rhodamine B
RLCA	Reaction Limited Cluster Aggregation
RPP	Redispersible polymer powder
SALS	Small-angle light scattering
SDS	Sodium dodecyl sulfate
SF	Shell feed
STY	Styrene
SZ-MC	Single Z-shape microchannel
TGA	Thermal gravimetric analysis
VOC	Volatile organic compound
WT	Waiting time
XRD	X-ray powder diffraction
Z-MC	Z-shape microchannel



# Symbols

Symbol	Units	Description
$a$	m	Particle radius
$a_0$	m	Bohr radius
$\alpha_P$	C m <sup>2</sup> V <sup>-1</sup>	Polarizability
$C$	A m <sup>-2</sup>	Current density
$d$	m	Thickness
$d_f$	-	Fractal dimension
$D_{ss}$	m	Average distance between the surface of two neighbor free NPs
$\Delta H_m$	J g <sup>-1</sup>	Enthalpy of melting
$e$	C	Electron charge
$E_a$	J	Activation energy
$\epsilon$	V s A <sup>-1</sup> m <sup>-1</sup>	Vacuum dielectric permeability
$\dot{\gamma}$	s <sup>-1</sup>	Shear rate
$I(0)$	-	Scattering intensity at zero angle
$I(q)$	-	Angle-dependent scattering intensity
$k$	L mol <sup>-1</sup> s <sup>-1</sup>	Rate constant
$k_0$	L mol <sup>-1</sup> s <sup>-1</sup>	Pre-exponential factor
$k_B$	J K <sup>-1</sup>	Boltzmann constant
$k_f$	-	Scaling prefactor
$\kappa$	m <sup>-1</sup>	Debye length
$\lambda$	m	Wavelength
$M$	mol L <sup>-1</sup>	Molarity
$\mu$	Pa s	Viscosity
$\mu_t$	Pa s	Turbulent viscosity
$n_0$	m <sup>-3</sup>	Number ion concentration
$n_w$	-	Water refractive index
$N_P$	molec L <sup>-1</sup>	Number concentration of the particles
$N_C$	-	Number of clusters

$N_{P,C}$	-	Number of particles in a cluster
$\langle P \rangle$	bar	Reynolds-averaged pressure
$P(q)$	-	Primary particles form factor
$\phi$	%	Volume fraction
$\Phi$	%	Porosity
$q$	-	Magnitude of the scattering wave vector
$r$	m	Particle distance
$R$	J K <sup>-1</sup> mol <sup>-1</sup>	Gas constant
$R_g$	m	Radius of gyration
$R_b$	$\Omega$	Bulk resistance
$\rho$	g mL <sup>-1</sup>	Density
$\sigma$	S m <sup>-1</sup>	Ionic conductivity
$S$	m <sup>2</sup>	Area of the electrode
$\langle S(q) \rangle$	-	Average structure factor
$t_r$	s	Residence time
$T$	K	Temperature
$T_C$	K	Crystallization temperature
$T_d$	K	Decomposition temperature
$T_g$	K	Glass transition temperature
$T_m$	K	Melting temperature
$\theta$	rad	Scattering angle
$\langle U_i \rangle$	-	Reynolds-averaged velocity component in the $i^{th}$ direction
$U_{max}$	V	Maximum of the interaction potential
$v$	m s <sup>-1</sup>	Velocity
$v_m$	m s <sup>-1</sup>	Mean velocity
$V_A$	V	Potential energy of attraction
$V_P$	m <sup>3</sup>	Particle volume
$V_R$	V	Potential energy of repulsion
$V_T$	V	Total interaction potential
$w$	-	Weight fraction
$W$	-	Fuchs stability ratio
$X_C$	%	Cristallinity
$\chi$	%	Conversion
$z$	-	Ion valence

# List of Figures

1.1	Total interaction potential acting among two approaching nanoparticles, according to the DLVO theory. . . . .	4
1.2	Scheme of step (left) and chain (right) polymerization. . . . .	7
1.3	Schematic representation of a random, an alternating, a block, and a nonlinear graft copolymers. . . . .	9
2.1	Schematic representation of colloidal interactions and relative position between two NPs and average distance between free NPs as a function of the conversion to large clusters. . . . .	23
2.2	Specific dimension of the SZ-MC and DZ-MC, mean velocity of water in the SZ-MC and DZ-MC as a function of the pressure drop (P/L), holder of the MCs and the setup of the shear-driven aggregation device. . . . .	24
2.3	Conversion, gyration radius, and mass fractal dimension of the clusters as a function of the cumulative residence time, at different mean velocities of the dispersion in the SZ-MC and DZ-MC. . . . .	25
3.1	Time evolution of the average cluster size and fractal dimension of swollen nanoparticles. . . . .	42
3.2	SEM pictures of the microparticles with and without shell. . . . .	45
3.3	Micrographs of the microparticles <i>via</i> confocal microscopy in transmission mode, in fluorescent confocal mode and their superposition. . . . .	45

3.4	Time evolution of the average cluster size and fractal dimension of swollen microparticles. . . . .	48
3.5	Evolution in time of the percentage of fluorescence for swollen and non-swollen microparticles. . . . .	49
4.1	Structure of the ionic liquid, Pyr13TFSI. . . . .	55
4.2	SALS measurement of the clusters from the microchannel and SEM image of the dried PC. . . . .	60
4.3	Freestanding, transparent, 50 $\mu\text{m}$ thick PCIL membrane formed <i>via</i> hot-pressing. . . . .	61
4.4	TGA profiles of PVdF-HFP, LiTFSI-Pyr13TFSI, PCIL membrane at PC/IL = 30/70 and conventional organic electrolyte. . . . .	63
4.5	SEM image of the cross-section of the PCIL membrane prepared at PC/IL = 30/70, after removal of the IL solution with DCM. . . . .	65
4.6	Ionic conductivity of the PCIL membrane treated and fitted with the linearized VTF equation. . . . .	67
4.7	Normalized discharge capacity for the assembled Li/PCIL/LFP cells with the PCIL membrane at PC/IL = 40/60, 35/65, and 30/70. . . . .	68
4.8	Specific discharge capacity and electrochemical efficiency for the assembled Li/PCIL/LFP cell with the PCIL membrane at PC/IL = 30/70. . . . .	69
4.9	Specific discharge capacity and Coulombic efficiency as a function of cycle number for the assembled Li/PCIL/LFP cell with the PCIL membrane at PC/IL = 30/70. . . . .	73
5.1	Average diameter and zeta potential of the silica NPs and TEM image of the dried NPs. . . . .	84

5.2	SEM picture of the silica NPs entrapped in the polymer matrix after a single pass through the microchannel. . . . .	85
5.3	DSC of the composite gel obtained after one pass through the microchannel at different percentages of the fillers, silica NPs. . . . .	87
5.4	XRD of the composite gel obtained after one pass through the microchannel at different percentages of the fillers, silica NPs. . . . .	89
5.5	Ionic conductivity at 25, 40, 55, 70 and 80 °C of the PSiCIL membranes containing 70 wt.% of IL and 0%, 5%, 10%, and 15% of SiO <sub>2</sub> , respectively. . . . .	91
5.6	Discharge capacity, normalized with respect to the initial cycle at 0.1C, at 60 °C of the PSiCIL membranes containing 70 wt.% of IL with 0% and 10% of SiO <sub>2</sub> , respectively. . . . .	93
6.1	Morphologies of the different synthesized core-shell polymer nanoparticles. . . . .	106
6.2	Instantaneous and cumulative conversion, and average particle size during the synthesis of sample <i>a</i> . . . . .	108
6.3	Mass fraction of 2-EHA in the polymer particles for sample <i>a</i> during the reaction. . . . .	109
6.4	DSC curves of polymer <i>a</i> . . . . .	111
6.5	Sample <i>i</i> and sample <i>d</i> after spray drying. . . . .	113
6.6	Powders <i>i</i> and <i>d</i> redispersed after spray drying. . . . .	115
6.7	The expansion in millimeters before the membrane cracks at different temperatures. . . . .	117
8.1	Microscopic image of the CS of the closed microchannel after thermal bonding of two structured wafers. . . . .	129

8.2	Microscopic image of the surface at the microfluidic channel bottom after the etch process. . . . .	130
8.3	DSC heating and cooling curves of PVdF-HFP. . . . .	135
8.4	Morphology of the PCIL membrane prepared at PC/IL = 20/80. . .	136
8.5	Number of polymer particles in the reactor during the synthesis of sample <i>a</i> . . . . .	140
8.6	Sketch of the membrane preparation procedure for crack-bridging tests. . . . .	142
8.7	Cement-based membrane obtained with polymer <i>h</i> (left) and <i>i</i> (right), after spray drying. . . . .	142
8.8	NMR spectra for the monomers STY (black curve) and 2-EHA (red curve) and for the copolymer STY/2-EHA <i>a</i> (green curve). . . . .	144

# List of Tables

3.1	Recipe for the synthesis of the core of the nanoparticles. . . . .	33
3.2	Recipe for the synthesis of the shell of the nanoparticles. . . . .	34
4.1	Ionic conductivities of the PCIL membrane at the PC/IL ratio of 30/70. . . . .	66
5.1	Properties of the dispersion of SiO <sub>2</sub> NPs in water. . . . .	83
5.2	Properties of the dispersion of SiO <sub>2</sub> NPs in water. . . . .	86
6.1	Final size, PDI (polydispersity index) and glass transition temperature ( $T_g$ ) of the different polymer particles. . . . .	108
6.2	Results of the visual analysis of the spray dried polymer latexes. Qualitative grain sizes range from fine over medium to coarse powder. The samples are also classified in free-flowing and caking powders. Their redispersibility in water ranges from good, to medium and to bad. . . . .	113
8.1	Physical and chemical properties of the aqueous dispersion of PVdF-HFP NPs. . . . .	134
8.2	Physical and chemical properties of the aqueous dispersion of PVdF-HFP NPs. . . . .	135
8.3	Ionic conductivity of the PSiCIL membranes in the temperature range from 25 to 80 °C at different percentages of silica. . . . .	137

8.4	Reaction formulations for different core-shell particles for samples <i>a-e</i> . All reactions were run at 80 °C with a stirring speed of 200 rpm.	138
8.5	Reaction formulations for different core-shell particles for samples <i>f-j</i> . All reactions were run at 80 °C with a stirring speed of 200 rpm.	139
8.6	Surface zeta potential, pH value and film-forming ability of the synthesized latexes. . . . .	141
8.7	2-EHA mass content of the cumulative polymer particles during the reaction. . . . .	143



# Chapter 1

## Introduction

## 1.1 Colloids: definition and properties

A colloid is defined as a heterogeneous mixture of two or more substances, in which one component is uniformly dispersed and suspended throughout the other phases at the nanoscale level. As the average size of colloidal particles typically ranges from 1 nm to 1  $\mu\text{m}$ , these dispersions exhibit peculiar physical and chemical properties, [1, 2] which find applications in very diverse sectors, including plastics production, photovoltaics and medical uses. [3–8] As it is not possible to overcome the principles of thermodynamics, any colloidal dispersion eventually coagulates and turns into a bulk phase. However, if the nanoparticles possess strong enough repulsive forces, which limit aggregation, these systems can remain dispersed even for years. A colloid can therefore be defined as a kinetically stable suspension.

The forces acting among colloidal nanoparticles can be divided in van der Waals, Born and electrostatic contributions. The first ones are attractive, strong and occurring at short-range and the numerical expression for the potential energy of attraction under limiting conditions has been derived by Hamaker [9] starting from the general expression:

$$V_A = -\frac{\alpha_P a_0^2 e^2}{(4\pi\epsilon_0)^2} \int_{V_1} \int_{V_2} \frac{dV_1 dV_2}{r^6} \quad (1.1)$$

where  $a_0$  is the Bohr radius,  $e$  is the electron charge,  $\alpha_P$  is the polarizability of the second atom,  $\epsilon$  is the vacuum dielectric permeability, and  $r$  is the distance. The electrostatic forces, on the other hand, are long-range and repulsive and, in the literature, there are various relations to describe the potential energy of repulsion, depending on the assumptions taken. For example:

$$V_R = \frac{32n_0 k_B T}{\kappa} z^2 [1 - \tanh(0.5\kappa r)] \quad (1.2)$$

where  $n_0$  is the number concentration of ions in bulk,  $k_B$  is the Boltzmann constant,  $T$  is the temperature,  $\kappa$  is the inverse of the thickness of the electrical double layer,  $z$  is the valence of the ion and  $r$  is the distance between the particles.

Born forces originate from the fact that atoms have a finite size and cannot interpenetrate each other and therefore repulsive electron-electron and nucleus-nucleus interactions occur at very short-range. The contribution of all these forces was described by Derjaguin and Landau [10] as well as by Verwey and Overbeek [11] in the so-called, after their initials, DLVO theory. According to it, the total interaction potential ( $V_T$ ) acting on two approaching nanoparticles can be evaluated as the sum of the repulsive and attractive contributions acting among them, as reported in Figure 1.1.

As it is evident from the DLVO diagram, the interaction potential presents a deep energetic well corresponding to aggregated species and a maximum, which represents the energy barrier that the particle has to overcome to aggregate. The stronger the repulsive forces, the higher the maximum, and the lower the fraction of collisions leading to aggregation. [12] The energy barrier can be overcome either by increasing the kinetic energy of the system (*e.g.*, by stirring or applying high shear) or by decreasing its magnitude through the addition of an electrolyte (*e.g.*, LiCl, MgCl<sub>2</sub> and AlCl<sub>3</sub>), which screens the repulsive forces and compresses the electrical double layer. [13] In this case, if the energy barrier is reduced to a certain level, Brownian motion allows the particles to overcome it, leading to effective aggregation during collision. It is also worth reporting that an important parameter governing the addition of an electrolyte is the critical coagulation concentration (*ccc*), which represents the minimum concentration of salt leading to a zero energy barrier. The latter differentiates the two limiting situations of aggregation: DLCA and RLCA. The former indicates the Diffusion Limited Cluster Aggregation, where no repulsive energy barrier exists and the rate of particle

aggregation is entirely controlled by Brownian motion. RLCA, on the other hand, identifies the situation where a repulsive energy barrier is present and the aggregation becomes controlled by the inter-particle potential. This situation is thus defined as Reaction Limited Cluster Aggregation.

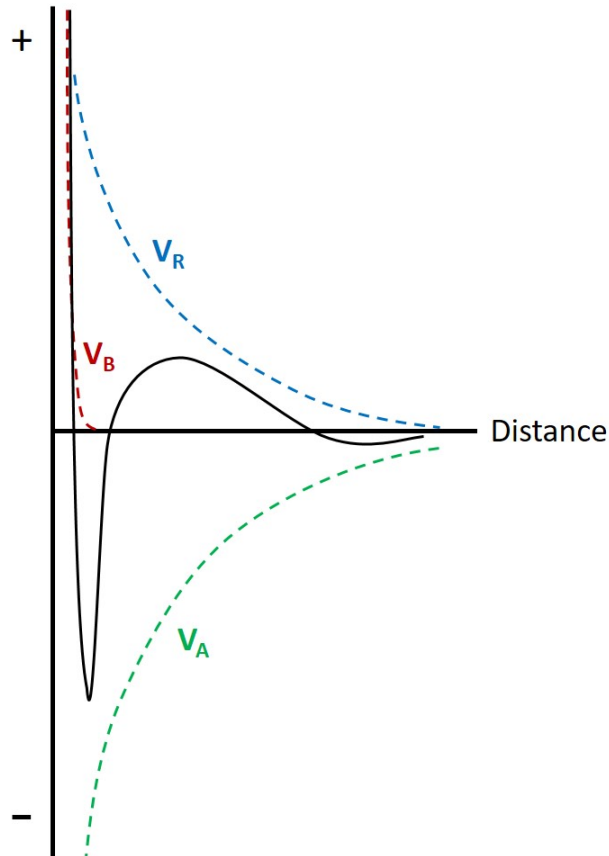


**Figure 1.1:** Total interaction potential acting among two approaching nanoparticles, according to DLVO theory.  $V_A$  = Potential energy of attraction (green dashed line),  $V_R$  = Potential energy of repulsion (blue dashed line), and  $V_B$  = Contribution of Born forces (red dashed line).

The main difference between these two regimes is the rate of aggregation. While in DLCA each collision leads to the formation of a cluster, in RLCA only a fraction of them is effective and in the remaining cases the repulsive forces prevail and the

barrier cannot be overcome. The parameter taking into account the difference of the two rates is the so-called Fuchs stability ratio,  $W$ , defined as: [14]

$$W = \frac{\beta_{DLCA}}{\beta_{RLCA}} = 2a \int_{2a}^{\infty} \exp\left(\frac{V_T}{kT}\right) \frac{dr}{r^2} \quad (1.3)$$

where  $a$  is the radius of the particle and  $r$  is the generic distance.

As it is evident from Equation 1.3, the Fuchs stability ratio is proportional to the interaction potential. The higher the value of the energy barrier, the higher  $W$ , and the slower the aggregation rate in RLCA conditions. Another consequence of the different regimes is the structure of the formed clusters, and in particular their morphology, which can be expressed using the concept of fractal dimension ( $d_f$ ). The latter gives an indication of the compactness of a cluster and its value ranges from 1 (linear alignment) to 3 (fully coalesced spheres). The typical values observed for DLCA and RLCA are in the range of 1.7-1.9 and 2.0-2.2, respectively. [15] The clusters obtained in RLCA regime are more compact as a consequence of the fact that only a fraction of the collisions between the particles leads to aggregation.

Shear-induced aggregation identifies the situation in which the aggregation process is merely driven by the velocity gradient induced, for instance, by forcing the latex to pass through a microchannel. More aptly, a colloidal suspension that is stable in stagnant conditions due to charge stabilization can aggregate when high shear flow is imposed, without electrolyte addition. [16–18] Moreover, in shear-induced aggregation cluster breakage plays a crucial role. *De facto*, the imposed high shear is not only capable of accelerating the rate of aggregation, but also to break the clusters. [19] Furthermore, cluster rearrangements may occur, driven by the minimization of the curved interfacial area of the primary particles in the aggregate, leading to more compact structures. [20,21] The main advantage of the aggregation under high shear is that it does not entail the addition of an electrolyte

to destabilize the system. The latter, in fact, is often difficult to be completely removed and may affect the purity as well as lead to changes in the electronic, mechanical and optical properties of the final polymer. [22] Moreover, shear-induced aggregation allows a continuous process and is particularly suitable to scale-up for industrial productions. [12] However, when additional non-DLVO interactions (*e.g.*, strongly repulsive, short-range hydration, and steric forces) become relevant, shear-induced aggregation may not be feasible. [23–25]

Regardless of the different aggregation methods implemented, it is well-accepted that colloidal aggregates present self-similarity properties, obeying the fractal geometry. [26] This means that the cluster mass scales with its size with a power-law correlation and independently from the length scale analyzed. The scaling exponent known as Hausdorff dimension is the  $d_f$  of the cluster and the equation describing this relation is given by: [15, 27–29]

$$i = k_f \left( \frac{R_g}{a} \right)^{d_f} \quad (1.4)$$

where:

- $i$  is the mass (*i.e.*, number of particles) of the cluster;
- $R_g$  is the radius of gyration of the cluster;
- $a$  is the radius of the primary particle;
- $k_f$  is the scaling prefactor which correlates with  $d_f$  according to:

$$k_f = 4.46d_f^{-2.08} \quad (1.5)$$

## 1.2 Polymer latexes: synthesis and applications

Polymers are materials made of repeated sub-units, monomers, which exhibit a large range of different properties and have various applications. Their mechanical, physical and chemical characteristics can be tailored to meet the specific needs by varying for example the type of the constituents, the chain lengths (which is proportional to the molecular weight) and the architecture of the polymer. The synthesis mechanism of these materials can be divided into step and chain polymerization. The former involves the formation of a high-molecular-weight polymer after many individual reactions between at least bifunctional monomers, whereas the latter rely on an initiator, which react with the active center located on the monomer to progressively add single units to the growing chain. [30] These two opposite mechanisms are schematically represented in Figure 1.2.

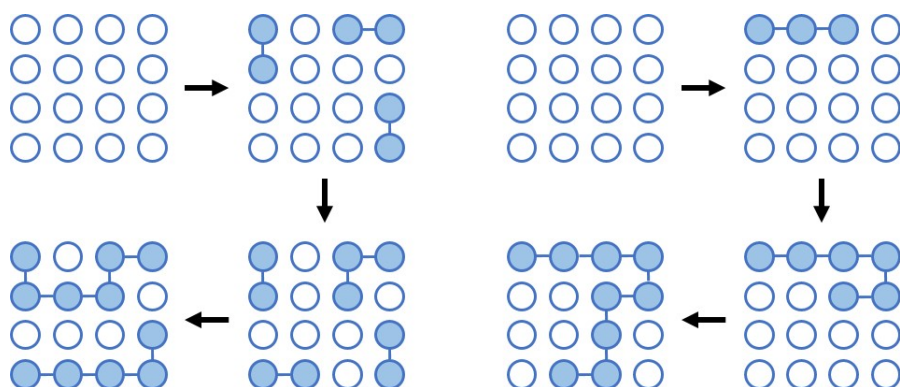


**Figure 1.2: Scheme of step (left) and chain (right) polymerization.**

Free-radical polymerization is often used to produce polymers *via* chain-growth mechanism. This reaction can be divided in four main steps, namely initiation, propagation, chain transfer, and termination. The first one involves the formation of free radicals when an initiator is decomposed chemically, thermally or by radiations. These radicals promptly react with the polymerizable unsaturated bond present on the monomer species to form the so-called active chains, which can

further react during the propagation phase. This step is characterized by the continuous addition of monomeric units into the growing side of the polymer chains, until eventually termination occurs. This phase arrests the growth of the molecule to form a dead chain, which will not further react. The chain transfer step involves the shift of a radical to another species, being it a monomer, a polymer or a transfer agent.

Emulsion polymerization is the most common technique to produce polymers starting from water, monomer, initiator and stabilizer. The peculiarity of this process is that the initiator is hydrophilic and therefore is solubilized in the water phase and not in the organic phase, as in suspension polymerization. As a consequence, the reaction starts in water, in which a small amount of monomer is dissolved. Nevertheless, as soon as the polymer chain forms, owing to its hydrophobic nature, a phase separation occurs and the formation of a polymer phase stabilized by the emulsifier is observed. The polymerization continues mainly within the newly formed polymer phase, leading to a final size of the particles ranging from 50 nm to 1  $\mu\text{m}$ . Due to the limited diameter of the formed nanoparticles and therefore their high specific surface area, heat removal from the system is extremely efficient. This aspect guarantees the achievement of enhanced productivity and high polymerization rate, simultaneously. Moreover, the limited size of the particles affects also the molecular weight of the final polymer, due to the so-called “segregation effect”. [31] Finally, the possibility of using water makes it the method of choice for most of the products formulations, especially with the recent environmental concerns related to the possible release of volatile organic compounds (VOCs) during application. [31] The colloidal dispersion of polymer nanoparticles obtained by emulsion polymerization in water is defined as latex. The latter is kept stable in time by the action of the emulsifier, which prevents



the polymer particles to coagulate either by carrying a net charge on them, thus making the nanoparticles repel each other, or by sterically avoiding their contact. Latexes have various applications, including paints and coatings, adhesives, paper and textile industries, construction materials. [32–35]

To meet the specific application needs, often multiple monomers are polymerized together to form a so-called copolymer. The latter, indeed, allows for tuning the material properties such as the crystallinity, the glass transition temperature, as well as the mechanical behavior, by varying the content of each monomer. Styrene, for example, is a brittle material when used as a homopolymer. However, if copolymerized with butadiene, the impact resistance of the resulting copolymer can be significantly increased. [36]

Copolymers can be produced using various methods resulting in different structures. A random copolymer has the different monomeric units distributed randomly, while an alternating one has alternating monomeric units in equimolar amounts. Block copolymers have uninterrupted linear sequences of the same units, whereas graft polymers consist of a backbone of one monomer to which one or more side chains of the other unit are attached, which results in nonlinear chains. The different possible structures are sketched in Figure 1.3.

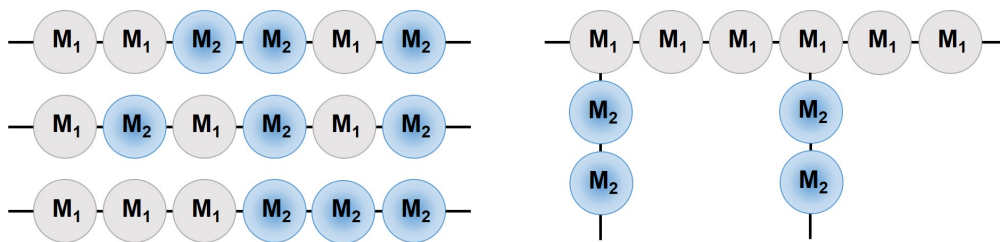


**Figure 1.3:** Schematic representation of random (top left), alternating (center left), block (bottom left), and nonlinear graft (right) copolymers.

Depending on the synthesis technique, the feed composition as well as the

relative reactivity of the monomers, the structures reported in Figure 1.3 can be obtained. A block copolymer comprises two or more homopolymer subunits linked by covalent bonds and it can be synthesized with specific operating conditions. A random structure is obtained when both monomers are simultaneously present in the reactor, whereas a graft copolymer requires special synthesis techniques.

### 1.3 Composite materials

Composites are materials made of multiple components which are classified as matrices and reinforcements, with different chemical and physical properties, which when combined form a new type of product with better overall performance. Wood and bones are examples of natural composites which exist in nature. The first one is made of lignin, the matrix, reinforced by cellulose fibers and the second one consists of a hard but brittle material (*i.e.*, hydroxyapatite) together with a soft and flexible material (*i.e.*, collagen). Since the early 1960s, there has been an increasing demand for materials with specific requirements which cannot be obtained with the use of a single constituent. As an example, for constructions and aviation there is the need of materials which are stiff and strong, while at the same time being light and flexible. Other application of composites include automotive, energy, infrastructures, sports and biomedical. [37–40]

Beside the properties of the constituents, the ratio between the matrix and the reinforcement as well as the geometry and orientation of the adjuvant are critical. This last aspect, in particular, is of utmost importance. For some applications, the reinforcing material has to be uniformly and homogeneously dispersed into the matrix at the smallest possible scale to maximize its effects (*e.g.*, for electronic applications), whereas in others it has to be continuously oriented in a specific direction (*e.g.*, reinforced concrete). [41]

## 1.4 Scope of the thesis

The aim of this thesis is to design and produce functional composite materials in which one of the constituents is a polymer. These include separators for lithium-ion batteries based on ionic liquids as well as construction materials with enhanced crack-bridging properties.

The thesis comprises an introduction to the world of colloids, including their definition, peculiar properties and stability, as well as to polymer latexes, applications and production strategies. After the introductory section, this work contains five main chapters dealing both with fundamental studies on the understanding of the aggregation phenomena occurring at a colloidal level, which provide the bases for the subsequent chapters involving the synthesis and development of innovative materials.

Chapter 2 deals with the understanding of the shear-driven aggregation kinetic of a polymer colloidal dispersion processed into a microchannel. In particular, a new, previously unobserved phenomenon related to bi-particle collision and the targeted experiments accomplished to verify the hypotheses are presented.

In chapter 3, a colloidal polymer latex is aggregated in shear-controlled regime to observe for the first time mass transfer between two colliding particles. To capture this, two differently labeled polymer dispersions were prepared and monitored through light scattering and fluorescence microscopy during aggregation.

Chapter 4 describes a new and versatile process to produce separators based on ionic liquids for lithium-ion batteries for high power applications, such as electric vehicles and smart grids. A polymer dispersion is aggregated to produce fractal

clusters which are then impregnated with the electrolyte and hot-pressed to form a homogeneous, transparent, and thin membranes. In chapter 5, the process and the battery performance are improved and optimized through addition of nanofillers to form composite clusters and the resulting separators show higher values of ionic conductivity and greater mechanical properties with respect to the state of the art commercial materials.

Chapter 6 presents a systematic study of the soft core-hard shell particle morphology on the production of redispersible polymer powders and on the crack-bridging properties of the cement-based membranes obtained from them. More aptly, different polymer latexes at high solid content with varied core-shell ratio, shell thickness and hardness were prepared from monomers *via* semi-batch emulsion polymerization and characterized in terms of size, composition, and softness (*i.e.*, glass transition temperature) to identify the optimal design of the polymer nanoparticles.

In the last chapter of this thesis, the most relevant results are carefully summarized and the outlook of these projects is thoroughly discussed, including some suggestions for future research.

## Chapter 2

# Aggregation of Stable Colloidal Dispersions under Short High-Shear Conditions

---

This chapter is based on the following publication: J. Lu, S. Caimi, P. Erfle, B. Wu, A. Cingolani, Y. Luo, A. Dietzel, P. Luo, H. Wu, M. Morbidelli, Aggregation of Stable Colloidal Dispersions under Short High-Shear Conditions, *in preparation*.

Shear-driven aggregation of colloidal particles is a process similar to a bimolecular chemical reaction, resulting also from collisions among the particles. The corresponding rate expression, derived based on the convective diffusion (two-body Smoluchowski) equation, has the following form: [42, 43]

$$k \sim k_0 \exp\left(\frac{-U_{max}}{k_B T}\right) \quad (2.1)$$

with

$$k_0 \sim \sqrt{\frac{3\pi\alpha\mu\dot{\gamma}a^3 - U''_{max}}{k_B T}} \exp\left(\frac{6\pi\alpha\mu\dot{\gamma}a^3}{k_B T}\right) \quad (2.2)$$

where  $k_B$  is Boltzmann's constant,  $U_{max}$  is the colloidal interaction energy barrier (thus,  $U''_{max} < 0$ ),  $\mu$  is the viscosity of the solvent,  $\dot{\gamma}$  is the shear rate,  $\alpha$  is a geometrical parameter, and  $a$  is the particle radius. It is therefore clear from Equation 2.1 that for shear-driven aggregation, the particles should possess enough energy to overcome the energy barrier, so as for the reaction between two particles to occur.

On the other hand, our recent experimental results on the shear-driven aggregation reveal a behavior that has never been observed in a bimolecular aggregation process. We studied the shear-driven aggregation kinetics of PS (polystyrene) and PVdF (polyvinylidene fluoride) nanoparticles (NPs), respectively, by forcing the NP dispersions to repeatedly pass through a Z-shape microchannel (Z-MC) of a rectangular cross section with a length of  $5.8 \cdot 10^{-3}$  m and cross-sectional area of  $5.26 \cdot 10^{-8}$  m<sup>2</sup> at a shear rate of  $\dot{\gamma} \sim 10^6$  s<sup>-1</sup>. [44, 45] It was expected that, as a "bimolecular reaction" process, the aggregation kinetics should follow Equation 2.1, *i.e.*, the conversion ( $\chi$ ) of the reactants (NPs) to the products (large clusters) should increase as the pass number of the dispersion (*i.e.*, the residence time) in the Z-MC increases, till reaching a value close to unity. However, it is surprising that the experimental results for both the PS and PVdF NPs did not follow Equa-

tion 2.1. Indeed, it was observed that, as the pass number in the Z-MC increases, the conversion of the NPs to the large clusters initially increases and then reaches a plateau value that is far from complete conversion.

We have tried to consider various possibilities of additional processes occurring under this intense shear. In particular, the observed phenomenon might be explained if erosion of the NPs from the surface of the large clusters in the turbulent field would take place when they grow large enough. [46–48] This is similar to a reverse reaction. As the conversion of the NPs to the large clusters increases, the erosion rate increases and eventually an equilibrium between erosion and aggregation is reached. Thus, the net conversion of the NPs to the large clusters does not further increase. However, such an equilibrium mechanism between erosion and aggregation has been excluded through the following *ad-hoc* designed experiment. We have prepared a NP dispersion at the same particle volume fraction ( $\phi$ ) as the remaining one after the conversion reached the plateau. Now, since the large clusters are absent, the possibility of the erosion process is excluded, and we would expect that a net conversion of the NPs to the large clusters should occur when the prepared NP dispersion passes repeatedly through the Z-MC. However, the experiments showed that no visible conversion of the NPs to the large clusters took place. Thus, the plateau conversion of the NPs to the large clusters does not result from the equilibrium between erosion and aggregation, or, in other words, the erosion process is insignificant in our systems.

The result of this experiment suggests the existence of a minimum time required for the aggregation to occur, with respect to the limited residence time of the dispersion in the Z-MC for each pass. To better describe such a minimum time problem, let us consider the colloidal interaction potential between two NPs, 1 and 2, illustrated in Figure 2.1a. Before the intense shear force is introduced, statistically, there is an average distance between the two neighbor NPs, 1 and 2, at

rest. It should be mentioned that in the case of PVdF NP dispersions studied previously, [45] the original latex was cleaned by adding ion-exchange resins (Dowex MR-3, Sigma-Aldrich) to completely remove all removable electrolytes such that the surface tension of the NP dispersion measured at  $\phi = 0.5\%$  was close to that of deionized water. In this case, due to the extremely low ionic strength, the electrostatic repulsion becomes substantially long-range such that the NPs can feel strong repulsion from their neighbors. In fact, at large  $\phi$  values, the NP dispersions become solid-like, with possible diffraction patterns. [49] This indicates that all the NPs are constrained in their specific location and cannot diffuse freely, leading to formation of colloidal crystals. Thus, for illustrative purpose, in this case we can consider that NP 2 is initially located somewhere on the repulsion peak, as illustrated in Figure 2.1a. When the NP dispersion is forced to pass through the Z-MC under the intense shear, part of the NPs may receive enough energy to overcome the interaction barrier ( $U_{max}$ ), thus converted to large clusters. After the first pass, the second one, the third one, *etc.*, can proceed. Thus, the conversion ( $\chi$ ) will increase as the pass number increases. On the other hand, as the conversion to large clusters increases, the volume fraction of the remaining free NPs,  $\phi$ , decreases, and consequently, the average distance between two neighbor free NPs, 1 and 2, changes. As an example, we have estimated the average distance between two neighbor free NPs under stagnant conditions ( $D_{ss}$ ) as a function of the conversion ( $\chi$ ) at various values of the mass fractal dimension of the clusters ( $d_f$ ), as reported in Figure 2.1b. Details about the  $D_{ss}$  estimation can be found in the Appendix, Section 8.1.4. It is seen that for  $d_f \geq 2.3$ , the  $D_{ss}$  value increases as  $\chi$  increases. Since the  $d_f$  value of the large clusters formed under intense shear has been well-documented to be  $d_f \geq 2.4$ , [44, 45, 50] one would expect that NP 2 in Figure 2.1a moves following the green arrow. Thus, the time needed for NP 2 to overcome  $U_{max}$ , *i.e.*, the aggregation time, increases as  $\chi$  increases. If the required



aggregation time becomes larger than the residence time of the dispersion in the MC, no aggregation takes place. One may argue that if the residence time for one pass is smaller than the aggregation time, we can increase the residence time by letting the dispersion pass the Z-MC two, three or more times. In reality, this is not the case, because for a given residence time of one pass, if the intense shear may drive NP 2 to a position close to NP 1 but still unable to overcome  $U_{max}$ , due to the disappearance of the intense shear after having passed through the Z-MC, NP 2 would come back to the original position at rest, as if nothing had happened. Thus, when the second pass starts, the intense shear has to move NP 2 again from its original position. Therefore, under such a situation, no matter how many passes, no aggregation takes place, which explains the observed plateau in the conversion value.

It should be mentioned that the scenario discussed above depends strongly on the compactness of the clusters (*i.e.*, the  $d_f$  value). As shown in Figure 2.1b, when  $d_f \leq 2.2$ , the  $D_{ss}$  value decreases as  $\chi$  increases. This arises because in this case the large clusters due to very open morphology, typical of those formed under stagnant conditions, occupy substantially larger space, leading to the available space for the free NPs decreasing sharply with  $\chi$ . This ends up with the formation of a gel with complete conversion of the primary particles.

To verify the above speculated mechanism, we have designed the shear-driven aggregation process by using two Z-MCs of different lengths, *i.e.*, having two different values of the residence time for the dispersion in the Z-MCs. In this way, if the residence time is the essential factor leading to the limited conversion, we would have a larger conversion in the longer Z-MC. To reduce the change in the fluid dynamics in the Z-MCs to the minimum, we have designed the two Z-MCs in such a way that the first one is a single Z-MC (SZ-MC), while the second one is a double Z-MC (DZ-MC), which is like two SZ-MCs linked together. Detailed dimensions

of the two MCs are given in Figure 2.2a. It should be pointed out that, based on the design in Figure 2.2a, the DZ-MC has basically the same pressure drops at the inlet and outlet as the SZ-MC does, instead of double. For this reason, for a given mean velocity ( $v_m$ ) of water, the specific pressure drop (P/L) in the DZ-MC is slightly smaller than that in the SZ-MC, as both measured experimentally and predicted by CFD simulations in Figure 2.2b. In any case, the  $v_m$  versus P/L curves in Figure 2.2b are basically all parallel, following a power-law with a slope of about 0.57. Thus, the fluid dynamic characteristics in SZ-MC and DZ-MC are the same, typical of turbulent flow. [17, 51]

Microfluidic systems made from glass materials have recently been demonstrated to be very useful for studying emulsification and nanoparticle generation processes. [52, 53] The glass material not only provides an inert environment and allows optical observation of processes that take place inside the microchannels, they can also be closed by thermal bonding which leads to a very stable connection and allows to operate these microfluidic systems under high pressures. Both systems used here, the SZ-MC and the DZ-MC, are micro fabricated from glass, and the manufacturing details are given in the Appendix, Section 8.1.2. For the shear-driven aggregation, the SZ-MC and the DZ-MC were carefully assembled inside a stainless steel holder as shown in Figure 2.2c, and the experimental setup is schematically shown in Figure 2.2d. The NP dispersion at a given initial  $\phi$  value was loaded in the container and pumped at a defined mean velocity ( $v_m$ ) through the SZ-MC or DZ-MC. After each pass, we analysed the conversion of the NPs to large clusters,  $\chi$ , and the gyration radius and mass fractal dimension of the clusters,  $R_g$  and  $d_f$ . The details on the applied techniques to measure these parameters are given in the Appendix, Section 8.1.3.

Polystyrene (PS) NPs with an average radius,  $a = 39$  nm, were synthesized in our lab and used in this work, following the procedure reported in the Appendix,

Section 8.1.1. Before the experiments, all the removable electrolytes were cleaned using an ion-exchange resin (Dowex Marathon MR-3, Sigma-Aldrich), as detailed in our previous work. [50] Then, the NP dispersion was diluted with pure water to a volume fraction of  $\phi = 0.01$ , which was used in all the following experiments. The shear-driven aggregation of the PS NPs in the SZ-MC and DZ-MC was carried out at three different mean velocities,  $v_m = 40.3, 49.0$  and  $59.5 \text{ m s}^{-1}$ , respectively, at which the corresponding mean shear rates estimated from the CFD simulations are  $2.43 \cdot 10^5, 3.15 \cdot 10^5$  and  $4.08 \cdot 10^5 \text{ s}^{-1}$ , and the residence times for one pass are 14.9, 12.2 and 10.1 ms in the SZ-MC and 29.8, 24.5 and 20.2 ms in the DZ-MC, respectively. The conversions of the NPs to large clusters,  $\chi$ , from the SZ-MC and DZ-MC are compared in Figure 2.3a, as a function of the cumulative residence time ( $t_r$ ), *i.e.*, the residence time of one pass multiplied by the number of passes. The corresponding gyration radius ( $R_g$ ) and mass fractal dimension ( $d_f$ ) are reported in Figure 2.3b and 2.3c, respectively. It is clearly seen from Figure 2.3a that at each given  $v_m$  value, there are three stages. The first stage is the initial induction stage, where the shear-driven aggregation is dominated by doublets and very small clusters, while the conversion to large clusters,  $\chi$  remains very small. Such an induction stage reduces as  $v_m$  (*i.e.*, the shear rate) increases, as also previously observed. [44] The second stage corresponds to the fast increase of  $\chi$  with  $t_r$ , where, due to the accumulation of substantial amount of doublets and small clusters and the increase in the cluster size, *i.e.*,  $a$  in Equation 2.2, the shear-driven aggregation auto-accelerates, leading to fast formation of large clusters. The third stage is characterized by the conversion plateau, as discussed above. For the first and second stages, the conversion curves from the SZ-MC and DZ-MC completely overlap, while for the third stage, they do not.

The overlapping in the first and second stages indicates that the aggregation time between two NPs is much shorter than the residence time of one pass in the SZ-

MC, such that the cumulative residence time is equivalent to the real residence time. It should be further emphasized that here we consider the aggregation time between two NPs to form a doublet because of the specific form of  $k_0$  (Equation 2.2), which increases exponentially with  $a^3$ . Thus, once doublets and small clusters are formed, due to such strong size effect, the small clusters can be quickly converted to large clusters. In the plateau stage, the  $\chi$  curves from the SZ-MC and DZ-MC do not overlap anymore, and the plateau value of  $\chi$  for the SZ-MC is smaller than that for the DZ-MC. For example, at  $v_m = 49.0 \text{ m s}^{-1}$ , the plateau value is  $\sim 66\%$  for the SZ-MC, while it is  $\sim 80\%$  for the DZ-MC. The value of the mass fractal dimension in the plateau region is constant, with the same value for both the SZ-MC and DZ-MC, equal to  $d_f = 2.40$ , which is typical for clusters formed through shear-driven aggregation of stable colloidal systems. [50] As discussed with reference to Figure 2.1b, at  $d_f = 2.40$ , the average distance between two neighbour free NPs ( $D_{ss}$ ) increases as the conversion (or the cumulative residence time) increases. Therefore, when the average distance between two neighbor free NPs increases above a certain value, the time needed for their shear-driven aggregation to occur becomes larger than the residence time of the dispersion in the microchannel. Such a situation occurs obviously at a larger  $\chi$  value the longer the microchannel is.

One may have observed that in Figure 2.3a, even though at each  $v_m$  value, the plateau  $\chi$  value is larger for the DZ-MC than for the SZ-MC, when  $v_m$  increases from 49.0 to 59.5  $\text{m s}^{-1}$ , *i.e.*, the shear rate increases from  $3.15 \cdot 10^5$  to  $4.08 \cdot 10^5 \text{ s}^{-1}$ , the plateau  $\chi$  value for each microchannel (SZ-MC or DZ-MC) does not increase. Note that this occurs only in the plateau stage, while in the first and second stages the effect of the shear rate on the conversion is significant as it can be seen in Figure 2.3a. The first possible explanation for this observation is related to the effect of  $v_m$  (or  $\dot{\gamma}$ ) on both the residence time and the shear-driven aggregation time in

the microchannel. Specifically, although a higher  $v_m$  value leads to a larger shear rate, thus a shorter time for NP 2 to overcome  $U_{max}$ , it also results in a shorter residence time in the microchannel. Thus, the plateau conversion for each microchannel increases with the shear rate only up to a certain limited value. There are other factors that may also contribute to this observation. For example, when the mean velocity ( $v_m$ ) increases above a certain level, the turbulent characteristics in such a small microchannel may change and become difficult to describe with the same turbulent theory. [54,55] In addition, the gyration radius of the large clusters is around  $11 \mu\text{m}$ , as shown in Figure 2.3c. Since the width of the microchannel is only  $200 \mu\text{m}$ , *i.e.*, the aspect ratio is only about 10, the presence of large amounts of large clusters could alter the turbulent behavior within the microchannel.

Some comments are also due about the time evolution of the gyration radius of the clusters,  $R_g$ , shown in Figure 2.3c. For both the SZ-MC and DZ-MC, the  $R_g$  value increases quickly with  $t_r$  after the first induction stage and reaches a local maximum, and then the  $R_g$  value decreases gradually to a constant value. Such an overshooting phenomenon has been previously reported, [44,56–58] and may result from the different rates of formation and breakage of the large clusters, changes in the surface properties, cluster restructuring, *etc.* It is interesting to have found that the steady-state  $R_g$  value in the plateau regime is slightly smaller for the DZ-MC ( $10.2 \mu\text{m}$ ) than for the SZ-MC ( $11.3 \mu\text{m}$ ). This result may indicate that for the given system, the time scale for the breakage of a large cluster is smaller than that for its formation. Thus, reducing the residence time of the dispersion in the microchannel, *i.e.*, using a shorter microchannel, affects more the formation than the breakage of the clusters.

In summary, we have designed and carried out intense shear-driven aggregation of stable PS NPs in two microchannels: one in the form of single Z (SZ-MC) and another in the form of double Z (DZ-MC). These experiments show that when the

high shear is applied for short interval of time, repeated over and over again, the conversion increases up to a certain plateau which is well below full conversion. At a fixed mean velocity inside the microchannel, such a plateau conversion value increases as the length of the microchannel (*i.e.*, the residence time of one pass) increases. Therefore, the results confirm that the specific aggregation process involves a minimum time for a successful shear-driven aggregation to occur. If the residence time of the NPs inside a microchannel is smaller than this minimum aggregation time, no aggregation occurs when the NP dispersion passes through the microchannel. As mentioned above, the situation does not change if we let the NP dispersion repeatedly pass through the microchannel many times (*i.e.*, by increasing the cumulative residence time), because if the residence time of one pass cannot allow the NPs to overcome the interaction energy barrier, the shear-driven aggregation does not occur, and when they come out from the microchannel, the intense shear force disappears, and the NPs return to their original interaction state. We believe that this observed behavior may not be peculiar of high shear aggregation and may actually be extended to all activated bimolecular processes.

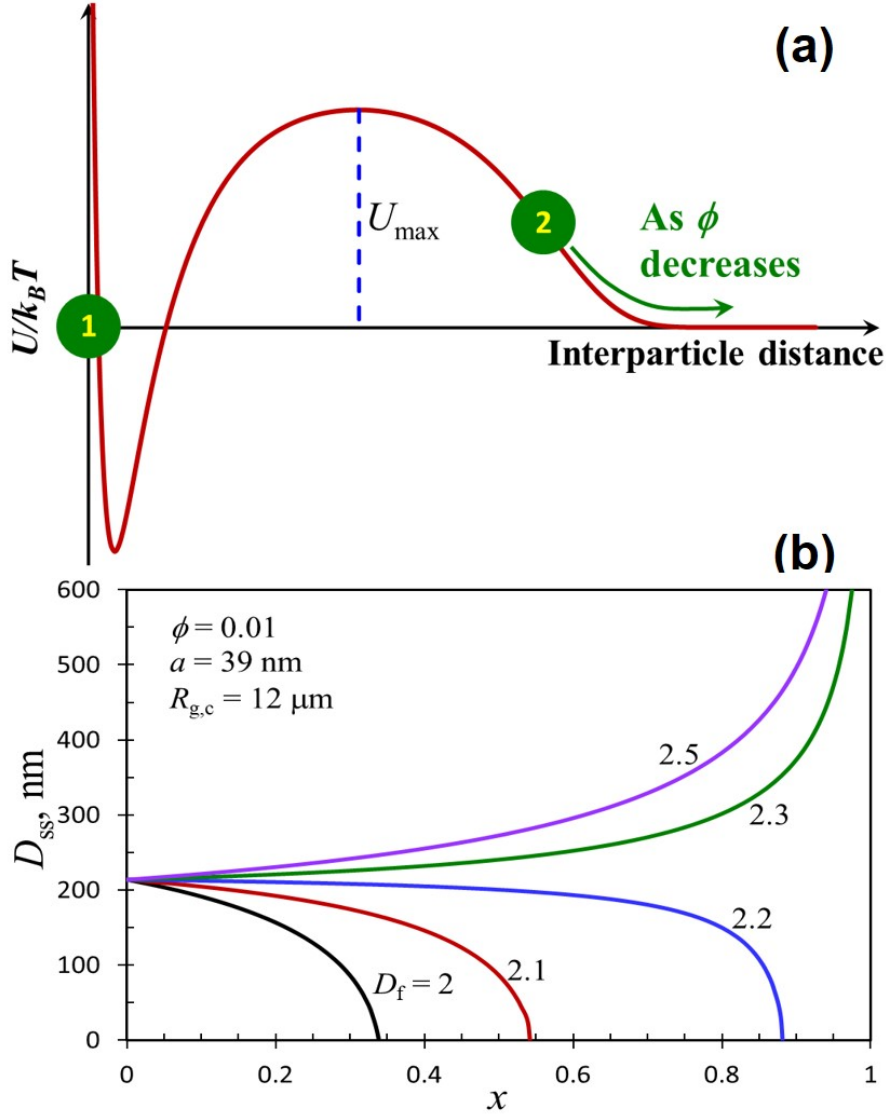


Figure 2.1: (a) Schematic representation of colloidal interactions and relative position between two NPs, 1 and 2, and (b) average distance ( $D_{ss}$ ) between free NPs as a function of the conversion to large clusters, at various  $d_f$  values, at the gyration radius of the large clusters,  $R_g = 12$   $\mu\text{m}$ , and the NPs radius,  $a = 39$  nm.

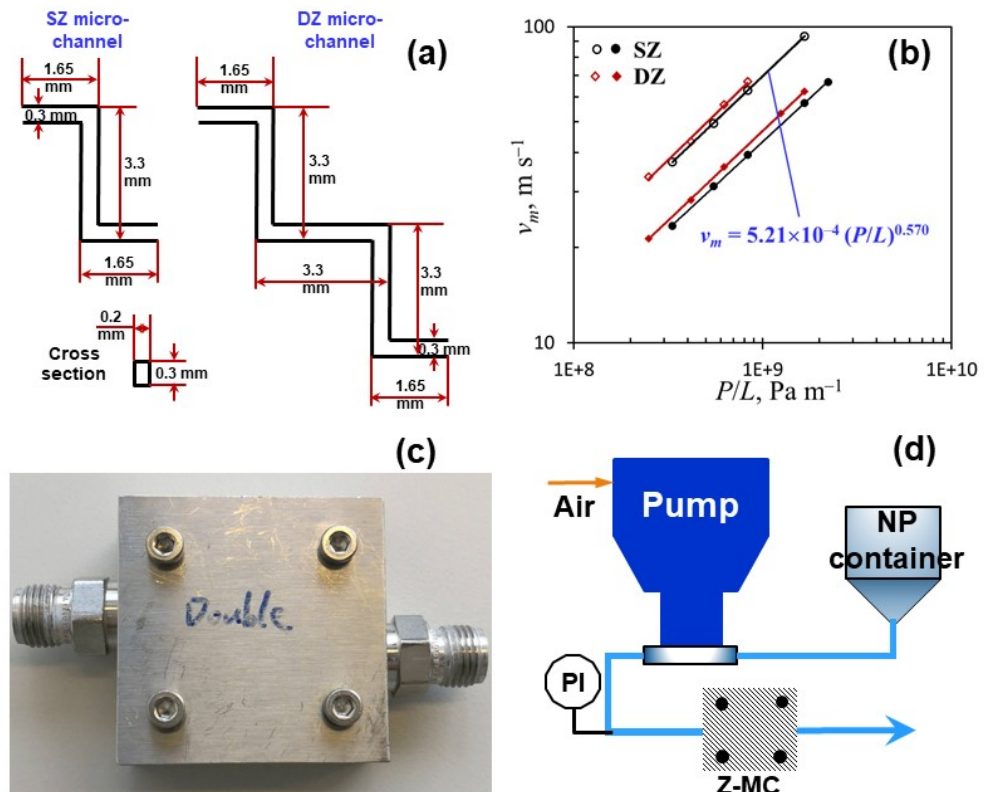


Figure 2.2: (a) Specific dimension of the SZ-MC and DZ-MC, (b) mean velocity ( $v_m$ ) of water in the SZ-MC and DZ-MC as a function of the pressure drop ( $P/L$ ) measured experimentally and predicted from CFD simulations, (c) holder of the MCs and (d) the setup of the shear-driven aggregation device.



## 2.0. DISCUSSION

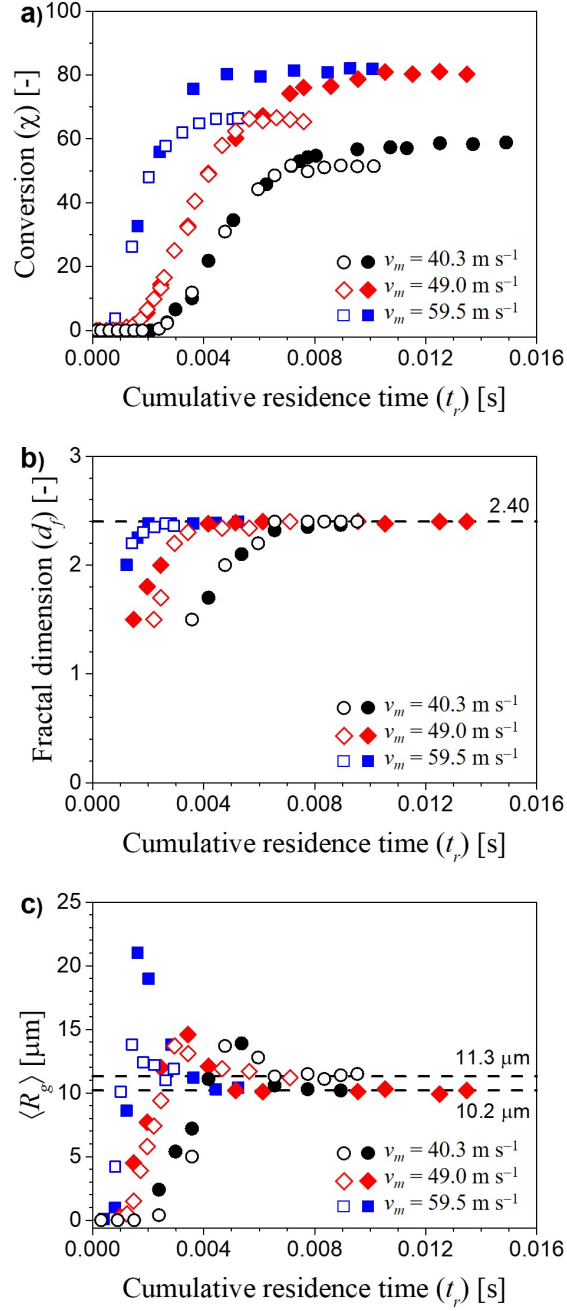


Figure 2.3: (a) Conversion ( $\chi$ ), (b) gyration radius ( $R_g$ ), and (c) mass fractal dimension ( $d_f$ ) of the clusters as a function of the cumulative residence time ( $t_r$ ), at different mean velocities ( $v_m$ ) of the dispersion in the SZ-MC (open symbols) and DZ-MC (filled symbols).



## Chapter 3

# Tracking of Fluorescently Labeled Polymer Particles Reveals Surface Effects during Shear-Controlled Aggregation

---

This chapter is based on the following publication: S. Caimi, A. Cingolani, B. Jaquet, M. Siggel, M. Lattuada, M. Morbidelli, Tracking of Fluorescently Labeled Polymer Particles Reveals Surface Effects during Shear-Controlled Aggregation, *Langmuir*, **2017**, 33(49), 14038-14044, DOI: 10.1021/acs.langmuir.7b03054.

### 3.1 Introduction

The process of aggregation and breakage of polymer particles under shear, which is a very relevant operation in the production of many polymeric materials, [59] is highly influenced not only by the physical parameters of the system (*i.e.*, solid and volume fraction, shear regime, particles size), [57, 60–63] but also by the surface chemistry and properties of the particles themselves. [1, 58, 64, 65] Our ability to quantitatively describe the behavior of aggregating particles exposed to shear forces is only limited to simple systems, behaving strictly as non-deformable sticky spheres. As soon as the particles present complex surface features, such as advanced functionality and composition, core/shell architecture and presence of plasticizers that soften the particles shells, they show characteristic and peculiar behaviors difficult to rationalize. [1] A particularly relevant example is the one of surface nano-roughness, which has already been shown to strongly affect polymer particles adhesion. [66, 67] Shear aggregation experiments carried out in our group on certain polystyrene particles have led us to hypothesize that, upon aggregation, their surface roughness was changing as a function of time, leading to completely different time evolutions of clusters morphology and to progressively decreasing average cluster sizes, instead of commonly encountered steady-state conditions. [58] Indeed, the increase in surface roughness leads to weaker bonds among particles within clusters, thus progressively increasing their breakage rate with time. Despite the importance of such effects, it is generally challenging to experimentally demonstrate not only the presence of surface roughness but even more a modification of this parameter upon prolonged exposure to shear forces. More importantly, the mechanisms that lead to these changes remain elusive. One of the proposed mechanism is plastic deformation, but what causes it still needs to be fully understood. Along with this line, molecular dynamic simulations have highlighted the possibility of some material transfer between particles as a result of repeated

aggregation/breakage events, with small chunks of polymer being torn off from the surface, and transferred to other particles. [68] Moreover, the phenomenon of chain exchange at a molecular level has been previously observed in different systems. [69,70] In this work, we have devised a novel and elegant strategy to experimentally prove the deformation of polymer particles exposed to shear forces, causing their aggregation and subsequent breakage. The surface alteration mechanism of suitably engineered colloidal particles was revealed by means of fluorescent microscopy. This technique has the potential to accurately visualize colloidal clusters when they are made of large enough primary particles. [71] Two sets of experiments were performed in this work. First, small polymer colloidal nanoparticles with slightly crosslinked polystyrene shell, swollen with styrene, which acts as a softener, were exposed to shear-controlled aggregation under fully-destabilized conditions. It was found that the system did not reach a stable steady state size, as commonly observed with hard particles, but showed a decrease in the average cluster size over time while keeping a constant fractal dimension (*i.e.*, maintaining the cluster structure unaltered) and never reaching a steady state condition. Among the various factors hypothesized to explain this behavior, an alteration of the surface, due to the softness of the outer layer induced by the monomer, seemed the most plausible and consistent with our previous findings. [58] In the second set of experiments, a different system was used, consisting of much larger particles, visible through an optical microscope, featuring a similar architecture to the smaller particles, but incorporating a fluorescent monomer. Using this second system, and working with a mixture of fluorescently labelled and non-labelled particles, we took advantage of fluorescence to monitor the surface alteration of the particles. In particular, we tracked whether some polymer could be displaced from a particle to another upon repeated aggregation and breakage events by simply recording the percentage over time of particles showing fluorescence. It was

demonstrated that substantial material exchange occurs between particles if their surface is sufficiently soft, which indeed is the case only in the presence of swelling monomer. Not surprisingly, the presence of a soft layer around the particles was also found to promote their adhesion upon contact. [72] Keeping in mind that material exchange might not be the only mechanism responsible for surface alterations of polymer particles, this work proves for the first time that material exchange takes place, thus providing novel insight into the importance of particle architecture and surface properties on shear aggregation.

## 3.2 Experimental

### 3.2.1 Materials

Divinylbenzene (DVB), styrene (STY), rhodamine B (RhB), azobis(isobutyronitrile) (AIBN), sodium dodecyl sulfate (SDS), potassium peroxydisulfate (KPS), poly vinylpyrrolidone 40k MW (PVP), dicyclohexylcarbodiimide (DCC), 4-(dimethylamino)-pyridine (DMAP), 2-hydroxyethyl methacrylate (HEMA), magnesium chloride and acetonitrile were purchased from Sigma-Aldrich and used without further purification. Ethanol was purchased from Fluka and used without further purification. Ultra-pure water was prepared by a Millipore Synergy water purification system. Nucleopore filters with 0.45  $\mu\text{m}$  pore size for dialysis were purchased from Whatman.

### 3.2.2 Synthesis of colloidal core-shell polymer nanoparticles

The synthesis of the polymer nanoparticles was carried out in a LabMax Automatic Reactor from Mettler-Toledo equipped with a 4 L jacketed glass reactor. The preparation involved two steps: core synthesis and shell covering. The former was made of 20% cross-linked particles of styrene and divinylbenzene, produced *via* semi-batch emulsion polymerization, whereas the latter was obtained by a seeded emulsion polymerization, using the 20% cross-linked particles as a seed, forming a 1% cross-linked shell around the core.

#### 3.2.2.1 Synthesis of the core

A mixture of water and surfactant (SDS) was initially charged into a glass reactor and the temperature was set at 70 °C using the oil heating jacket (initial charge, IC

as reported in Table 3.1). When the reactor temperature reached the set-point (in approximately 25 minutes), a solution of water and initiator (KPS) was injected through a septum directly into the reactor (initiator solution, IS). In order to guarantee starved conditions, an emulsion of styrene, DVB, water, and surfactant was fed over the reaction time using a syringe pump (continuous feed, CF as reported in Table 3.1). A solution of water and KPS was continuously fed using a second syringe pump, to guarantee the constant presence of the initiator (initiator feed, IF). When the reaction time was over, the system was kept at 70 °C for one hour, to ensure complete conversion of the monomer. The monomer conversion and the particle size evolution were followed by gravimetric analysis and dynamic light scattering (DLS), respectively. The exact quantities of the chemicals used in the particle synthesis are reported in Table 3.1.

### 3.2.2.2 Synthesis of the shell

To form a soft shell onto the core particles, the latter was added a second time into the LabMax together with water and surfactant (initial charge, IC as reported in Table 3.2). The previously synthesized latex worked as a seed for the second polymerization step. When the reactor temperature reached the set point of 70 °C, a water solution of initiator KPS was added to the jacketed reactor (initiator solution, IS). During the reaction time, a mixture of styrene and DVB was fed to achieve a radially homogeneous cross-linking density [73] (continuous feed, CF as reported in Table 3.2). Again, the monomer conversion and the average particle size were determined by gravimetric analysis and DLS, respectively. The complete recipe is reported in Table 3.2.



## 3.2. EXPERIMENTAL

---

**Table 3.1: Recipe for the synthesis of the core. All numbers are target values, the actual ones may vary by less than 1%. IC = Initial Charge, IS = Initiator Solution, CF = Continuous Feed and IF = Initiator Feed.**

	IC	IS	CF	IF
Water	1575 g	75 g	315 g	75 g
DVB			63 g	
Styrene			252 g	
SDS	6.2 g		2 g	
KPS		2 g		2 g
Reaction time		5 hours		
Cross-linkage degree		20 %		
Diameter		42 nm		
PDI		0.055		

**Table 3.2:** Recipe for the synthesis of the shell. All numbers are target values, the actual ones may vary by less than 1%. IC = Initial Charge, IS = Initiator Solution and CF = Continuous Feed.

	IC	IS	CF
Water	1295 g	50 g	
DVB			0.8 g
Styrene			79.7 g
SDS	1 g		
KPS		1.5 g	
Core latex	723 g		
Reaction time		5 hours	
Cross-linkage degree		1 %	
Diameter		54 nm	
PDI		0.030	

### 3.2.3 Synthesis and purification of rhodamine B - HEMA precursor

The synthesis method was adapted from Cova *et al.* [74] The rhodamine B-HEMA (RhB-HEMA) precursor was synthesized by Steglich esterification. In a flask, 4 g of RhB were dissolved in 80 mL acetonitrile. After full dissolution, 1.3 g of HEMA were added to the reaction mixture under stirring. In a second flask, 1.72 g of DCC and 52 mg of DMAP were mixed in 80 mL acetonitrile and added dropwise to the solution within 20 minutes. The reaction was run for 24 hours at 40 °C. The crude product was filtered to remove the precipitated by-product. The obtained solution was then purified by preparative chromatography using a C18 reversed phase column and acetonitrile/water mixture as the mobile phase. The purity of the product was confirmed by mass spectroscopy (LC-ESI-TOF) identifying a peak at 555 m/z. This precursor has been used to produce the fluorescent shell on the micron size particles.

### 3.2.4 Synthesis of core-shell polymer microparticles

#### 3.2.4.1 Synthesis of the core

The synthesis method was based on the work by Lee *et al.* [75] Accordingly, 1.5 g of PVP were dissolved in 102.6 g of ethanol in a 500 mL round bottom flask and heated to 70 °C. Furthermore, 0.15 g AIBN were dissolved in 15 g styrene and added to the reaction mixture upon reaching the target temperature. The reaction was left at 70 °C for 24 hours under continuous stirring. When a conversion of 80% was reached, the mixture was cooled to room temperature. At this point, 1.43 g DVB, corresponding to 20% of the converted amount of styrene, were mixed with 0.075 g AIBN and added to 58 g of the seed reaction product. The mixture was left for 6 hours under stirring at room temperature. After completion, the

mixture was added to a 250 mL three neck flask and heated to 70 °C for several hours, until conversion reached values above 95%. The final size was approximately 2  $\mu\text{m}$  in diameter. SEM pictures and optical microscopy confirmed very high monodispersity of the prepared particles.

#### 3.2.4.2 Synthesis of the shell

In order to grow the shell on the polymer microparticles, 50 g of the previously produced suspension of crosslinked core particles were added to a plastic wide neck bottle. Under stirring, 100 mL water were dripped into the solution over 20 minutes using an addition funnel. The resulting mixture was added to a Millipore dialysis chamber with a 0.45 micron Whatman Nucleopore membrane. Millipore water was rinsed through the chamber at 0.8 bar until the surface tension of the permeated solution reached the one of pure water, equal to 71.97  $\text{mN m}^{-1}$  at 25 °C, to ensure complete removal of PVP from the dispersion. The dialyzed particles were transferred to a 250 mL round bottom flask and heated to 70 °C. After charging 0.01 g KPS, 30  $\mu\text{L}$  of the monomer mixture (styrene with 1% DVB) were added successively every 30 minutes over 4 hours to increase the particle size by about 100 nm. In case of the synthesis of a fluorescent shell, the RhB-HEMA precursor was added to the previous mixture. The precursor was dissolved in 5 mL acetonitrile and put into a small flask and completely dried from the solvent, using a rotary evaporator. The conventional monomer mixture used in the previous case was used to re-dissolve the precursor. Effective inclusion of the RhB-HEMA within the polymer was assessed by UV measurements of the supernatant after precipitation of the particles. The absence of any signal confirmed complete incorporation. Moreover, to verify with more accuracy that the dye was bound to the polymer chains, some particles were centrifuged out of the aqueous solution, dried, re-dispersed and swollen with an organic solvent (isopropanol). After precipitation

of the polymer particles, the supernatant was newly analyzed by means of UV spectroscopy, and again no trace of dye was found. Increase in size of the particles was determined *via* small-angle light scattering (SALS) measurements and SEM pictures. Moreover, the absence of an unwanted nucleation, leading to a second small nanoparticles population was confirmed by DLS.

### 3.2.5 Processing of the particles

#### 3.2.5.1 Dilution and swelling

The synthesized nanoparticles latex has been diluted with degassed Millipore water down to a specific dry mass fraction ( $5 \cdot 10^{-5}$ ). This mixture has either been used as it is or swollen with additional hydrophobic monomer (*i.e.*, styrene), whose amount is calculated as a percentage of the solid content of the latex. The obtained solution has been left under mild agitation overnight at 200 rpm before further processing. The microparticles dispersion has been diluted in degassed Millipore water from the previous mixture to reach a mass fraction of  $5 \cdot 10^{-4}$ . In case of swelling, pure styrene equal to half of the saturation concentration in water has been added to the mixture. The system was left to equilibrate overnight. The repartition of the monomer between the water and the hydrophobic polymer phase allows for swelling of the outer, slightly crosslinked shell on the surface of the particles. Experiments were run using either fully non-fluorescent or an equal mixture of fluorescent and non-fluorescent particles.

#### 3.2.5.2 Stirred tank reactor

The diluted latex has been aggregated using a 2 L cylindrical stirred tank reactor equipped with a 60 mm Rushton impeller and four metallic cylindrical baffles. The solution has been fed into the reactor through an opening and the tank has

been firmly closed. Significant attention has been dedicated to the removal of any bubble of air inside the reactor, to avoid aggregation at the interface between the suspension and air. To prevent air entering the reactor when sampling, part of the excess polymer solution was pumped in a vertical tube (1.5 m high) connected to the reactor. The stirring velocity is set at 500 rpm, which corresponds to a maximum shear rate of  $17300\text{ s}^{-1}$  and an average one in the range of 900-1700  $\text{s}^{-1}$ , evaluated from the scaling for the maximum dissipation rate proposed by Soos *et al.* [76] In order to destabilize the system, 60 mL of a 2 M solution of  $\text{MgCl}_2$  were added to the reactor through an opening in the bottom plate. Owing to the strong shear forces produced by the stirrer, the primary particles start aggregating in a shear-controlled regime, which is not driven by Brownian motion but is controlled by the extent of the applied shear.

### 3.2.6 Characterization methods

#### Monomer conversion.

The monomer conversion is determined from the dry mass fraction of the sample. A small aliquot of the sample (about 1 mL) was spread over quartz sand and heated at  $120\text{ }^\circ\text{C}$  in air using a HG53 Moisture Analyzer from Mettler-Toledo.

#### Dynamic light scattering.

The average size of the nanoparticles was determined by dynamic light scattering (DLS) using a Zetasizer Nano ZS from Malvern.

#### Static light scattering.

To compute the size and the fractal dimension of the aggregated nanoparticles clusters, the average size of the microparticles as well as of their aggregated clusters, small-angle static light scattering Mastersizer 2000 from Malvern Instruments equipped with a laser having  $\lambda_{SALS} = 633$  nm was used. The radius of gyration  $\langle R_g(t) \rangle$  was obtained by fitting the structure factor in a Guinier plot, as reported in Harshe *et al.* [19] The fractal dimension  $d_f$  was extracted from the Guinier plot, by measuring the slope of the curve in the power-law region, using the relation  $\langle S(q) \rangle \propto q^{-d_f}$ .

#### Microscopy.

The microparticles and their clusters were analyzed using scanning electron microscopy (Gemini 1530 FEG from Zeiss), with field emission gun operated at 5 kV. The coating of the samples was performed using platinum. Optical microscopy was performed using a Leica SP8-AOBS confocal microscopy. An Argon laser at 550 nm was used for excitation of the samples and the emitted light was collected using one HyD detector. Bright field images were collected in parallel using a PMT detector.

#### Image analysis.

The image analysis was performed on the picture taken with confocal microscopy using ImageJ software. At least 2000 microparticles were evaluated for each measurement. For each picture, the average area in terms of number of pixels occupied by the non-clustered polymer microparticles was evaluated. The obtained value

was used, together with the total occupied area, to compute the total number of polymer microparticles present as individuals, non-clusters objects as well as aggregated in clusters, both in the case of non-fluorescent and fluorescent particles.



## 3.3 Results and Discussion

### 3.3.1 Shear-controlled aggregation

In our shear-controlled aggregation experiments, a colloidal suspension of primary particles is fed into a stirred tank reactor and an electrolyte solution is added to fully destabilize the system. However, owing to the presence of the stirrer, the aggregation process is not driven by Brownian motion but is controlled by the magnitude of the applied shear. Accordingly, the aggregation rate is highly affected by the stirring velocity. [63] The destabilization of the system due to the electrolyte addition cancels the repulsive energy barrier, thus leading to primary particles aggregating at a much faster rate into their primary energy minimum. The stirrer creates velocity gradients that drive particles and clusters against each other, thus increasing the frequency of their encounters. On the other hand, clusters may also break under the action of hydrodynamic stresses caused by the presence of shear forces. [63] Consequently, it is expected that the system reaches and preserves a steady state condition, determined by an equilibrium between the aggregation and breakage rates. [57] The critical parameter defining the region of shear-controlled aggregation is the Peclet number ( $Pe$ ) which expresses the ratio between the shear and the Brownian forces and is defined according to the equation:

$$Pe = \frac{3\pi\mu\dot{\gamma}R_p^3}{k_B T} \quad (3.1)$$

where  $\mu$  is the solvent viscosity,  $\dot{\gamma}$  is the shear rate,  $R_p$  is the radius of the primary particles,  $k_B$  is the Boltzmann's constant, and  $T$  is the absolute temperature. [65]

### 3.3.2 Aggregation of nanoparticles

The study of the aggregation of particles in a shear-controlled regime has been carried out using the polymer nanoparticles with a core-shell structure, synthesized through the recipe described in the experimental section. The soft shell of the polymer particles allows for swelling by additional monomer (styrene), which is used as a plasticizer that lowers the glass transition temperature of the polymer domain, [77] thus making it very soft at the operating temperature. The addition of highly concentrated (2 M) magnesium chloride solution ensures full screening of the surface charges located at the particles surface. The system is left under agitation for some hours and the morphology evolution of the clusters, in terms of the radius of gyration ( $\langle R_g \rangle$ ) and fractal dimension ( $d_f$ ) is monitored. As the latter is obtained *via* power-law regression of the scattering structure factor, only variations in the range of  $\pm 0.1$  are appreciable. Figure 3.1 reports the average cluster size and fractal dimension as a function of the aggregation time for the samples swollen with 0, 10 and 20% of additional monomer.

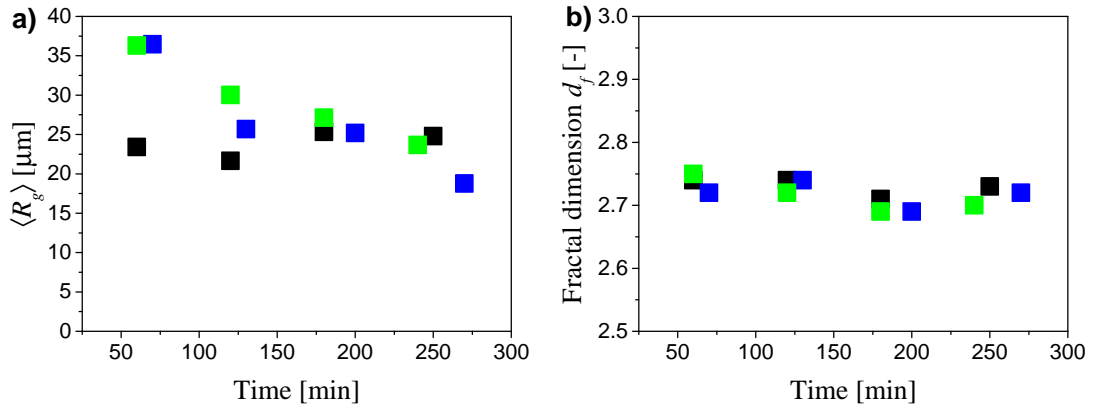


**Figure 3.1:** Time evolution of the average cluster size (a) and fractal dimension (b) for different swelling ratios (black squares: non-swollen; blue: 10% swollen; green: 20% swollen) during the shear-controlled aggregation of nanoparticles.

As it can be seen from Figure 3.1a, the average cluster size for the non-swollen

clusters presents no appreciable variations with time after about 50 minutes and reaches a constant value of approximately  $25 \mu\text{m}$  (black squares). This is in agreement with the results obtained by Harshe *et al.* [19] and Soos *et al.* [63] and shows that the interplay between aggregation and breakage reaches an equilibrium and the average cluster size remains steady in time. Due to the high  $Pe$  number, as soon as a cluster is broken into smaller fragments, it promptly aggregates with other polymer particles or clusters to reach the same constant average size. On the other hand, in the case of primary particles swollen with 10 and 20% of styrene, the average size of the clusters continuously decreases with time. In particular, the average size of the sample swollen with 10% of styrene is measured to vary from  $36 \mu\text{m}$  after 70 minutes to  $19 \mu\text{m}$  after 270 (blue squares). Likewise, the size of the sample swollen with 20% of additional monomer decreases from  $36 \mu\text{m}$  after 60 minutes to  $23 \mu\text{m}$  after 240 (green squares). In addition, Figure 3.1b shows that the fractal dimension remains constant at a value of approximately 2.7, which is virtually identical to that obtained for clusters made of non-swollen particles in the case of shear-induced aggregation and breakage processes. [19] The observed decrease of the aggregate size with time is in contrast with the available literature and accepted explanations for this trend are still missing. Consistently with what hypothesized in a previous work, [58] the observed trend could be the result of some alterations on the surface of the swollen primary particles, which eventually affect the bond strength among particles and consequently the rate of breakage. More specifically, after the particles undergo many cycles of aggregation and breakage, their surface could become more irregular and less homogeneous. The experimental evidence indicates that this process should be related to the morphology of the primary particles, which are made of a hard core surrounded by a shell that is softened through monomer swelling. One possible mechanism consistent with these observations is that the surface alteration of the primary particles occurs through

material exchange among different particles upon collision and breakage. These alterations may affect the surface adhesion of the particles and consequently the breakage rate because less energy is required in order to separate them. It is worth noting that the observed behavior cannot be simply due to the fact that the system is not yet at equilibrium conditions, because a destabilized system under shear-controlled aggregation regime typically reaches equilibrium between aggregation and breakage within about 60 minutes, at least for the particle concentration used in these experiments. [63]

### 3.3.3 Aggregation of microparticles

In order to confirm whether the hypothesized material exchange process occurs, aggregation and breakage have been investigated using microparticles produced according to the recipe reported in the experimental section. These particles exhibit the same architecture as the nanoparticles: they have a hard core of 2  $\mu\text{m}$  diameter, composed of polystyrene crosslinked with 20% DVB, and a soft outer shell of 100 nm, again made of polystyrene but only 1% crosslinked. The morphology of the microparticles before and after the growth of the shell is shown in Figure 3.2. Note that the microparticles present dimples, which probably result from the swelling and crosslinking procedure used to produce their shell, as reported and discussed earlier in the literature. [78, 79]

Furthermore, some particles have been made fluorescent by the addition of RhB-HEMA precursor in the monomer mixtures used to synthesize the shell, so that they can be visualized with a fluorescent confocal microscope. Their shear-controlled aggregation has been investigated by introducing an equal mixture of fluorescent and non-fluorescent particles into the stirred tank, following the same procedure as for the nanoparticles. Again, the experiments have been run without and with the addition of further styrene in order to swell, and thus soften, the

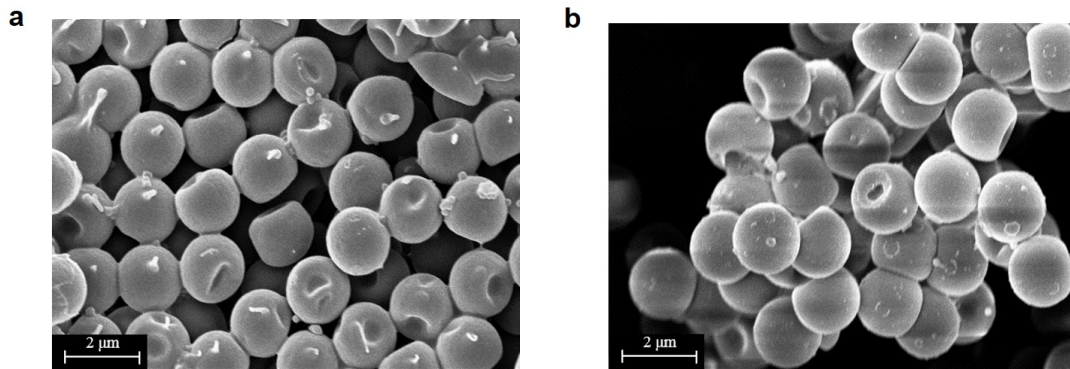


**Figure 3.2:** Particles without shell (a) and after shell growth (b).

particles outer shell. The number of fluorescent microparticles before and after aggregation, present both as single entities as well as grouped in clusters, has been determined by image analysis. Figure 3.3 shows the confocal pictures of the microparticles, before and after applying the fluorescent filter. This allows visualizing all the particles (Figure 3.3a) or only the fluorescent ones (Figure 3.3b). The two pictures are superimposed in Figure 3.3c, which allows appreciating how many microparticles result fluorescent.

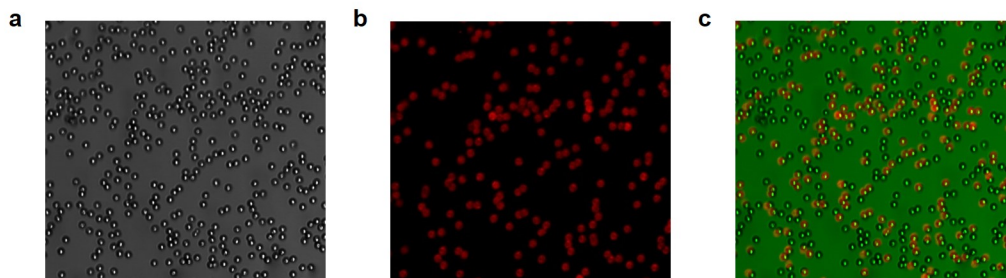


**Figure 3.3:** Micrographs of the microparticles in transmission mode (a), in fluorescent confocal mode (b) and their superposition (c).

### 3.3.3.1 Aggregation of non-swollen microparticles

Non-swollen microparticles were aggregated under shear and monitored for several hours. The  $\langle R_g \rangle$  values of the formed clusters measured by small-angle light scattering measurements are shown in Figure 3.4 (red squares). It can be observed that already after one hour a steady state of the average size is reached, which remains constant over the five hours experimental time. Remarkably, this equilibrium value for  $\langle R_g \rangle$  is considerably smaller than in the case of nanoparticles. This observation can be understood considering the number of particles present in each cluster, which can be estimated through the equation:

$$i = k \left( \frac{\langle R_g \rangle}{R_p} \right)^{d_f} \quad (3.2)$$

where  $k$  is the fractal prefactor, a number whose value typically ranges between 1 and 1.2, [80, 81]  $\langle R_g \rangle$  is the average radius of gyration,  $R_p$  is the radius of the primary particles, and  $d_f$  is the fractal dimension of the colloidal aggregates. It results that the number of nanoparticles aggregated in a cluster is in the order of 107, whereas the one of the microparticles is limited to 4-5. Since aggregation is a second order kinetic process, a smaller number of particles implies a lower aggregation rate, while breakage, being a first order kinetic process, is unaffected by a lower number of particles. It is, therefore, reasonable to expect a different equilibrium condition, dominated by the relative higher breakage contribution. Moreover, the breakage process is also strongly influenced by the size of the particles. For the same cluster size, in fact, a cluster made of micron-sized particles contains a lower number of particles and consequently a lower number of bonds among them. Given this relatively weaker bond strength compared to the hydrodynamic stress acting on the particles, it is reasonable to assume that, when subjected to shear, their clusters can re-break into much smaller units, including individual particles. [82]

In order to determine any alteration on their surface, the percentage of fluorescent particles was monitored as a function of time as shown in Figure 3.5 (red squares). The fact that this value does not change over five hours allows concluding that, in this case, no material exchange occurs among the surfaces of the primary particles.

#### 3.3.3.2 Aggregation of swollen microparticles

The same experiment has been repeated using particles whose shell has been swollen with styrene. The values of  $\langle R_g \rangle$  were determined *via* light scattering and shown in Figure 3.4 as a function of time (green squares). It is seen that the gyration radius reaches the value of 3  $\mu\text{m}$  within the first hour and then remains constant. Noticeably, it seems not to decrease over time, as in the case of the nanoparticles. This aspect is again due to the low number of particles present in each cluster, which makes it difficult to observe a significant decrease in the average cluster size in time when dealing with microparticles. In any case, it is a fact that the interplay between aggregation and breakage controls the process. Anew, the proportion of fluorescent particles was measured. As visible in Figure 3.5, the percentage of fluorescent particles clearly increases over time, moving from the initial 50% to approximately 62% after two hours and eventually to 70% after five hours (green squares). This experiment shows that the fluorescent polymer chains, initially present only on the surface of fluorescent particles, are displaced and can be found also on the surface of non-fluorescent particles. In particular, this material exchange occurs only when the shell of the particles is sufficiently soft, *i.e.*, when the particles are swollen by styrene. It is therefore reasonable that a similar mechanism occurs even in the case of nanoparticles, and might be responsible for the unexpected progressive decrease in the average cluster size.

### 3.3.3.3 Aggregation of microparticles without shell

For sake of completeness, the highly crosslinked polystyrene microparticles without shell were aggregated under shear. Interestingly, under the same conditions, they were unable to aggregate over the four hours time course of the experiment (Figure 3.4). This behavior further confirms the extreme importance of the surface of the particles in colloidal aggregation. More aptly, a softer surface, in this case due to a 1% crosslinked polystyrene shell of 100 nm, was observed to promote aggregation, whereas a harder one, composed of highly crosslinked polystyrene (20%), makes it impossible for the microparticles to form stable clusters in the tested conditions. They surely collide but due to their rigidity, weak bonds are formed, which are easily broken by shear forces.

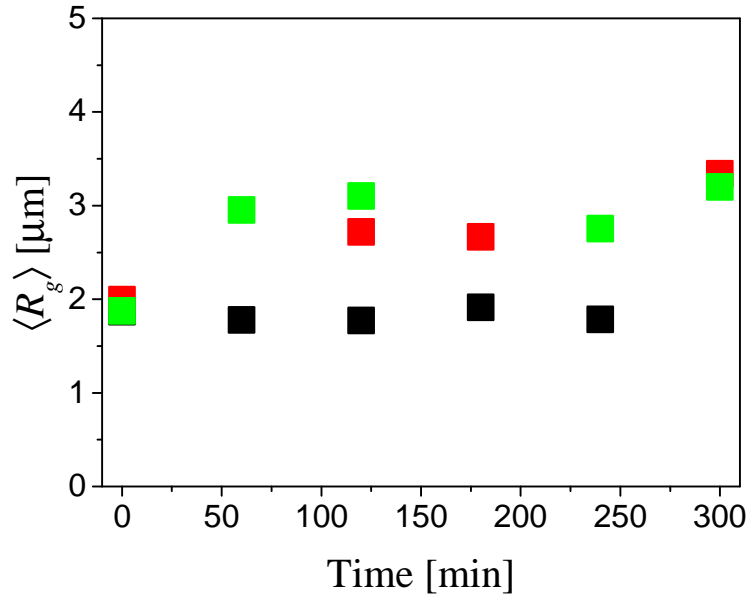


**Figure 3.4:** Average  $\langle R_g \rangle$  as a function of time for different microparticles. In particular: black squares refer to non-swollen core microparticles, red squares to non-swollen core-shell microparticles and green squares to swollen core-shell microparticles.



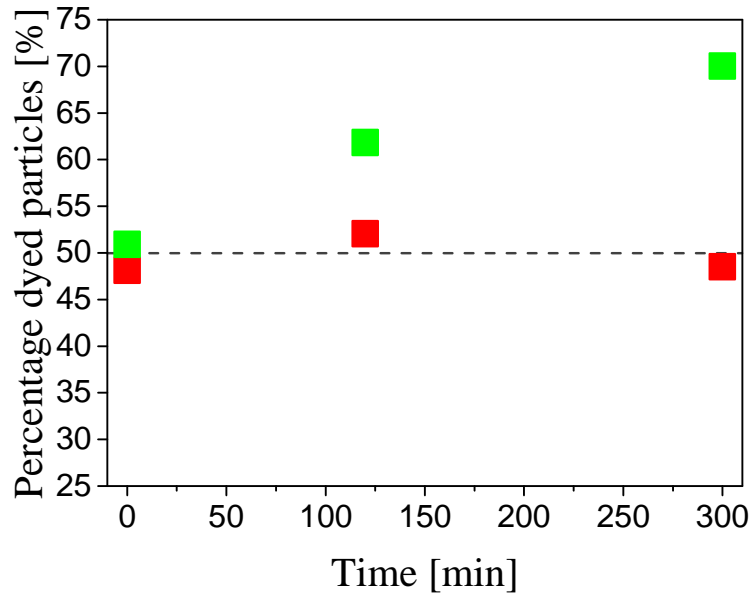


Figure 3.5: Percentage of fluorescent core-shell microparticles as a function of time (red squares: non-swollen, green squares: swollen).

### 3.4 Conclusion

In this work, shear-induced aggregation experiments of various polymer colloidal particles have been carried out, with the specific objective of clarifying the role of the softness of the particle shell on the outcome of the aggregation. In particular, in a previous work, we hypothesized that the surface of sufficiently soft particles could be deformed as a result of the repeated aggregation and breakage events, leading to an increase in surface roughness. This effect could be sufficiently pronounced to lead to exchange of material from one particle surface to another. In order to prove the presence of such material exchange, specially designed polymer particles with core-shell structure, and having fluorescence group incorporated into their shell have been prepared. To tune the softness of the polymer shell, some styrene monomer was added, which acts as a plasticizer. For the first time, material exchange occurring on the surface of core-shell polymer microparticles, when

softened by monomer addition, upon aggregation under shear was proven and highlighted. This was achieved by aggregating a 1:1 mixture of fluorescent and non-fluorescent particles, and by monitoring the increase in the number of particles exhibiting fluorescence as a function of time. An increase in the percentage of particles showing a fluorescent signature was recorded over time, reaching after 5 hours a fraction of 70%.

The consequences of our work are far-reaching. It is reasonable to assume this phenomenon to be responsible for the unusual behavior observed on similar nanoparticles in the same conditions (swollen shell). Indeed, the slow but progressive decrease in the size of the formed clusters over time upon shear-controlled aggregation, without substantial change in fractal dimension, and without reaching steady-state conditions, might be due to surface alterations and increased roughness on the polymer domain induced by material transfer. These modifications can affect the surface adhesion among the particles and lead to a restructuring of the clusters towards continuously new steady-state conditions between aggregation and breakage.

It is worth noticing that material exchange, which has been proven for the first time in this work, might not be the only phenomenon controlling the unusual behavior observed in shear-controlled aggregation of nanoparticles, but we believe that it represents a very important effect, the full consequences of it need to be further ascertained and deepened.

## Chapter 4

# PVdF-HFP and Ionic-Liquid-Based, Freestanding Thin Separator for Lithium-Ion Batteries

---

This chapter is based on the following publication: S. Caimi, H. Wu, M. Morbidelli, PVdF-HFP and Ionic-Liquid-Based, Freestanding Thin Separator for Lithium-Ion Batteries, *ACS Applied Energy Materials*, **2018**, 1(10), 5224-5232, DOI: 10.1021/acsaem.8b00860.

## 4.1 Introduction

Lithium-ion batteries (LIBs) since their appearance on the market in 1991 have received noticeable attention as the most popular energy storage system for portable electronic devices including laptops, cell phones, and music players. [83] Because of their high energy density and long cycle life, lithium-ion batteries are considered promising candidates for large-scale power applications, such as electric vehicles and emerging smart grids. [84–89] Proper selection of the electrolyte and separator is of utmost importance for achieving good battery performance in terms of cycle life, power density, reliability, and safety. [90–93] In particular, the separator has to possess specific properties such as chemical and electrochemical inertness towards all cell components, mechanical and dimensional stability, and physical strength. [94] To meet these requirements, different solutions have been intensively studied in the literature, including addition of nanofillers into the separator to promote the electrochemical and mechanical properties (the so-called composite membrane separators) or blend of different polymers with complementary properties. [93] The safety aspect becomes especially important when the cells are exposed to mechanical, thermal, or electrical abuse conditions, typical in the applications of LIBs at high powers. These safety considerations are particularly addressed in the utilization of highly volatile, thermally unstable, and toxic organic-solvent-based electrolytes, together with the concrete risk of leakage associated with them. [84, 95–105]

Accordingly, in recent years, alternative, effective, and innovative electrolytes have been extensively studied. Among those, the possibility of using ionic liquids (ILs), characterized by low flammability, negligible vapor pressure, low toxicity, high ion density, and high ionic conductivities, was thoroughly investigated. [84, 106–119] The choice of the anion and cation comprising an IL affects several important characteristics, including density, viscosity, conductivity, and thermal and electro-

chemical stability. [120–122] In particular, the ionic conductivity of an IL is often proportional to its viscosity: a higher value of the viscosity leads to a reduced mobility of ions and results in a lower conductivity. [123] Among the various studied ILs, the pyrrolidinium-based ILs are considered to be one of the most promising candidates, as they are characterized by high ionic conductivity (greater than 1 mS cm<sup>-1</sup> at room temperature), excellent thermal stability (> 300 °C), and broad electrochemical window (ESW, 0–5 V *versus* Li<sup>0</sup>/Li<sup>+</sup>). [122, 124–131] Among the ILs of this class, Pyr13TFSI is often selected as it possesses one of the lowest viscosities due to the reduced steric hindrance of the Pyr13<sup>+</sup> cation. [112, 132–134] Moreover, the TFSI<sup>-</sup> anion, having low Lewis acidity due to the delocalized negative charge over five atoms, shows a weak coordinating power with Li<sup>+</sup> and guarantees chemical inertness and great electrochemical stability toward cell oxidation. [95, 99, 135–140]

For the formation of a freestanding, dimensionally stable and flexible, IL-based membrane, the IL has to be incorporated inside a polymer matrix to form a so-called gel-polymer electrolyte (GPE) membrane. Among the available polymers, poly(vinylidene fluoride-*co*-hexafluoro propylene) (PVdF-HFP) is receiving considerable attention due to its high dielectric constant ( $\epsilon \sim 8.4$ ), good compatibility with the electrodes, low glass transition temperature, and crystallinity, which enable improved ionic conductivity. [141–145] The incorporation of the IL within the polymer matrix provides adequate mechanical properties, while maintaining great electrochemical characteristics typical of ILs. [124] Along this line, many researchers focused on producing these GPE membranes by solution casting, a technique that typically involves the following steps: (1) finding specific solvents to dissolve the applied polymer, (2) dispersing the IL, lithium salt, and the other components in the polymer solution, and (3) casting to form the GPE membrane after solvent evaporation. [124, 146–148] Despite being very promising and proven

to work, this technique requires use of specific organic solvents that not only dissolve the polymer but also have good affinity to the IL and the lithium salts. In addition, the impact of these solvents to the environment and the cost of their recovery are also important issues to be considered in industrial practice. To overcome the above-mentioned drawbacks and increase the process sustainability, in this work we devise a method that is purely water-based to prepare freestanding, flexible, and transparent IL-polymer membranes for LIBs. The principle of the design involves (1) formation of micron-scale fractal (porous) clusters from the PVdF-HFP nanoparticles (NPs) in water through intense shear-driven aggregation, a technique previously developed in our group, [44, 149] (2) drying of the clusters and subsequently mixing with the IL and the lithium salt, and (3) hot-pressing of the polymer clusters/IL mixture to form a homogeneous, freestanding membrane. It will be seen that the fractal clusters formed in step 1 possess a large porosity and a well-defined, interconnected pore structure, suitable to host the IL and form a bicontinuous structure. The developed membranes have been successfully used in half-coin cell batteries.

## 4.2 Experimental

### 4.2.1 Materials

The following chemicals have been employed without further treatments: N-propyl-N-methylpyrrolidinium bis(trifluoromethane sulfonyl)-imide (Pyr1308b, purity 99.5%) was purchased from Solvionic. The structure of Pyr13TFSI is reported in Figure 4.1. The water dispersion of PVdF-HFP NPs and bis(trifluoromethane)-sulfonamide lithium salt (LiTFSI) were provided by Solvay (Bollate, Italy). Ion-exchange resin (Dowex MR-3 hydrogen and hydroxide form) purchased from Sigma-Aldrich has been employed as received to remove the anionic surfactant adsorbed on the particle surface. [16] Dichloromethane (anhydrous, purity  $\geq 99.8\%$ ) was purchased from Sigma-Aldrich. The lithium iron phosphate (LFP) cathode material is commercial grade Life Power P2 from Clariant. Before assembling, the positive electrode and the separator were dried overnight under vacuum at 130 and 60 °C, respectively.

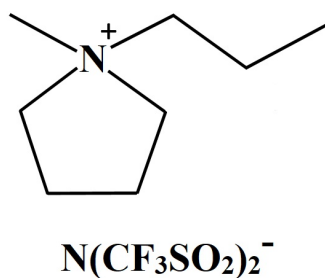


Figure 4.1: Structure of the ionic liquid, Pyr13TFSI.

### 4.2.2 Methods

Intense shear-driven aggregation of the PVdF-HFP NPs was carried out using a high-shear device, HC-5000 (Microfluidics), equipped with a L30Z microchannel with a width of  $300\ \mu\text{m}$ , a rectangular cross section of  $5.26 \cdot 10^{-8}\ \text{m}^2$  and a length of  $5.8\ \text{mm}$ . An operating pressure of  $120\ \text{bar}$  was used, corresponding to a shear rate of  $4.8 \cdot 10^6\ \text{s}^{-1}$ . [149] At this shear rate, when the volume fraction of the PVdF-HFP NPs was  $\phi = 18\%$ , a solidlike gel was formed just after one pass through the microchannel. Subsequently, the obtained gel was dried in oven at  $60\ ^\circ\text{C}$  and then ball-milled at  $600\ \text{rpm}$  for  $30\ \text{min}$ . The obtained clusters in the form of powder were sieved, and those with sizes smaller than  $63\ \mu\text{m}$  were collected, and referred to in the following as the polymer clusters (PCs).

For the preparation of the Li-ion-conducting electrolyte solution, dried LiTFSI salt was added to the Pyr13TFSI IL to obtain a  $0.5\ \text{M}$  solution, which is here referred to as the IL solution.

The dried PCs were then mixed with the IL solution, LiTFSI-Pyr13TFSI, at different mass fractions, to obtain a PC/IL slurry. Such mixing was simply done using a magnetic bar for few seconds, and, then, the slurry was kept at rest overnight to allow the liquid to impregnate the pores of the PCs. The slurry was then transferred to an aluminum sheet, covered with a second one, placed in a preheated hydraulic hand-press (Rondol, Strasbourg), and hot-pressed to form a membrane. The pressing temperature was selected close to the melting temperature of PVdF-HFP ( $T_m \sim 130\ ^\circ\text{C}$ ). After the hot-pressing, the hand-press was cooled down, while the pressing was held, until reaching room temperature. The formed membrane (electrolyte) is here referred to as the PCIL membrane.

The small-angle light scattering (SALS) instrument, Mastersizer 2000 (Malvern) equipped with a laser with the wavelength  $\lambda = 633\ \text{nm}$ , was used to characterize the morphology of the clusters formed by the intense shear-driven aggregation. In



## 4.2. EXPERIMENTAL

---

particular, we have measured the average scattering structure factor of the clusters,  $\langle S(q) \rangle$ , using the SALS instrument, which is defined as: [150]

$$\langle S(q) \rangle = \frac{I(q)}{I(0)P(q)} \quad (4.1)$$

Here,  $I(q)$  is the angle-dependent scattering intensity,  $I(0)$  is the intensity at zero angle,  $P(q)$  is the form factor of the primary particles measured using the same instrument, and  $q$  is the magnitude of the scattering wave vector, defined as:

$$q = \frac{4\pi n_w}{\lambda} \sin\left(\frac{\theta}{2}\right) \quad (4.2)$$

Here,  $\lambda$  is the wavelength of the incident light,  $n_w$  the refractive index of water, and  $\theta$  the scattering angle. Then, the average radius of gyration of the clusters,  $\langle R_g \rangle$ , was estimated using the Guinier plot of  $\langle S(q) \rangle$ :

$$-\ln(\langle S(q) \rangle) = \frac{3}{q^2} \langle R_g \rangle^2, \quad q \langle R_g \rangle < 1 \quad (4.3)$$

The power-law regime of  $\langle S(q) \rangle$  leads to an estimate of the fractal dimension,  $d_f$ :

$$\langle S(q) \rangle \propto q^{-d_f} \text{ for } \frac{1}{\langle R_g \rangle} \ll q \ll \frac{1}{a} \quad (4.4)$$

Here,  $a$  is the radius of the PVdF-HFP NPs, determined by the form factor,  $P(q)$ . Differential scanning calorimetry (DSC) measurements were conducted using a Q1000 instrument (TA Instruments) using 40  $\mu\text{L}$  crucibles in aluminum and a heating and cooling rate of 5  $^\circ\text{C min}^{-1}$  in a nitrogen atmosphere in the temperature range from -80 to 170  $^\circ\text{C}$ . Thermal gravimetric analysis (TGA) was conducted on a TGA/SDTA-851e instrument (Mettler-Toledo) using 70  $\mu\text{L}$  crucibles in alumina and a heating rate of 5  $^\circ\text{C min}^{-1}$  in air in the temperature range from 35 to

500 °C.

The ionic conductivity of the PCIL membrane was measured by AC impedance spectroscopy using a conductivity cell consisting of two stainless steel blocking electrodes. The AC impedance spectroscopy was carried out under the following conditions: PEIS (impedance under potentiostatic mode),  $\Delta V = 5$  mV, and a frequency range between 300 kHz and 1 Hz. SEM images were taken using a Gemini 1530 FEG instrument from Zeiss with a field-emission gun operated at 5 kV. The coating of the samples was performed using platinum. The electrochemical (EC) performance of the PCIL membrane was investigated by assembling the CR2032 coin cells, with lithium iron phosphate ( $\text{LiFePO}_4$ ) (LFP) and lithium metal as the cathode and the counter electrode, respectively, and the PCIL membrane as the separator. The EC tests were conducted on a Land CT2001A battery tester at a mass loading of the active materials per cell equal to 4 mg. The cell assembly was performed in a glovebox under argon atmosphere. The cells were cycled at various current densities in the voltage range 2.5-4 V (*versus* Li/Li<sup>+</sup>) at 60 °C. For charge/discharge performance characterization, 1C is defined as 170 mAh g<sup>-1</sup>.

## 4.3 Results and Discussion

### 4.3.1 Preparation of the PCIL membranes

The physical and chemical properties of the used PVdF-HFP NP dispersion are reported in the Appendix (Section 8.2.1, Table 8.1). The anionic surfactant has been removed by repeated cleaning with ion-exchange resin, Dowex MR-3, to reduce the colloidal stability of the PVdF-HFP NPs so as to facilitate the shear-driven aggregation. [16] After the cleaning, the conductivity of the dispersion becomes lower than  $10 \mu\text{S cm}^{-1}$ , and its surface tension is comparable to that of deionized water. It should be pointed out that the PVdF-HFP NPs are still very stable after cleaning, because of the fixed charges on the surface coming from the initiator.

As reported in Section 4.2, the intense shear-driven aggregation of the PVdF-HFP NPs was performed at a shear rate of  $4.8 \cdot 10^6 \text{ s}^{-1}$ , leading to the formation of a solidlike gel. To analyze the morphology of the clusters forming the gel, we redispersed the gel in deionized water, in the form of clusters. It should be mentioned that since the PVdF-HFP NPs are stable at rest, after passing through the microchannel the formed clusters are also stable (repulsive). The formation of a gel at the outlet of the microchannel is due to the crowding effect. Therefore, the gel can be easily redispersed in the form of individual clusters. The average radius of gyration,  $\langle R_g \rangle$ , and the mass fractal dimension,  $d_f$ , of the PCs are measured using the SALS instrument, Mastersizer 2000. [56, 150] Figure 4.2a shows the average structure factor,  $\langle S(q) \rangle$ , as a function of the magnitude of the scattering wave vector,  $q$ . From the  $\langle S(q) \rangle$  curve, the Guinier region gives  $\langle R_g \rangle = 28 \mu\text{m}$ , and the power-law region covers a  $q$  range of almost 2 orders of magnitude, indicating that the clusters can be well-considered as fractal objects. The slope of the power-law region leads to the estimate of  $d_f = 2.5$ , which is typical of the clusters formed under intense shear. [44]

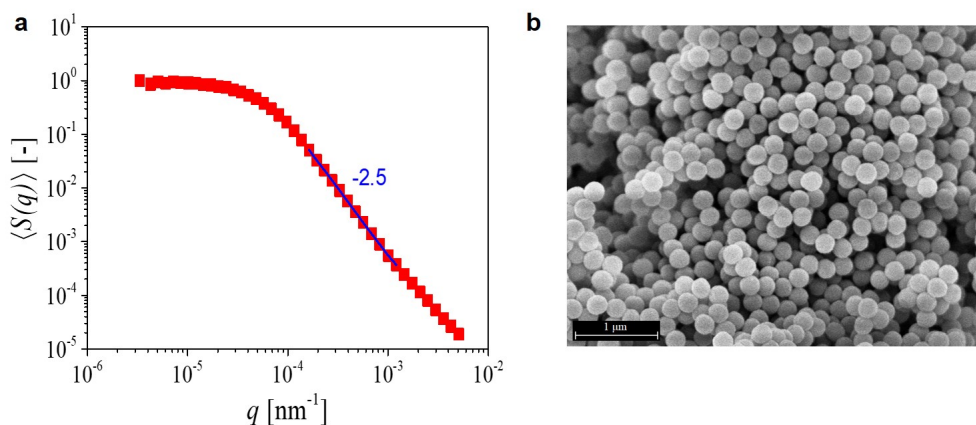


**Figure 4.2:** (a) Average structure factor,  $\langle S(q) \rangle$ , of the clusters forming the gel as a function of the scattering angle. (b) SEM image showing the morphology of the dried PC (scale bar:  $1 \mu\text{m}$ ).

When the gel is dried, all the clusters stick together, and the identity of the individual clusters forming the gel is lost. Therefore, the size of the PCs would depend on the milling extent, and in this work the dried PCs, whose size was smaller than  $63 \mu\text{m}$ , were collected from sieving. The SEM image of the dried PCs is shown in Figure 4.2b, representing the typical morphology of dried clusters with high porosity. It should be mentioned that since the gel is formed at the particle volume fraction,  $\phi = 18\%$ , the theoretical porosity (or void fraction) in the gel should be  $\Phi = 1 - \phi = 82\%$ . However, during the drying, certain restructuring inside the clusters occurs, which reduces the porosity. On the other hand, it will be seen in the following discussion on the membrane preparation that the porosity in the dried clusters is still very high, at least  $\Phi = 70\%$ . The dried PCs were then mixed with the IL solution at different mass fractions to obtain a PC/IL slurry, as described in the experimental section. The slurry was kept at rest overnight to allow the IL solution to impregnate the pores of the PCs, and then hot-pressed to form the membrane. The pressing temperature is chosen to be close to, but lower than, the melting point ( $T_m$ ) of the polymer to allow the

polymer particles to have slight interpenetration during the pressing. Since the  $T_m$  for PVdF-HFP is approximately 130 °C, as measured by DSC (Figure 8.4 and Table 8.2 in the Appendix, Section 8.2.2), we found that a pressing temperature lower than 100 °C is insufficient to form a homogeneous and continuous membrane and that the optimal pressing temperature is 120 °C. Figure 4.3 shows an example of the membrane formed by hot-pressing at 120 °C and 10 kN for 5 min, at the mass ratio PC/IL = 30/70.



**Figure 4.3:** Freestanding, transparent, 50  $\mu\text{m}$  thick PCIL membrane formed *via* hot-pressing.

It is seen that, after removal of the aluminum sheets, a freestanding, homogeneous, and transparent membrane is obtained. Since the formed membrane is based on the PC/IL slurry, it is here referred to as the PCIL membrane. The thickness of the PCIL membrane is measured with a digital caliper, being approximately 50  $\mu\text{m}$ . It was observed that the thickness after pressing depends solely on the applied pressure and is not influenced by the amount of sample. Therefore, the size of the membrane can be simply varied by varying the mass of the slurry

to be pressed. The formed membranes are stored in dried nitrogen atmosphere to avoid water absorption. The thermal stability of the PCIL membrane is evaluated by thermal gravimetric analysis (TGA) and compared in Figure 4.4 with that of the polymer, PVdF-HFP, the ionic liquid solution, LiTFSI-Pyr13TFSI, and the conventional organic electrolyte, 1.0 M LiPF<sub>6</sub> in EC/EMC = 50/50 (vol %). Let us define the decomposition temperature ( $T_d$ ) as the temperature corresponding to 10% weight loss, and from the results in Figure 4.4, we have  $T_d = 451, 402,$  and  $383$  °C for the polymer, the ionic liquid solution, and the membrane, respectively. In particular, the membrane is stable up to  $325$  °C with no material loss before the onset of the decomposition region, indicating that the membrane absorbed a negligible amount of water (curve 3 in Figure 4.4). Moreover, the membrane exhibits 70% weight loss in the same temperature range as the ionic liquid solution. This value is expected because the PCIL membrane is prepared at the PC/IL ratio of 30/70, and the 70% weight loss results from the used IL solution. As already observed by Sirisopanaporn *et al.*, [147] this result indicates that the IL solution is penetrated in the pores of PVdF-HFP clusters with no significant interaction with the polymer. For the conventional organic electrolyte, the decomposition temperature in Figure 4.4 (curve 4) is  $T_d = 75$  °C, and most of the mass is lost below  $200$  °C. This last aspect highlights why the researchers have made great effort to move toward solid electrolytes and particularly toward IL-based systems, which have much higher thermal stabilities.

It was found that the internal structure of the PCIL membrane cannot be clearly visualized if the SEM image is taken directly from the membrane sample, because of the excessive charging effect of the IL. Therefore, to visualize its structure *via* SEM, we removed the IL solution through repeated washing of the sample with dichloromethane (DCM). According to the safety data sheet provided by the producer, the IL used in this work has good solubility in acetone or in DCM, which

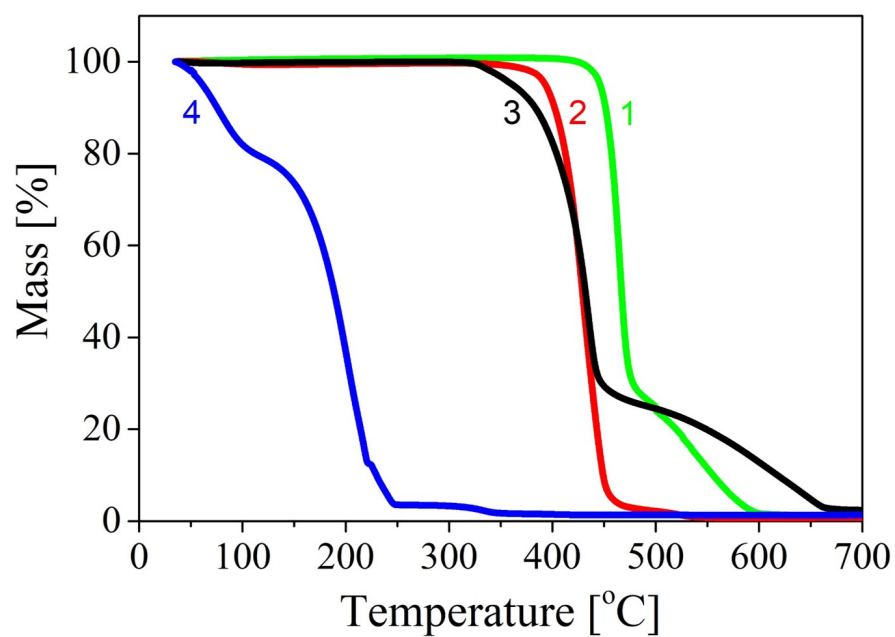


Figure 4.4: TGA profiles of PVdF-HFP (curve 1), LiTFSI-Pyr13TFSI (curve 2), PCIL membrane at PC/IL = 30/70 (curve 3), and conventional organic electrolyte, 1.0 M LiPF<sub>6</sub> in EC/EMC (curve 4).

was confirmed by adding the IL to DCM. For PVdF-HFP, the producer declares that it is readily soluble in acetone but not in DCM, and this was also confirmed by our tests. Thus, using DCM to wash the IL from the PCIL membrane does not change the internal structure of the separator. Figure 4.5 reports the cross-section of the PCIL membrane, which was prepared by breaking the membrane after immersion in liquid nitrogen, to preserve the structure. It can be seen that although the PCs are deformed and linked together after the hot-pressing, the porosity remains high. This is understandable when one considers that the IL solution is incompressible and that it has penetrated in the inner and outer region of the PCs, and during the hot-pressing, the total porosity remains basically unchanged. On the other hand, because of the deformation of all the PCs, the shape of the pores and the pore size distribution change substantially after hot-pressing. From Figure 4.5, although the primary particles of the PCs look deformed, part of their identity can still be observed. This proves that the polymer particles did not fully melt during hot-pressing. Furthermore, it is possible to observe that this process leads to the formation of a continuous polymer matrix hosting the IL in its interconnected pores, thus forming a bicontinuous structure.

### **4.3.2 Electrochemical characterization of the PCIL membranes**

The ionic conductivity of the PCIL membrane prepared at PC/IL = 30/70 was measured by AC impedance spectroscopy in the frequency range from 300 kHz to 1 Hz at different temperatures, and the results are reported in Table 4.1. As can be seen, the ionic conductivity of the PCIL membrane increases from 0.51 to 2.29 mS cm<sup>-1</sup> as the temperature increases from 25 to 80 °C. The increase of ionic conductivity with temperature is typical of the IL-based GPEs, mainly because of reduced viscosity. The obtained values are higher than or comparable to those



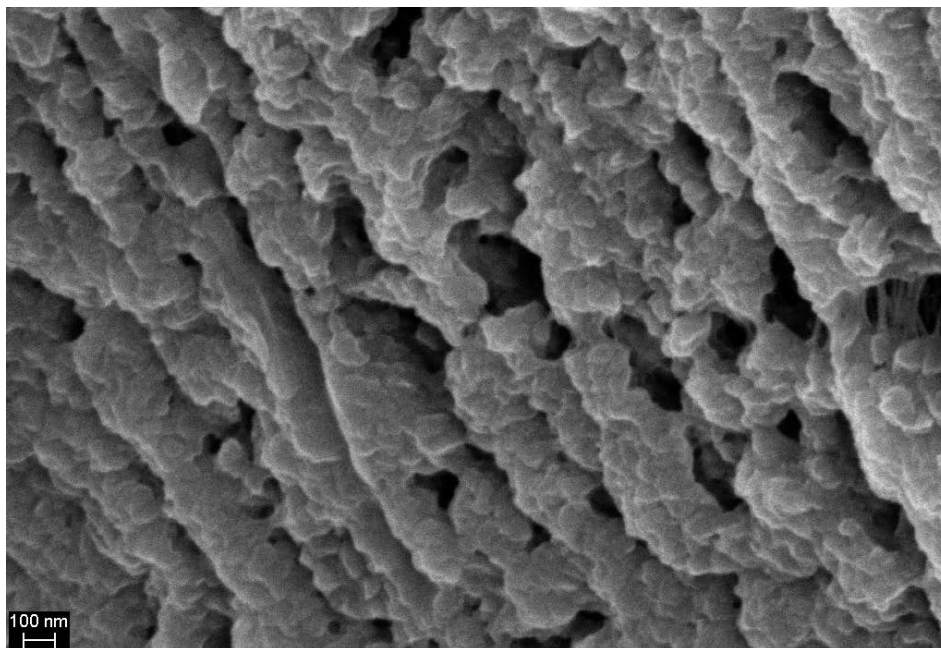


**Figure 4.5:** SEM image of the cross-section of the PCIL membrane prepared at PC/IL = 30/70, after removal of the IL solution with DCM.

previously reported in the literature for the GPE membranes based on PVdF-HFP and ionic liquids. [124,147,148,151–153] Guyomard-Lack *et al.* [154] prepared membranes through organic-solvent-based casting, with the same IL solution, but somewhat different polymer (PVdF-*co*-HEA), together with SiO<sub>2</sub>. From their results, for a comparable system with 70 wt.% of the IL solution, the measured conductivity was approximately 0.7 mS cm<sup>-1</sup> at 25 °C. This value is slightly higher than that shown in Table 4.1, and this could result from the presence of SiO<sub>2</sub>, which is believed to improve the ionic conductivity. [143,145,155] It is practically accepted that good electrochemical performances of a LIB, in terms of capacity and stability, require a value of at least 1 mS cm<sup>-1</sup> for the ionic conductivity. This means that, for the developed PCIL membrane, on the basis of the results in Table 4.1, an operating temperature higher than 50 °C has to be selected.

The data of the ionic conductivity in Table 4.1 can be correlated with the

**Table 4.1: Ionic conductivities of the PCIL membrane at the PC/IL ratio of 30/70, measured at different temperatures, and the corresponding values of the parameters in Equation 4.6.**

	Ionic conductivity [mS cm <sup>-1</sup> ]					$E_a$ [eV]	$T_0$ [K]
	25 °C	40 °C	55 °C	70 °C	80 °C		
PCIL	0.51	0.78	1.22	1.77	2.29	0.13	101

Vogel–Tammann–Fulcher (VTF) equation: [156]

$$\sigma(T) = AT^{-0.5} \exp\left(\frac{B}{T - T_0}\right) \quad (4.5)$$

where  $A$  is the pre-exponential factor,  $T_0$  is a reference temperature at which the free volume vanishes, and the ionic mobility goes to zero, and  $B$  is a pseudoactivation energy for the charge-carrier motion. The VTF equation represents a phenomenological way to interpret ion transport (or viscosity) data in amorphous polymer electrolytes above the glass transition temperature. [131,157] Empirically, the VTF parameters can be obtained by fitting the conductivity data in terms of the linearized relationship: [158]

$$\log_{10}(\sigma T^{0.5}) = \log_{10}(A) - 0.43 \left(\frac{E_a}{k_B(T - T_0)}\right) \quad (4.6)$$

where  $E_a$  is the activation energy and  $k_B$  the Boltzmann constant. A comparison between the experimental data for the PCIL membrane and the fitting of Equation 4.6 is shown in Figure 4.6, and the obtained values for  $E_a$  and  $T_0$  are reported in the last columns of Table 4.1. The good agreement with the experimental data and the obtained small value for  $E_a$  (= 0.13 eV) indicate no particular restrictions to the motion of ions within the membrane. [124,131,159]

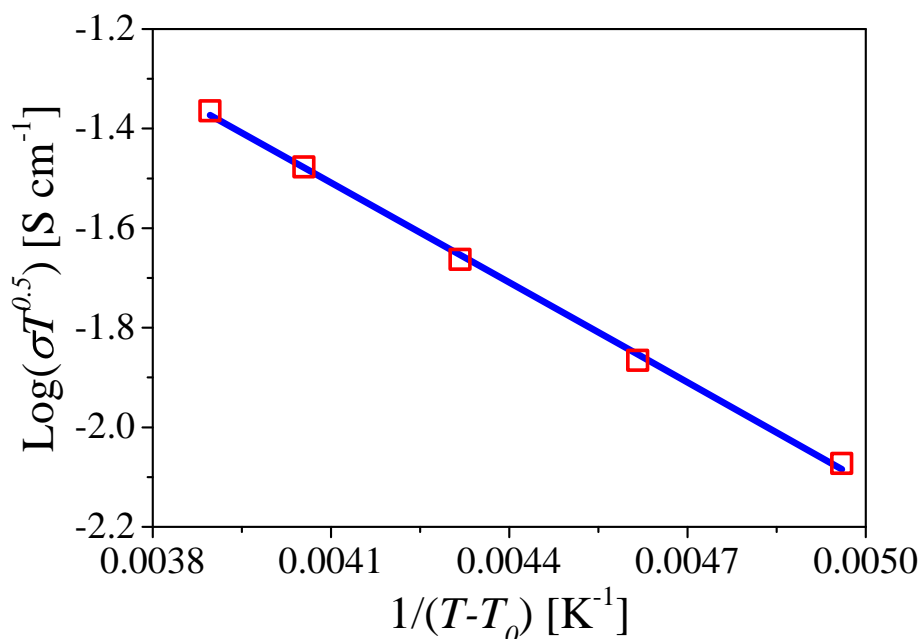


**Figure 4.6:** Ionic conductivity data in Table 4.1 treated and fitted with the linearized VTF equation.

The performance of the PCIL membrane is investigated by assembling Li/PCIL/LFP coin cells. Three types of PCIL membranes have been prepared at the PC/IL ratio of 40/60, 35/65, and 30/70, respectively. The normalized discharge capacity, measured at 60 °C, as a function of the applied current density for the three PCIL membranes is shown in Figure 4.7. The normalized discharge capacity is defined as the measured discharge capacity divided by the initial discharge capacity at 0.2C. It can be observed from Figure 4.7 that, for the PCIL membrane at PC/IL = 40/60, the battery starts to lose its performance already at 0.5C, retaining only 92% of the initial discharge capacity. This becomes even more severe at 1C and 2C, where the capacity drops down to 44% and 20% of the initial capacity, respectively. When the current density is reduced back to 0.5C, although the battery shows a good recovery up to 89% for the first cycle, the performance drops down to 84% in the next 4 cycles, indicating limited stability over time. The cell assembled with

the PCIL membrane at PC/IL = 35/65 shows better performances with respect to that at PC/IL = 40/60. The discharge capacity remains good (>95% of the initial one) up to 1C, but it drops down to 51% at 2C. When the current density is reduced back to 0.5C, the battery shows not only a good recovery (up to 99%) but also good cycle stability. The best performance is given by the cell assembled with the PCIL membrane at PC/IL = 30/70, which can retain more than 88% of the initial capacity even at current density of 2C. The cell shows basically complete recovery when the current density returns to 0.5C (99% and 96% of the initial capacity at 0.5C and 0.2C, respectively).

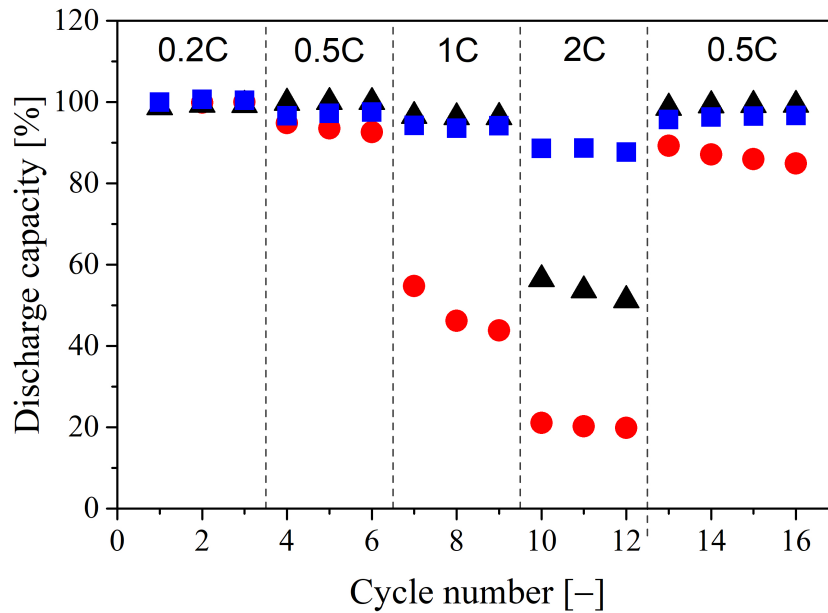


**Figure 4.7:** Normalized discharge capacity, measured at 60 °C, for the assembled Li/PCIL/LFP cells with the PCIL membrane at PC/IL = 40/60 (red circles), 35/65 (black triangles), and 30/70 (blue squares), respectively.

For the best case above, *i.e.*, the cell assembled with the membrane at PC/IL = 30/70, the specific discharge capacity and the efficiency of the electrochemical cycles are reported in Figure 4.8. It is seen that, at low current densities (0.2C and

0.5C), the measured capacities (150 and 145 mAh g<sup>-1</sup>) are close to the theoretical one for the LFP-based batteries (170 mAh g<sup>-1</sup>). Even at 1C and 2C rates, the performance is still very good, reaching a capacity of 141 and 132 mAh g<sup>-1</sup>, respectively. After the cycles at high current densities, the specific discharge capacity of the battery is measured again at 1C, and it still reaches a value of 139 mAh g<sup>-1</sup>, indicating that negligible deterioration occurs for the PCIL membrane at high rates. The battery efficiency in Figure 4.8 (blue squares) is defined as the ratio between the discharge and charge capacities, and it is >90% in the entire range of the C-rates. The obtained values are higher than those previously reported in the literature for the Li/LFP-based batteries using the IL-based GPE membrane as the separator. [124, 151]

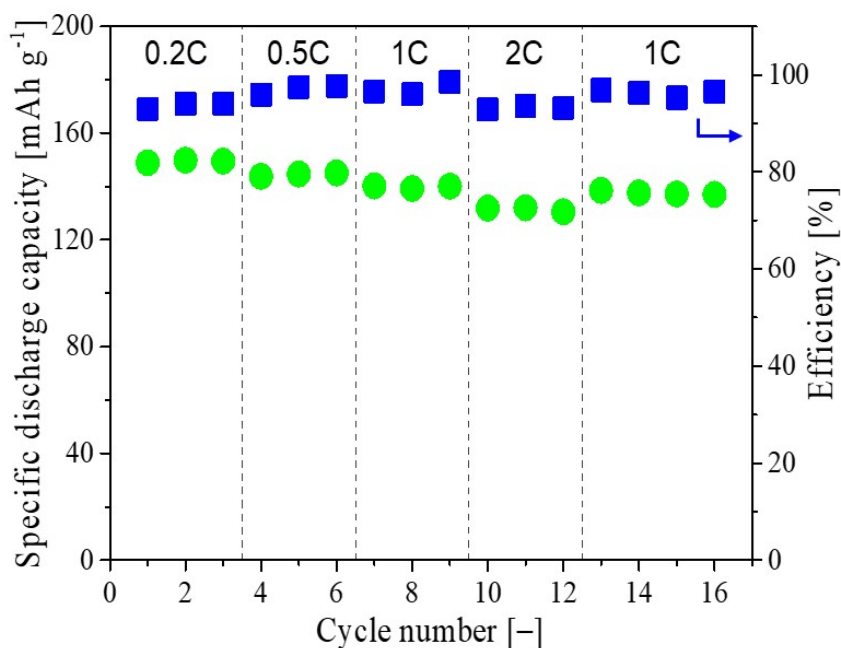


**Figure 4.8:** Specific discharge capacity (green circles) and electrochemical efficiency (blue squares), at 60 °C, for the assembled Li/PCIL/LFP cell with the PCIL membrane at PC/IL = 30/70.

From the above results in Figures 4.7 and 4.8, it is evident that the performance

of the cell, in terms of the stability at high C-rates and capacity retention, increases as the mass fraction of the IL solution in the PCIL membrane increases. This result is understandable when one considers that the PCs are fractal objects, and all the pores in a PC are interconnected. When the mass fraction of the IL solution is low, the IL solution occupies only part of the pore volume in the PC, and the remaining can be considered as dead volume. The presence of the latter leads to three consequences: (1) the number of channels for the transport of lithium ions is reduced. (2) Some of the pores are not interconnected (interrupted by the empty pores). (3) The total pore volume will be further reduced after hot-pressing, because of the fact that the empty pores are compressible. All these factors explain why the performance increases as the mass fraction of the IL solution in the PCIL membrane increases. At the optimal conditions, all the pores are filled with the IL solution and thus interconnected, forming a real bicontinuous membrane (both the IL solution and the PVdF-HFP network are continuous). Therefore, although uneven lithium deposition and dendrite formation may occur and close some of the channels, since all the pores form a continuous phase, the lithium ions can always find available channels to cross the membrane. In principle, we can continue increasing the mass fraction of the IL solution in the PCIL membrane. In reality, we found that a PCIL membrane prepared at PC/IL = 20/80 has poor homogeneity and integrity, thus being mechanically unfeasible for its application. A picture of the PCIL membrane obtained at PC/IL = 20/80 is shown in Figure 8.4 of the Appendix (Section 8.2.3). This result indicates that if a too large mass fraction of the IL solution is used, the PCs in the PC/IL slurry cannot interconnect to form a continuous membrane, as the IL solution not only fills the pores of the PCs but also partially occupies the space among the PCs, leading to disconnection of the PCs during the hot-pressing. In addition, the good membrane formed at PC/IL = 30/70 reveals that the porosity of the PCs is at least 70% (but certainly

smaller than 80%). It is therefore concluded that, for the given system, the proper conditions for the preparation of the PCIL membranes *via* hot-pressing are PC/IL = 30/70 and  $T = 120\text{ }^{\circ}\text{C}$ , which result in not only sufficient integrity and good mechanical strength of the PCIL membrane but also good performance of the assembled battery.

The long-term cycling stability of the cell assembled with the PCIL membrane at PC/IL = 30/70 as the separator has been tested at 0.5C and  $60\text{ }^{\circ}\text{C}$  for more than 200 cycles. The results are shown in Figure 4.9 and compared with those of Shin *et al.* [151] for a battery prepared using rather similar materials. As can be seen, the specific discharge capacity after 200 cycles still retains 95% of the initial capacity ( $149.5\text{ mAh g}^{-1}$ ). After 225 cycles, the battery performance decreases significantly to  $135\text{ mAh g}^{-1}$  (*i.e.*, 90% of the initial value). The Coulombic efficiency stays always very close to unity throughout the entire stability test. To our knowledge, the obtained high discharge capacities at high current densities reported in Figure 4.8 and the great stability over more than 200 cycles at 0.5C in Figure 4.9 are superior to the performance reported in the literature for the same type of batteries using the IL-based GPE membranes. [124,151,160–162] Ferrari *et al.* [124] reported the performances of a Li/GPE/LFP cell, where the GPE membrane was prepared with 30% PVdF-HFP and 70% PyrA<sub>1201</sub>TFSI-LiTFSI *via* a conventional casting technique using acetone as the solvent. Despite the battery showing good results at room temperature and at low current densities (0.05C and 0.1C), it exhibited poor discharge capacities at higher current densities ( $120\text{ mAh g}^{-1}$  at 0.2C;  $75\text{ mAh g}^{-1}$  at 0.5C). Shin *et al.* [151] prepared a  $100\text{ }\mu\text{m}$  thick, PEO/Pyr13TFSI-based membrane *via* hot-pressing, where PEO was purchased and used directly, without proper control of its porosity. It was used to assemble a half-coin cell with lithium and LFP as electrodes, which was tested at 0.05C and  $40\text{ }^{\circ}\text{C}$ , and the results are reproduced in Figure 4.9. As can be seen, the discharge capacity is initially similar

to that of our cell, but the cycling stability is significantly lower, also considering that the current density was 0.05C, while ours is 0.5C. At higher current densities the assembled cell showed low capacity retention. Stepniak *et al.* [160] prepared a IL-GPE-based membrane through solution casting and *in situ* UV polymerization. The assembled Li/IL-GPE/LFP cell showed good cycling performance in 50 cycles at 0.05C and 25 °C, but at high current densities its discharge capacities are much lower than those in Figure 4.8. Tong *et al.* [161] prepared a PVdF-HFP-based membrane through electrospinning, in which the IL solution was then impregnated. The obtained GPE was tested also by assembling a Li/GPE/LFP cell. Again, though the cycling stability was good for 50 cycles at 0.1C and 25 °C, at high current densities, the discharge capacities drop substantially. Costa *et al.* [163] evaluated the performance of a separator made of PVdF and produced by solvent casting together with an imidazolium-based ionic liquid ( $[\text{C}_2\text{mim}][\text{NTf}_2]$ ). The conductivity at room temperature was 0.23 mS cm<sup>-1</sup>, and the initial discharge capacity in a Li/C-LFP half-cell was about 75 mAh g<sup>-1</sup>, and after 10 cycles at 0.2 C and 25 °C, the capacity retention reduced to 60%. It should be mentioned that apart from the polymer matrix, the IL solutions and the testing temperatures used by Stepniak *et al.*, [160] Shin *et al.*, [151] and Costa *et al.* [163] are also different from ours, and direct comparison of their results here becomes difficult. On the other hand, the small dependence of the discharge capacity on the current density from our PCIL membrane in Figure 4.8 is seldom observed in the literature for similar systems. We believe that the excellent performance of our PCIL membrane at high current densities is related to its high porosity (>70%), homogeneously distributed pores, and well-controlled pore dimension (all in the submicron range, as it can be seen in Figure 4.5). More importantly, the pores formed in the fractal clusters are all interconnected and accessible for the IL solution, thus forming a continuous phase within the membrane without any dead volume.



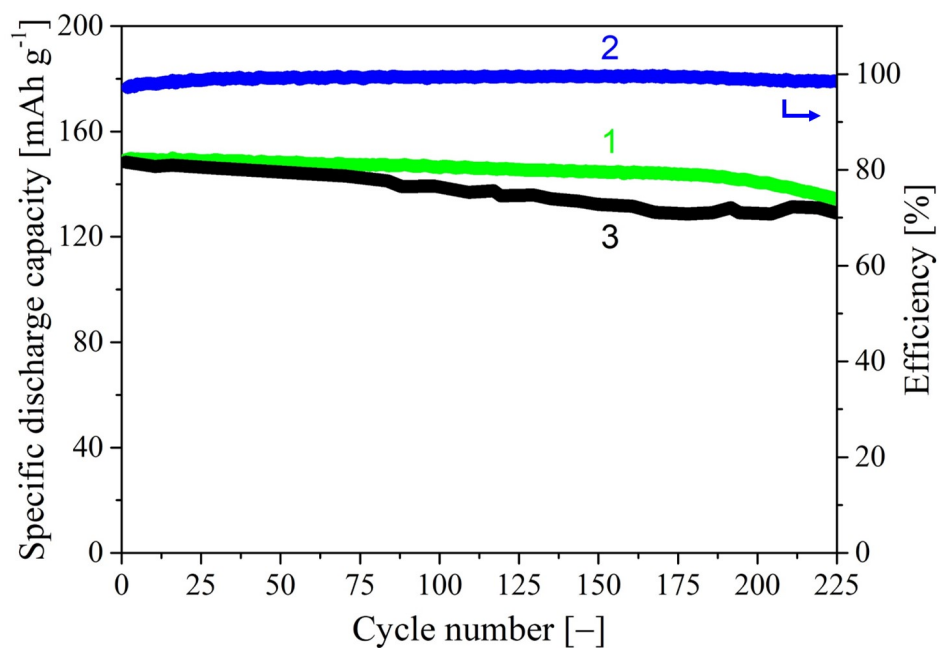


Figure 4.9: Specific discharge capacity (curve 1) and Coulombic efficiency (curve 2) as a function of cycle number, at 0.5C and 60 °C, for the assembled Li/PCIL/LFP cell with the PCIL membrane at PC/IL = 30/70. Curve 3 is reproduced from the work of Shin *et al.* [151] where the capacity was measured at 0.05C and 40 °C.

## 4.4 Conclusion

We have developed a methodology to prepare freestanding, polymer (PVdF-HFP)/ionic-liquid-based (Pyr13TFSI-LiTFSI), electrolyte membrane for LIBs, with well-controlled submicron pores and high porosity. This approach does not involve any organic solvent and starts with direct conversion of the aqueous dispersion of the PVdF-HFP NPs to a solidlike gel through intense shear-driven aggregation. Then, the gel is dried and ball-milled, forming dried polymer clusters (PCs), which are typical fractal objects, thus possessing well-controlled submicron pores and high porosity. Subsequently, the PCs are mixed with the ionic liquid (IL) solution, and the mixture is hot-pressed to form a membrane, referred here to as the PCIL membrane. Because of the complete interconnection of the pores in the membrane, a property of fractal objects, the incorporated IL solution and the polymer matrix form a bicontinuous structure, and the formed transparent membrane presents good ionic conductivity. A PCIL membrane of 50  $\mu\text{m}$  prepared at the PC/IL mass ratio of 30/70 has been used as the separator to assemble a half-coin cell having  $\text{LiFePO}_4$  and Li as the cathode and the counter electrode, respectively. The electrochemical performance of the cell has been tested at 60  $^\circ\text{C}$ , and it showed excellent results not only at low but also at high current density. The performance increases as the mass ratio of the IL solution in the membrane increases, because of the increased porosity and ion diffusion medium. On the other hand, a too large mass ratio of the IL solution may lead to the amount of the polymer clusters being insufficient to form a freestanding membrane. In the present case, the PC/IL mass ratio should be smaller than 20/80. It is worth pointing out that there could be other ILs that show superior ionic conductivities, and their applications in our PCIL separator may lead to better performances at lower temperatures. However, the focus of the present work is on the design of the morphology of the separator and not on the optimization of the IL/Li salt system. The developed

#### 4.4. CONCLUSION

---

design methodology is very versatile and could be easily applied to systems with different ILs to study the performance of the PCIL membranes at low and high temperatures.



## Chapter 5

# Effect of SiO<sub>2</sub> Nanoparticles on the Performance of PVdF-HFP/Ionic Liquid Separator for Lithium-Ion Batteries

---

This chapter is based on the following publication: S. Caimi, A. Klaue, H. Wu, M. Morbidelli, Effect of SiO<sub>2</sub> Nanoparticles on the Performance of PVdF-HFP/Ionic Liquid Separator for Lithium-Ion Batteries, *Nanomaterials*, **2018**, 8(11), 926, DOI: 10.3390/nano8110926.

## 5.1 Introduction

Recent large-scale power applications of lithium-ion batteries (LIB) including electric vehicles and emerging smart grids require long cycle life, low impact on the environment and high reliability and safety. [85–89, 164] Current technologies are based on the use of organic liquid electrolytes, which guarantee high ionic conductivity at low temperatures and long cycle stability. However, they are also highly volatile, toxic and thermally unstable and may leak out of the battery under abnormal operations. [95, 99–105] One of the most promising alternatives to replace liquid electrolyte is the employment of ionic liquids (ILs), which possess high ion density and are characterized by high thermal stability. [109–115, 118, 119, 164, 165] Among the several existing ILs, those based on pyrrolidinium and in particular Pyr13TFSI are often considered since they exhibit one of the lowest viscosities and are chemically inert towards the cell components. [95, 112, 135, 136] The main drawback of the use of ILs is the limited ionic conductivity at low temperature, especially when mixed with the host polymer to form the separator. One possibility to increase the ionic conductivity at low temperatures is the addition of inorganic nanoparticles (NPs) such as  $\text{SiO}_2$ ,  $\text{Al}_2\text{O}_3$ ,  $\text{TiO}_2$  and  $\text{CeO}_2$ , to the polymer matrix. [143, 145, 166–168] These fillers can improve the conductivity by reducing the polymer crystallinity and by interacting with the ionic species in the electrolyte through Lewis acid-base interactions. [142, 155, 166, 169, 170] Moreover, it is well-established that the addition of inorganic NPs into the polymer matrix improves its mechanical stability, thus preventing thermal shrinkage and mechanical breakdown of the separator. [155, 171, 172] In order to maximize the effect of the added NPs, it is essential to disperse them in the polymer matrix uniformly and at the nanoscale level. [141, 173] To achieve this, in this work, we start from a dispersion of silica NPs in water and mix it with an aqueous dispersion of PVdF-HFP NPs. The binary dispersion is then subjected to shear-driven gelation by passing through a

microchannel where, if present alone, the polymer NPs undergo gelation whereas the silica NPs are shear-inactive (*i.e.*, they are stable and do not aggregate). As the process occurs in few milliseconds the silica NPs cannot escape from the polymer gel network and remain entrapped and dispersed uniformly in the polymer matrix. [45,149,150] Poly(vinylidene fluoride-*co*-hexafluoropropylene) (PVdF-HFP) is chosen as it possesses high dielectric constant, it is chemically compatible with the electrode materials, and it is characterized by low crystallinity. [141,143–145] The method to form a freestanding, uniform and transparent membrane through hot-pressing, starting from the polymer/filler clusters and the IL has been developed earlier in our group and described elsewhere. [174] The effect of the presence of silica NPs in the IL-based membrane is investigated in terms of ionic conductivity and electrochemical cyclability.

## 5.2 Experimental

### 5.2.1 Materials

The following chemicals have been employed without further treatments. Sodium dodecyl sulphate (SDS, purity 99%) and N-Propyl-N-Methylpyrrolidinium bis(trifluoromethane-sulfonyl)-imide (Pyr1308b, purity 99.5%) were purchased from Apollo Scientific and Solvionic (Toulouse, France), respectively. The water dispersion of PVdF-HFP NPs, the amorphous silica powder Tixosil 365 and bis(trifluoromethane)sulfonamide lithium salt (LiTFSI) were provided by Solvay (Bollate, Italy). Ion-exchange resin (Dowex MR-3 hydrogen and hydroxide form) was purchased from Sigma-Aldrich. The lithium iron phosphate (LFP) cathode material is commercial grade Life Power P2 from Clariant. Before assembling, the positive electrode and the separator were dried overnight under vacuum at 130 and 60 °C, respectively.

### 5.2.2 Methods

To form a suitable dispersion, Millipore water is added to the silica powder to reach a solid fraction of 30% and the mixture is mechanically stirred and repeatedly sonicated using a digital sonifier from Branson. Eventually, the dispersion is centrifuged at 2000 rpm for 10 minutes to remove the remaining large clusters. The binary dispersion of PVdF-HFP and  $\text{SiO}_2$  NPs is prepared by adding the silica NP dispersion dropwise to the PVdF-HFP NP dispersion under agitation. As the addition of  $\text{SiO}_2$  NPs may destabilize the PVdF-HFP dispersion due to a repartition of the adsorbed surfactant between the two species, some additional SDS is added (0.2% with respect to the solid content of the dispersion). The content of the added silica is evaluated as mass percentage with respect to the mass of polymer.



## 5.2. EXPERIMENTAL

---

A high-shear device, HC-5000 (Microfluidics, Westwood, Massachusetts, United States), connected to a L30Z microchannel with a width of 300  $\mu\text{m}$ , a rectangular cross section of  $5.26 \cdot 10^{-8} \text{ m}^2$  and a length of 5.8 mm was used to perform shear-driven gelation of the PVdF-HFP/SiO<sub>2</sub> NPs. The operating conditions for the gelation and subsequent drying to obtain the polymer-silica clusters (PSiCs) are reported elsewhere. [174]

The IL solution consisted of a 0.5 M solution of LiTFSI salt dissolved into Pyr13TFSI. The obtained clusters were mixed with the IL solution at a mass fraction of PSiC/IL equal to 30/70 wt.%, following the procedure previously reported. [174] The slurry was then transferred between two aluminum sheets in a preheated hydraulic hand-press (Rondol, Strasbourg, France) and hot-pressed at 120 °C and 10 kN to form the separator. The cooling phase was performed while holding the pressure. The formed membrane (electrolyte) is here referred to as the PSiCIL membrane.

Small-angle light scattering (SALS) measurements were taken using a Mastersizer 2000 (Malvern, United Kingdom) equipped with a laser having a wavelength  $\lambda = 633 \text{ nm}$  to characterize the obtained clusters in terms of their average radius of gyration,  $\langle R_g \rangle$ , and their fractal dimension,  $d_f$ , following the procedure reported elsewhere. [56, 175] Measures of dynamic light scattering and zeta potential were conducted using Zetasizer Nano ZS 3600 from Malvern Instruments.

Differential scanning calorimetry (DSC) measurements were conducted using Q1000 instrument (TA Instruments) using 40  $\mu\text{L}$  crucibles in aluminum and a heating and cooling rate of 5 °C  $\text{min}^{-1}$  in a nitrogen atmosphere in the temperature range from 80 to 200 °C. The solid content is measured using a HG53 Halogen Moisture Analyzer (Mettler-Toledo). Powder XRD measurements were carried out with a X'Pert PRO-MPD diffractometer (PANalytical). Data were recorded in the 5-70°  $2\theta$  range with an angular step size of 0.05° and a counting time of 0.26 seconds per

step. The peaks at  $2\theta = 18.2, 20.0, 26.6$  and  $38.8$  correspond to the (100), (020), (110) and (021) crystalline peaks of PVdF-HFP, respectively. [176]

AC impedance spectroscopy was used to measure the ionic conductivity of the PSiCIL membranes using a conductivity cell consisting of two stainless steel blocking electrodes. The measurement was carried out under PEIS conditions (impedance under potentiostatic mode),  $\Delta V = 5$  mV and frequency range from 300 kHz to 1 Hz. The resistance of the polymer electrolyte was measured and the ionic conductivity ( $\sigma$ ) was obtained as follows:

$$\sigma = \frac{d}{R_b S} \quad (5.1)$$

where  $d$  is the thickness of the separator,  $R_b$  the bulk resistance and  $S$  the area of the stainless steel electrode.

SEM images were taken using a Zeiss Leo 1530 (Zeiss, Oberkochen, Germany) with field emission gun operated at 5 kV. The coating of the samples was performed using platinum. TEM images were performed using a Morgagni 268 from FEI equipped with a tungsten emitter operated at 100 kV.

The electrochemical (EC) performance of the PSiCIL membrane was investigated by assembling the CR2032 coin cells, with lithium iron phosphate (LFP) and lithium metal as the cathode and the counter electrode, respectively, and the PSiCIL membrane as the separator. The EC tests were conducted on a Land CT2001A battery tester at a mass loading of the active materials per cell equal to 4 mg. The cell assembly was performed in a glove-box under argon atmosphere. The cells were cycled at various current densities in the voltage range 2.5-4 V (*versus* Li/Li<sup>+</sup>) at 60 °C. For charge/discharge performance characterization, 1C is defined as 170 mAh g<sup>-1</sup>.

## 5.3 Results and Discussion

### 5.3.1 Preparation of the P*SiCIL* membranes

The procedure to obtain the silica dispersion is reported in the experimental section. Typical properties of the obtained dispersion of SiO<sub>2</sub> NPs in water are summarized in Table 5.1.

**Table 5.1: Properties of the dispersion of SiO<sub>2</sub> NPs in water.**

	Average clusters diameter	PDI	Zeta potential
	[nm]	[-]	[mV]
Tixosil 365	160	0.19	-47.9

For the application at hand, the silica NPs have to be well-dispersed in water and should be negatively charged to maintain their stability while mixed with the negatively charged PVdF-HFP NPs. As reported in Table 5.1, these requirements are met by the silica NPs, showing an average diameter smaller than 200 nm and a negative potential larger than 40 mV (absolute value). In order to investigate the effect of pH, Figure 5.1a reports the average diameter and the zeta potential of the silica NPs in the pH range 6-12. To better appreciate the morphology of the silica NPs, Figure 5.1b reports a TEM image of the dried silica dispersion. From Figure 5.1a, it is seen that the dispersed SiO<sub>2</sub> NPs have a constant average diameter smaller than 200 nm and are negatively charged with the zeta potential ranging from -48 to -42 mV. Moreover, from Figure 5.1b, it is possible to recognize that the each silica NP is a nanocluster made of 10 nm silica primary particles.

The physical and chemical properties of the used PVdF-HFP NP dispersion are reported in the Appendix (Section 8.2.1, Table 8.1). In order to reduce the

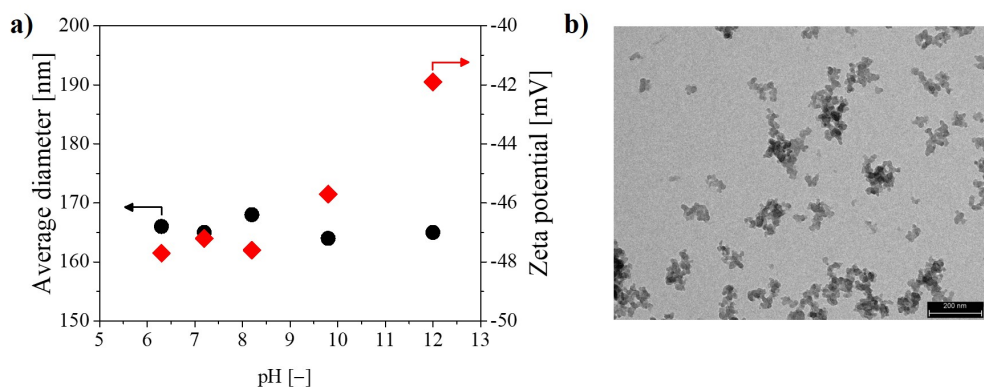


**Figure 5.1:** (a) Average diameter and zeta potential of the silica NPs as a function of pH in the silica dispersion. (b) TEM image of the dried silica NPs (scale 200 nm).

colloidal stability of the PVdF-HFP NPs so as to facilitate the shear-driven gelation, the anionic surfactant was removed by repeated washing with ion-exchange resin Dowex MR-3.

The polymer and filler dispersions are mixed as described in the experimental section and the binary system is subjected to intense shear by forcing it to pass through a microchannel so as to have rapid gelation of the polymer NPs with the typical fractal characteristics. Since the formation of the polymer gel network occurs in few milliseconds and the silica NPs are shear-inactive (*i.e.*, they do not aggregate under the given shear rate), the fillers, silica NPs, have no time to escape and remains entrapped in the formed matrix at a nanoscale level. In order to have complete capture of the silica nanoparticles, it is of utmost importance to obtain a compact gel after a single pass through the microchannel, as discussed elsewhere. [45,177] This depends on the solid content of the polymer/silica dispersion: the higher the solid content, the greater the compactness of the formed gel. In order to analyze the distribution of the silica NPs inside the polymer matrix, SEM pictures of the gel obtained from the microchannel are shown in Figure 5.2.

From Figure 5.2 it is evident that the shear-induced gelation is capable of

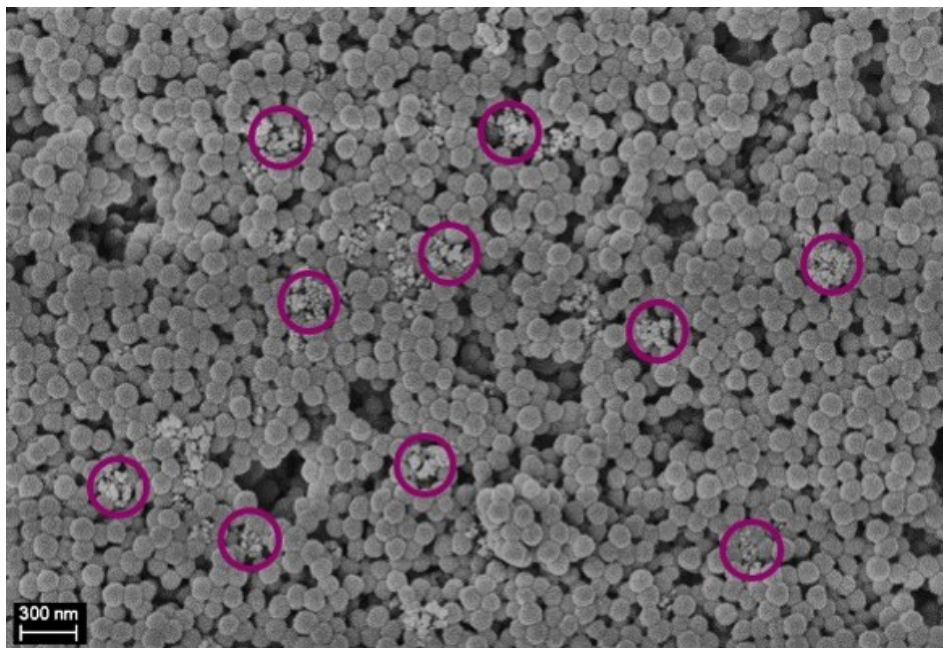


Figure 5.2: SEM picture of the silica NPs entrapped in the polymer matrix after a single pass through the microchannel (scale 300 nm). Some silica NPs are encircled in violet to be better visualized.

dispersing uniformly and randomly the silica NPs as fillers within the polymer matrix, where the silica NPs with respect to the PVdF-HFP NPs are clearly and easily distinguishable (whiter and smaller ones, encircled in violet in Figure 5.2). It is worth noticing that the fillers are uniformly dispersed at the nanoscale level (*i.e.*, the silica NPs are smaller than 200 nm). Moreover, it is possible to observe that also the PVdF-HFP NPs maintain their original identity. In order to investigate the physical properties of the pure polymer and of the composite material, DSC is performed. Figure 5.3 reports the results of the heating and cooling ramps of the dried gel at different contents of SiO<sub>2</sub>. The melting and crystallization temperatures as well as the crystallinity of the composite derived from the DSC heating and cooling curves are reported in Table 5.2.

**Table 5.2: Properties of the composite material at increasing amount of SiO<sub>2</sub>, derived from the DSC curves in Figure 5.3.  $T_m$ : melting temperature.  $T_c$ : crystallization temperature.  $\Delta H_m$ : enthalpy of melting.  $X_c$ : crystallinity.**

	$T_m$	$T_c$	$\Delta H_m$	$X_c$
	[°C]	[°C]	[J g <sup>-1</sup> ]	[%]
Pure	133.6	97.6	22.19	21.2
10% SiO <sub>2</sub>	132.8	100	18.21	17.4
20% SiO <sub>2</sub>	130.5	99.7	16.92	16.2
30% SiO <sub>2</sub>	130.6	99.6	15.66	14.9

The results reported in Table 5.2 show that the amount of SiO<sub>2</sub> NPs affects only slightly the melting and crystallization temperatures. The melting temperature of the pure polymer PVdF-HFP results in approximately 134 °C as derived from the maximum of the heating curve and progressively decreases with increasing

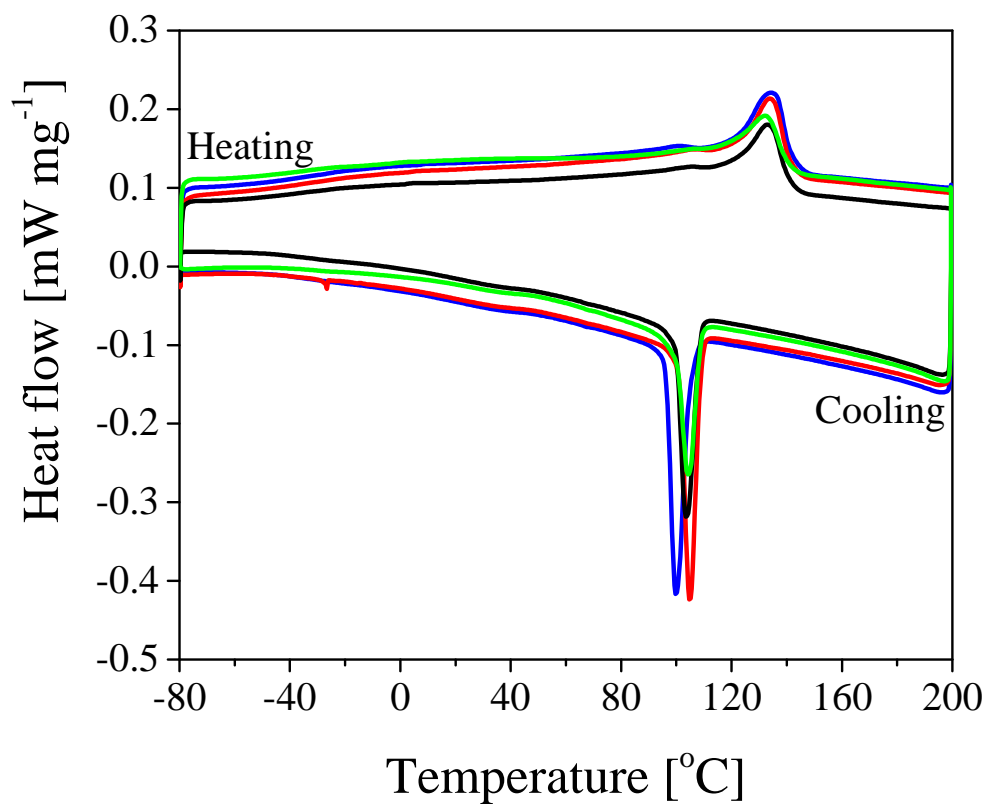


Figure 5.3: DSC of the composite gel obtained after one pass through the microchannel at different percentages of the fillers, silica NPs. Blue curve: PVdF-HFP; Red curve: PVdF-HFP + 10%  $\text{SiO}_2$ ; Black curve: PVdF-HFP + 20%  $\text{SiO}_2$ ; Green curve: PVdF-HFP + 30%  $\text{SiO}_2$ .

amount of SiO<sub>2</sub> to reach approximately 131 °C at 30 wt.% content of silica. The crystallization temperature, on the other hand, is measured from the minimum of the cooling curve, which is approximately 98 °C for the pure polymer and 100 °C for the composite material, independently of the amount of silica. Furthermore, the enthalpy of melting and the crystallinity significantly decrease with increasing content of SiO<sub>2</sub> NPs. These results are expected and are related to the hindered reorganization of the polymer chains due to the cross-linking centers formed by the interaction of Lewis acid groups with the polar groups (*i.e.*, the -F atoms of the polymer chains). This interaction can stabilize the amorphous structure and facilitates the transport of Li<sup>+</sup> ions (*i.e.*, the ionic conductivity), as observed by several authors. [166, 169, 170, 178, 179]

In order to measure the crystallinity of the polymer and to investigate the effect of the introduction of the SiO<sub>2</sub> NPs on it, XRD measurement are performed and the results are shown in Figure 5.4.

It is seen that the spectrum of the pure polymer confirms the partial crystallization of PVdF units in the copolymer and gives a semi-crystalline structure of PVdF-HFP. [143] Moreover, the crystallinity of the polymer has been considerably reduced upon the addition of silica NPs. The intensity of the crystalline peaks, indeed, decreases and broadens when increasing the amount of SiO<sub>2</sub>. This reduction in crystallinity is attributed to the changes of the chain conformation due to the presence of the silica NPs, which again facilitate higher ionic conduction. [180, 181] The dried PSiCs containing different percentages of SiO<sub>2</sub> are then mixed with the IL solution at a mass fractions PSiC/IL of 30/70 wt.% to obtain a slurry, as described in the experimental section. To allow full impregnation of the IL solution into the pores of the PSiCs, the slurry is left at rest overnight before being hot-pressed at 120 °C and 10 kN, as described in our previous work. [174] After the hot-pressing, it is possible to obtain a freestanding, homogeneous and transparent



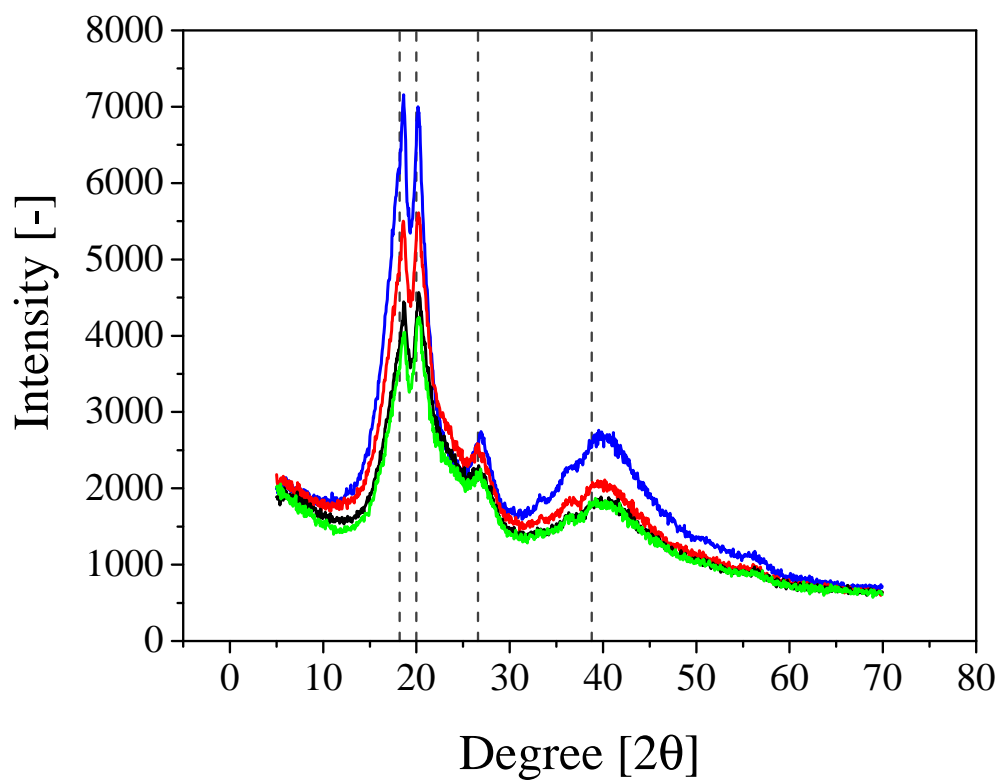


Figure 5.4: XRD of the composite gel obtained after one pass through the microchannel at different percentages of the fillers, silica NPs. Blue curve: PVdF-HFP; Red curve: PVdF-HFP + 10% SiO<sub>2</sub>; Black curve: PVdF-HFP + 20% SiO<sub>2</sub>; Green curve: PVdF-HFP + 30% SiO<sub>2</sub>.

50  $\mu\text{m}$  thick IL-based membrane (referred as P*SiCIL* membrane) containing the silica NPs at a nanoscale level. To prevent water absorption, the P*SiCIL* membranes are stored in dried nitrogen atmosphere.

### 5.3.2 Electrochemical characterization of the P*SiCIL* membranes

The ionic conductivity of the P*SiCIL* membranes was measured by AC impedance spectroscopy in the temperature range from 25 to 80 °C at increasing percentages of silica (with respect to the polymer) in the P*SiCs*, and the results are reported in Figure 5.5 and Table 8.3 in the Appendix, Section 8.3.1. As can be seen in Figure 5.5, the ionic conductivity improves as the temperature increases. This can be understood by taking into account the effect of the temperature on the viscosity of the IL, which decreases as the temperature rises. The introduction of SiO<sub>2</sub> NPs within the polymer matrix substantially improves the ionic conductivity of the P*SiCIL* membrane. In particular, the room temperature conductivity increases from 0.51 mS cm<sup>-1</sup> for the pure polymer to 1.04, 1.22 and 0.71 mS cm<sup>-1</sup> with 5, 10, and 15% of SiO<sub>2</sub>, respectively. The same trend is observed in the entire temperature range, where the membrane containing 10% of SiO<sub>2</sub> NPs shows the highest values of ionic conductivity reaching 1.77, 2.51, 2.95 and 3.23 mS cm<sup>-1</sup> at 40, 55, 70 and 80 °C, respectively (the conductivity data for the other samples are summarized in Table 8.3 in the Appendix, Section 8.3.1). Interestingly, it is observed that the increase in conductivity is not a linear function of the SiO<sub>2</sub> content. The conductivity values corresponding to the SiO<sub>2</sub> content of 15% are lower than those at a SiO<sub>2</sub> content of 5 and 10%. This behavior has been previously observed in the literature and attributed to the fact that at low filler concentrations the interaction between polymer matrix and SiO<sub>2</sub> NPs facilitates the transport of Li<sup>+</sup> ions. However, when the SiO<sub>2</sub> concentration reaches a certain level, the

dilution effect predominates and the ionic conductivity decreases. [143, 182] As reported by Stephan *et al.* [143], the highest conductivity is reached when the filler content ranges from 8 to 10 wt.%. The values of the ionic conductivity obtained in this work are in line with those previously reported in the literature for polymer/IL separators. [124, 174]

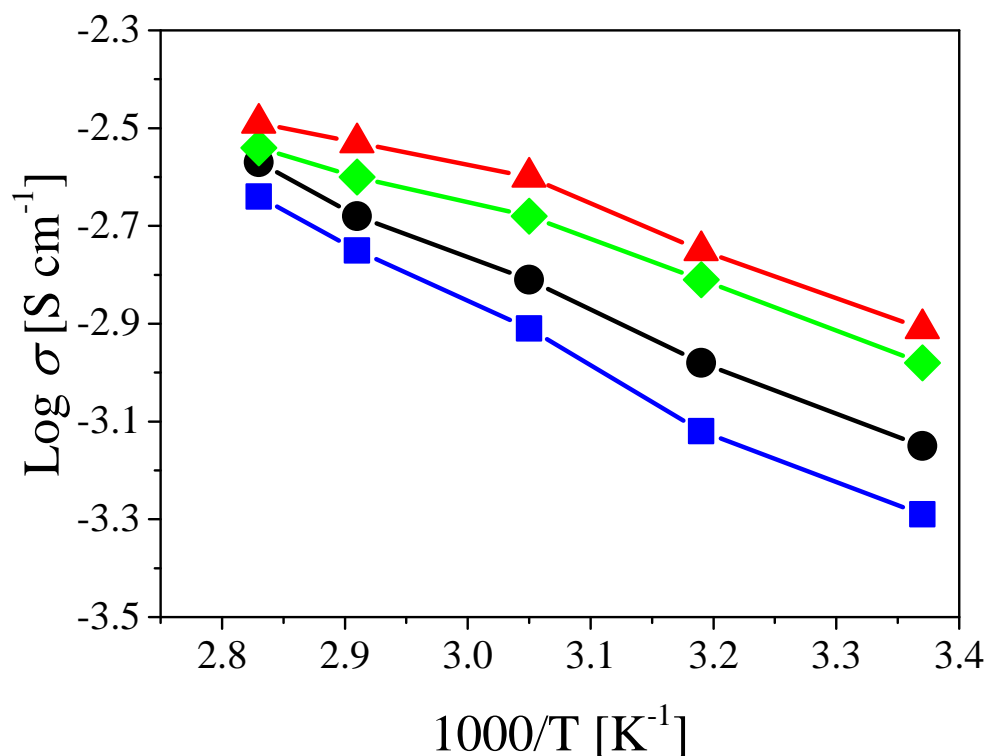


Figure 5.5: Ionic conductivity at 25, 40, 55, 70 and 80 °C of the PSiCIL membranes containing 70 wt.% of IL and 0% (blue squares) [174], 5% (green diamonds), 10% (red triangles), and 15% (black circles) of SiO<sub>2</sub>, respectively.

The membrane with a SiO<sub>2</sub> content of 10%, showing the highest ionic conductivity, was used as separator to assemble CR2032 coin cells, with lithium iron phosphate (LFP) and lithium metal as the cathode and the counter electrode, respectively. The corresponding discharge capacity was measured as a function of

the applied current density and compared in Figure 5.6 with the values obtained using the membrane made of the PVdF-HFP/IL composite without silica. [174] It is seen that the discharge capacities of the two membranes are almost identical up to a current density of 1C, with a capacity retention higher than 90% with respect to the initial cycles at 0.1C. This very low dependence of the discharge capacity on the applied current density is not common when considering earlier literature results. [171, 181] At a current density of 2C, a clear difference between the two membranes is observed, where the normalized discharge capacity is 79.5% and 83.3% for the separators with 0% and 10% of SiO<sub>2</sub>, respectively. Such a superior high capacity retention can be attributed to the fractal structure of the polymer clusters and to the bicontinuous morphology of the separator. Indeed, the high and well-controlled porosity formed *via* shear-gelation is preserved during the hot-pressing phase, where the IL solution fully impregnates the pores forming a multitude of channels through which the ions can flow, thus showing limited loss of capacity at high current density. On the other hand, the positive contribution of the silica NPs can be attributed to two factors. Firstly, the silica NPs might hinder the reorganization, even if already limited, of the polymer particles during the membrane formation process, thus leaving more channels open to the ions transfer. Secondly, as discussed in the previous paragraph, the performance at high C-rates are improved because of the same silica/polymer interactions which favor the ionic conductivity. At low current densities this is not observed as the existing channels, given the fractal geometry of the polymer clusters, are well-developed and the ion transfer is not limited by them. It is worth mentioning that, after the cycles at 2C, the battery is tested again at 0.2C showing a recovery for the membranes containing 0% and 10% of SiO<sub>2</sub> of 97.5% and 99%, respectively, thus showing limited performance loss during the cycles at high current densities. The cycle efficiency remained close to unity during all cycles.

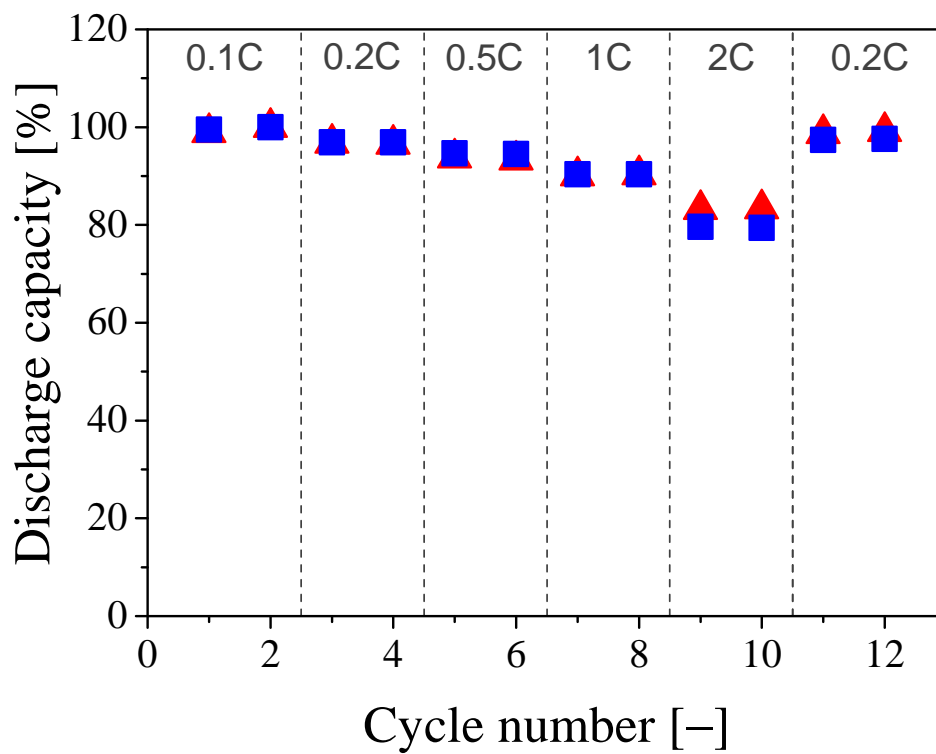


Figure 5.6: Discharge capacity, normalized with respect to the initial cycle at 0.1C, at 60 °C of the PSiCIL membranes containing 70 wt.% of IL with 0% (blue squares) and 10% (red triangles) of SiO<sub>2</sub>, respectively.

## 5.4 Conclusion

In this work, we have analysed the effect of dispersing silica NPs into PVdF-HFP/IL membranes on the ionic conductivity and discharge capacity of lithium-ion batteries. In particular, starting from the corresponding powder, we have formed a stable water dispersion of silica NPs, which could be mixed with a PVdF-HFP NP dispersion, to form a binary dispersion which was then subjected to intense shear-driven gelation. As the gelation occurs extremely fast, the silica NPs cannot escape during the gel network formation and remain entrapped and dispersed into the polymer matrix at the nanoscale level. The introduction of silica NPs into the polymer matrix was shown *via* DSC and XRD to reduce the crystallinity of the polymer, thus stabilizing the amorphous structure and facilitating the transport of Li<sup>+</sup> ions.

The so produced PVdF-HFP-SiO<sub>2</sub> composite clusters (PSiCs) were mixed with an IL solution and hot-pressed to form a membrane, so as to analyze the effect of the silica NPs on its electrochemical performance. It was observed that the ionic conductivity increases as the SiO<sub>2</sub> content increases. The ionic conductivity reaches a maximum at a SiO<sub>2</sub> content of 10%, being 1.22 mS cm<sup>-1</sup> at room temperature, and then decreases as the SiO<sub>2</sub> content further increases. The membrane formed with 10% SiO<sub>2</sub> was used to assemble coin cells and tested for cyclability at different C-rates at 60 °C. At low current densities, no significant differences between the membranes with 0% and 10% silica were observed and the measured discharge capacities at 1C were higher than 90% of the ones measured at 0.1C, showing excellent capacity retention even at high current densities. At 2C the membrane containing 10% silica performed better, showing a discharge capacity of 83.3%, compared to 79.5% of the membrane containing no silica. This can be attributed to the positive effect of the dispersed SiO<sub>2</sub> NPs, which, on one side, hinder the reorganization of the polymer NPs, thus reducing the crystallinity and

#### 5.4. CONCLUSION

---

increasing the amorphous phase, and, on the other side, favor the transfer of ions, because of their interaction with the polymer matrix.





## Chapter 6

# Core-Shell Morphology of Redispersible Powders in Polymer-Cement Waterproof Mortars

---

This chapter is based on the following publication: S. Caimi, E. Timmerer, M. Banfi, G. Storti, M. Morbidelli, Core-Shell Morphology of Redispersible Powders in Polymer-Cement Waterproof Mortars, *Polymers*, **2018**, 10(10), 1122, DOI: 10.3390/polym10101122.

## 6.1 Introduction

Cement-based materials are the most widely used components in construction industry, thanks to their setting and hardening properties. To improve their tensile strength, water impermeability and chemical resistance, various additives are normally used. [32, 183, 184] In particular, the addition of polymers is known to improve the workability of fresh mortars, the deformability, the adhesive performance, the cracks and the freezing-thawing resistances of hardened mortars. [32, 33, 185–190] Due to these advantages, polymer-cement mortars (PCMs) are commonly used in a wide variety of applications, including floor screeds, decorative finishing, tile adhesives and waterproofing systems. [187] The latter, in particular, is of large interest for the construction industry, as the PCMs provide a cheap and green alternative to other waterproofing methods, like for example bituminous sheet-based systems, which arrive at the construction site as rolls and are then laid on the surface, thus requiring substantial work as the resulting joints need to be carefully sealed as they are potential weak spots. On the other hand, PCMs can be easily applied using a trowel, roller, spray or a brush and are therefore joint-free. In addition, their thickness can be varied by the user and is not predetermined by the manufacturer, thus widening the possible application range. PCMs for waterproofing can be divided into two categories, one-component (1C) and two-component systems (2C). The latter comes as a liquid component (containing mainly the latex dispersion) which needs to be mixed with a second dry-mix component (containing sand, cement, and other ingredients) in the right ratio and then to be applied on the supporting structure. These systems, however, are susceptible to human errors during mixing and transport to the construction site is expensive. 1C systems, on the other hand, come as dry-mix mortars (consisting of sand, cement, redispersible polymer powder (RPPs), and other ingredients), which

only needs to be mixed with water on-site. The 1C solution reduces transportation and packing costs and increases the products shelf life. [191, 192] A limitation to this approach comes from the redispersibility of the polymer powder, which is not straightforward particularly in the case of relatively soft polymers such as those used for these applications.

To prepare RPPs, techniques like spray and freeze drying are commonly used. Both methods exploit the evaporation of water or sublimation of ice under specific conditions of temperature and pressure. Freeze drying is normally used to produce high-value products, as its operation is relatively complex and costly. [193] Spray drying, on the other hand, is 30-50 times cheaper and can handle various feedstocks like emulsions, slurries and solutions, which makes it the method of choice for drying polymer dispersions to produce RPPs. [194–197]

In a typical spray drying process, the latex dispersion is first atomized through a nozzle and then sprayed into the hot drying chamber where the water is quickly evaporated. Within the drying tower, a constant airflow keeps the particles in the chamber to prevent them from reaching the outlet before being fully dried. When the particles leave the chamber, a cyclone separates the exhaust gas and the dried particles are collected. The outcome of a spray drying process is influenced by several variables, such as its design, the inlet and outlet temperatures, the feed rate, the air flow and the atomization step (*i.e.*, nozzle type and atomizing speed). [198, 199] As the drying process occurs at high temperatures, the polymer particles may coalesce and agglomerate, which obviously lowers their ability to be reversibly dispersed. To prevent this, water-soluble polymers (*e.g.*, poly(vinyl alcohol), PVA) can be added as protective colloids and, in addition, anti-blocking agents, such as silicon dioxide or stearic acid, are normally added to avoid caking during storage. [195, 200–205] It is worth noting that, as there are increasing concerns about volatile organic compounds (VOCs) in building ma-

materials, the production of RPPs from water-based polymer dispersions and the spray drying step guarantee the absence of organic solvents and other organic additives. [191, 192, 206, 207]

In this work, a systematic study of the most convenient morphology of the polymer particles used in the RPPs with respect to the spray-ability, film forming characteristics and crack-bridging properties is reported. In these applications, polymers with glass transition temperature ( $T_g$ ) lower than  $-20\text{ }^\circ\text{C}$  are used. Since it would not be possible to spray dry a polymer with such a low  $T_g$ , a harder shell is grown around the soft core to limit particles coalescence and form RPPs. Indeed, core-shell morphologies were intensively studied in the literature and found application in various research areas, including limitation of the particles interpenetration upon drying, controlled release of encapsulated active ingredients, and tuning of the liquid-liquid interfaces. [208–213] In particular, for the preparation of RPPs, the core-shell morphology can improve the polymer spray-ability and its redispersion, without affecting the film forming and crack-bridging properties and without further addition of expensive additives. [56, 204, 214, 215] In general, styrene and 2-ethylhexyl acrylate can be taken as hard ( $T_g = 100\text{ }^\circ\text{C}$ ) and soft ( $T_g = -50\text{ }^\circ\text{C}$ ) monomers, respectively, while their ratio is selected so to match the desired  $T_g$ . In order to carefully control the copolymer composition and therefore the value of  $T_g$ , semi-batch emulsion polymerization was adopted [31, 216] using a reactive emulsifier (surfmer, MAPTAC) as stabilizer.

## 6.2 Experimental

### 6.2.1 Materials

Styrene (STY, 99.5% stab. with 10-15 ppm 4-*t*-butylcatechol, from ABCR) and 2-ethylhexyl acrylate (2-EHA, 98%, from ABCR) were selected as monomers, 2,2'-Azobis(2-methylpropionamidine)dihydrochloride as initiator (V-50, 98%, from Acros Organics), and [3-(Methacryloylamino)propyl]trimethylammonium chloride solution (MAPTAC, 50 wt.% in H<sub>2</sub>O, from Sigma-Aldrich) as surfactant or surmer due to the presence of an unsaturated bond. All materials were used without further purification. Deoxygenated Millipore water (Merck Millipore Synergy) provided the reaction medium for all syntheses. For spray drying fumed silica, dolomite and poly(vinyl alcohol) (PVA, Höppler viscosity 4 mPa·s, hydrolysis degree 88 mol%) were used as received. Chloroform-*d* (99.8 atom%D, stab. with Ag, from Armar Isotopes) was used as received for NMR characterization. For cement compatibility and crack-bridging tests, Portland cement (CEMI 52.5N Milke classic, from Milke) and quartz sand (0.1 - 0.3 mm) were used as provided by the supplier.

### 6.2.2 Syntheses

All semi-batch emulsion polymerizations were carried out in a 1 L glass-jacketed reactor (Syrris Atlas automated reaction system) fitted with a reflux condenser, sampling device, N<sub>2</sub> inlet, two feeding inlets and a PTFE anchor stirrer equipped with two blade impellers rotating at 200 rpm. For the polymerization, the reactor was charged with a solution of the surfactant MAPTAC (IC) in deoxygenized water (bubbled overnight with N<sub>2</sub>) and heated up to 80 °C using the heating jacket and

an oil bath (Huber, Polystat CC 302). After reaching the reaction temperature ( $\pm 0.5$  °C), part of the initiator solution (IS) was added into the reactor as a shot. The remaining initiator solution (IF) and monomer core mixture (CF) were then fed using two pumps (Bischoff, HPLC compact pump). The initiator was fed for 6 hours, while the core monomer mixture was fed for 2.5 to 3.5 hours depending on the core-shell ratio used. After switching off the core feed, it was waited for 1 to 1.5 hours (WT) until the conversion reached approximately 80%. The monomer shell mixture (SF) was then fed for 0.5 to 1.5 hours, in order to have a total monomer feed time of 4 h. After switching off the initiator feed, the reaction was stirred for an additional hour to ensure full conversion. The detailed reaction formulations are summarized in the discussion section and in Tables 8.4 and 8.5 in the Appendix, Section 8.4.1.

### 6.2.3 Characterization of polymer dispersions

A sample was taken from the polymerization reactor every hour to monitor instantaneous conversion, particle size and composition. By measuring the solid content with a HG53 Halogen Moisture Analyzer (Mettler-Toledo) the instantaneous conversion could be calculated. The average radius of the polymer NPs and the polydispersity index (PDI) are measured by dynamic light scattering using Zetasizer Nano ZS 3600 (Malvern Instruments) after diluting the sample with deionized water. To analyze the instantaneous composition of the copolymer, the samples were dried in a vacuum oven at 50 °C and dissolved in deuterated chloroform to perform  $^1\text{H-NMR}$  measurements using a 300 MHz Spectrometer (Bruker). By calculating the peak integrals from the spectra, it was possible to estimate mole and mass fractions of 2-EHA in each sample. As an example, the spectra for monomers and copolymer are reported in the Appendix in Figure 8.8 for sample *a*.

The zeta potential of a 0.01 wt.% solution of the final latex was measured using the Zetasizer Nano ZS 3600 and the pH was measured using a SevenEasy pH-meter (Mettler-Toledo).

To determine the glass transition temperature ( $T_g$ ) of the produced copolymer, differential scanning calorimetry was performed in a Q1000 Differential Scanning Calorimeter (TA Instruments) using 10 mg of sample in 40  $\mu$ L aluminum crucibles, heating and cooling rates of 5  $^{\circ}$ C  $\text{min}^{-1}$  in nitrogen atmosphere, and temperature range from -80 to +100  $^{\circ}$ C. The  $T_g$  was obtained from the DSC plot (heat flow *versus* temperature) using the inflection point of the S-shape profile, as described in the literature. [217] Finally, to evaluate the film-forming ability, a few droplets of the polymer latex were transferred into a petri dish and dried in air at room temperature.

#### 6.2.4 Spray drying

For spray drying in a NiroAtomizer (Niro), a water solution of 25 wt.% PVA was prepared and added to the copolymer dispersion to have 15% of PVA with respect to the polymer. Then, the dispersion was diluted with water to have a total solid content of 25%. The inlet temperature of the spray drier was set at 135  $^{\circ}$ C and the outlet temperature was kept at approximately 70  $^{\circ}$ C. A peristaltic pump (ISM 817, IKA) was used to feed the dispersion at 12.2  $\text{g min}^{-1}$ . To prevent caking of the dried powder, silica was fed together with limestone powder with a ratio of 1:18 through a dry powder feeder (AccuRate) with a feed rate of 0.75  $\text{g min}^{-1}$  to have 19 wt.% with respect to the polymer. The compressed air inlet to disperse the anti-caking mixture was set at 2 bar and the spray nozzle was set at 3.5 bar. The amount of collected powder was weighed to measure the yield and 0.5 g of it were mixed with 10 mL of water to test redispersibility.

### 6.2.5 Polymer-cement mortars

To test the quality of the cement-based mortars prepared using the different copolymers, 25 g of dried polymer were dry-mixed with 56 g of quartz sand and 19 g of Portland cement. The dry-mix was poured into approximately 20 g of water and a timer was started. It was then stirred vigorously for 1 minute and the wetting speed as well as the fluidity were analyzed. If the amount of water was not sufficient to yield a creamy consistency, additional water was used. The polymer-cement mixture was then applied on top of two adjacent cement fiber plates with a thickness of 2 mm. 5 hours later, a second layer of 2 mm polymer-cement membrane was applied. The membrane was left at rest for 28 days at standard conditions (23 °C/50% relative humidity) before the crack-bridging test.

The mortar and sample preparation procedure is sketched in Figure 8.6 in the Appendix, Section 8.4.3

### 6.2.6 Crack-bridging ability of the polymer-cement mortar

Crack-bridging tests were performed according to EN 14891 [218] in the temperature range from -20 to 23 °C using a Z020/TH2S (Zwick/Roell) to measure the maximum expansion until visible cracks form. The displacement rate is 0.15 mm min<sup>-1</sup> and is kept constant during the test. Before the test and the recording starts, a pre-load of 20N was applied. To be able to vary the testing temperature, the whole straining device was encased by a temperature-controlling unit (TEE 65/40X, RS-Simulatoren).



## 6.3 Results and Discussion

### 6.3.1 Synthesis of core-shell polymer nanoparticles

Core-shell polymer nanoparticles with the different morphologies sketched in Figure 6.1 were prepared in order to investigate the effect of core-shell ratio, shell thickness, and shell hardness on the ability to be spray dried and to form crack-resistant membranes. The core is made of 25/75 wt.% of STY/2-EHA, respectively, having a  $T_g$  of approximately  $-25\text{ }^\circ\text{C}$  and with a size ranging from 255 to 285 nm, as reported in Table 6.1. Being the core nanoparticles extremely soft (*i.e.*, with very low  $T_g$ ), a dispersion of this product could not be spray dried as it led to fully coalesced particles which could not be redispersed. To improve the spray-ability, a harder shell with  $T_g$  higher than  $65\text{ }^\circ\text{C}$  was grown around the soft core.

The different types of particle morphologies described in Table 6.1 were prepared. On one hand, the shell thickness was varied from 5 to 15 nm while keeping the core size constant at approximately 280 nm (latexes *a*, *d* and *e*). On the other hand, the final particle size was kept constant at approximately 300 nm and the core-shell ratio was varied from 87% to 97% (latexes *a*, *f* and *g*). Moreover, to study the influence of the hardness of the shell, its composition was varied from 80% to 99% STY content, while keeping the core size and shell thickness constant at 280 and 300 nm (latexes *a*, *b* and *c*) and at 260 and 295 nm (latexes *g*, *h* and *i*), respectively. Finally, for comparison purposes, a latex made of core-only particles (*i.e.*, with an overall composition of 25/75 wt.% of STY/2-EHA) was considered (latex *j*).

The values of final particle size and PDI (polydispersity index by DLS) for all particles are reported in Table 6.1. Small PDI values (below 0.1) indicate narrow particle size distribution, meaning that almost all particles have the same size. As above-mentioned, particle size, instantaneous conversion and copolymer

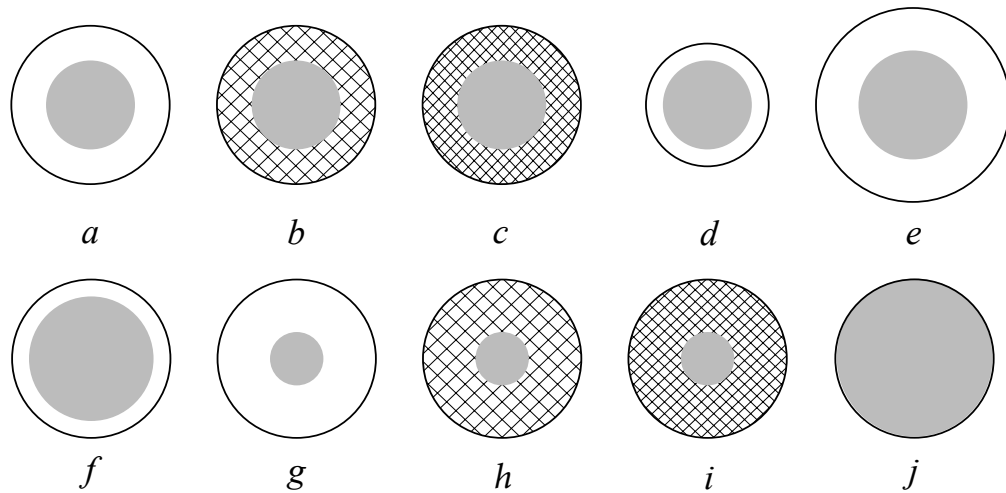


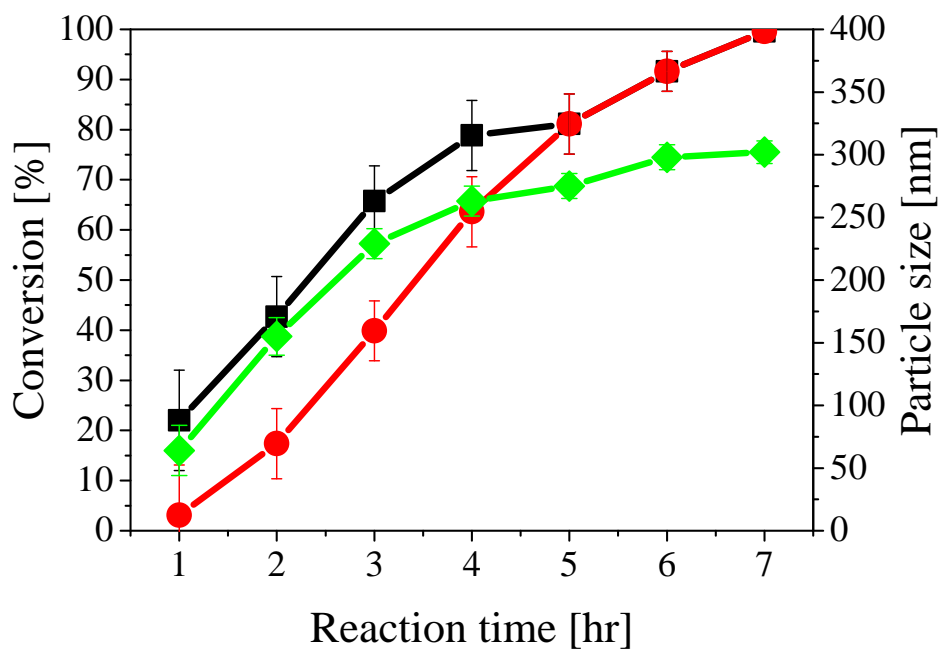
**Figure 6.1:** Morphologies of the different synthesized core-shell polymer nanoparticles. Medium core size with medium shell thickness and styrene content of (a) 80%, (b) 90%, and (c) 99% in the shell. Medium core size with a (d) thinner and (e) thicker shell of styrene content of 80% and different overall particle size. Different core size while keeping the overall size constant with respect to (a), leading to a (f) thinner and (g) thicker shell of styrene content of 80%. Same morphology as (g) but with a styrene content of (h) 90% and (i) 99% in the shell. (j) Core-only latex particles.

composition were monitored during all reactions. With illustrative purposes, the time evolutions of instantaneous and cumulative conversions, and average particle size in the case of reaction *a* are shown in Figure 6.2. These curves had similar shape for all other reactions and, in particular, it is possible to note that both particle size and conversion values show a rapid increase at the beginning, while slowing down after about 4 hours of reaction time due to the progressive monomer depletion. The initial lag time before the reaction starts is due to the presence of inhibitors in the monomers along with the lower reactivity of 2-EHA with respect to STY. On the other hand, the instantaneous conversion (defined with respect to the amount of monomers added to the reactor until the given time) reaches a value of approximately 70% after 3 hours and remains larger for the rest of the reaction. The cumulative conversion (defined with respect to the entire amount of monomers added into the reactor) grows following the typical S-shape and reaches 100% after 7 hours. The two curves obviously superimpose after 5 hours when the monomer mixture addition was completed. The average particle size increases up to 300 nm (green curve in Figure 6.2) and the PDI value was measured to be below 0.1 throughout the whole reaction. The total number of polymer particles remained constant at approximately  $1.5 \cdot 10^{16}$ , indicating no secondary nucleation as reported in Figure 8.5 in the Appendix, Section 8.4.1.

The values of the cumulative composition of sample *a* during the reaction are shown in Figure 6.3. As reported in Table 8.4, the core mixture (CF) made of STY/2-EHA 25/75 wt.% was fed during the first 3 hours of the reaction, followed by 1 hour rest (WT) and subsequent feed of the shell mixture (SF) (STY/2-EHA 80/20 wt.%) for 1 hour. This feed policy is consistent with the composition profile in the figure, which is approximately equal to 75% 2-EHA for the first 4 hours and then decreases progressively to the value of 65% 2-EHA, which is the expected final cumulative composition assuming complete conversion (dashed curve in Fig-

**Table 6.1: Final size, PDI (polydispersity index) and glass transition temperature ( $T_g$ ) of the different polymer particles.**

Sample	<i>a</i>	<i>b</i>	<i>c</i>	<i>d</i>	<i>e</i>	<i>f</i>	<i>g</i>	<i>h</i>	<i>i</i>	<i>j</i>
Core size [nm]	280	278	284	276	279	285	255	258	260	296
NPs size [nm]	302	296	301	286	311	294	293	294	303	
PDI	0.01	0.03	0.02	0.06	0.04	0.02	0.07	0.06	0.01	0.02
Core $T_g$ [°C]	-24.0	-27.6	-24.2	-25.6	-25.0	-24.4	-21.5	-25.2	-22.7	-24.7
Shell $T_g$ [°C]	65.8	74.2	86.7	65.8	65.8	65.8	65.8	74.2	86.7	


**Figure 6.2: Instantaneous (black squares) and cumulative (red circles) conversion, and average particle size (green diamonds) during the synthesis of sample *a*.**

ure 6.3). These results show no preferential incorporation of the two monomers, with the formed polymer chains having the desired cumulative composition. This is confirmed for all polymer samples as reported in the Appendix, Table 8.7.

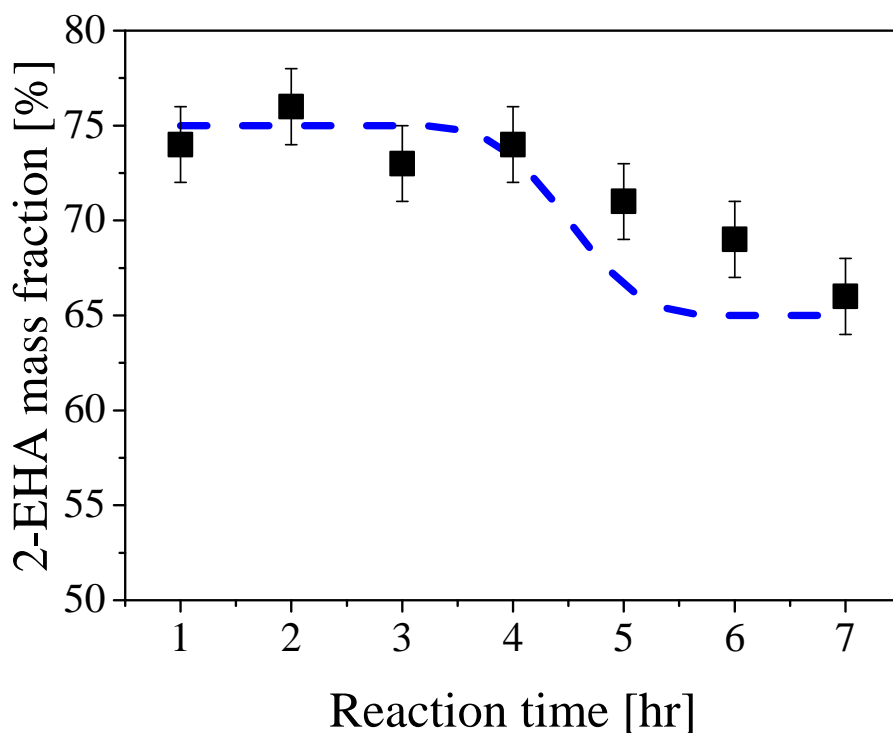


**Figure 6.3:** Mass fraction of 2-EHA in the polymer particles for sample *a* during the reaction. The dashed curve represents the cumulative polymer composition corresponding to the fed monomer mixture assuming complete conversion.

The  $T_g$  values of the different copolymers measured by DSC are also shown in Table 6.1. Approximately  $-25\text{ }^\circ\text{C}$  was estimated in all cases, which is in agreement with the estimated value for a copolymer with composition STY/2-EHA 25/75 wt.% using the Fox equation: [219, 220]

$$\frac{1}{T_g} = \frac{\omega_1}{T_{g,1}} + \frac{\omega_2}{T_{g,2}} + \dots + \frac{\omega_n}{T_{g,n}} \quad (6.1)$$

where  $\omega_k$  and  $T_{g,k}$  are the weight ratio and the glass transition temperature of the generic monomer  $k$ , respectively. This property needs to be closely controlled in the application considered in this work since the polymer  $T_g$  is known to affect film formation, film shape and cement hydration in mortars. [221] Note that the reported  $T_g$  values refer to the core only, as it was not possible to observe the characteristic S-shape at higher temperatures corresponding to the shell composition, because the core-shell transition is quite smooth and, therefore, there is a very gradual change in the composition towards the harder shell. This is illustrated, for the case of polymer  $a$ , in Figure 6.4 where the heating and cooling profiles are shown. It is seen that only the  $T_g$  value of the particle core can be estimated from the S-shaped profile of the heating curve (black curve). The shell  $T_g$  values of the different samples reported in Table 6.1 were measured by synthesizing particles with homogeneous morphology and the same composition as the shell, that is STY/2-EHA equal to 80/20, 90/10 and 99/1 wt.%, which resulted to be 65.8, 74.2, 86.7 °C, respectively.

Finally, to quantify the surface charge of the polymer particles, which allows inferring the stability of the corresponding polymer latexes, the zeta potential values were measured. As the surfactant used in the polymerization bears a positive charge at neutral pH, all measured values of zeta potential are positive and lie between 47.4 and 54.5 mV (Table 8.6 in the Appendix, Section 8.4.2). These electrostatic repulsion forces result in stable dispersion along with good spray-ability during the drying step. Moreover, all latexes were dried into petri dishes to verify their film formation ability. In all cases, the presence of the harder shell does not hinder the film formation upon drying, as reported in Table 8.6. The used surfmer MAPTAC combines in its molecular structure a charged, positive group, which gives stability to the system, and a polymerizable unsaturated bond, which can react with the monomers and be incorporated into the growing polymer chains. [222]

Being covalently attached to the particles, it will not desorb during film formation and therefore the properties of the RPPs remain unchanged. [223–225] Indeed, conventional surfactant due to their possibility of migrating from the particle surface to the liquid solution are known to negatively affect the final properties of the materials, such as the adhesion strength, the water resistance and the crack-bridging properties. [226, 227]

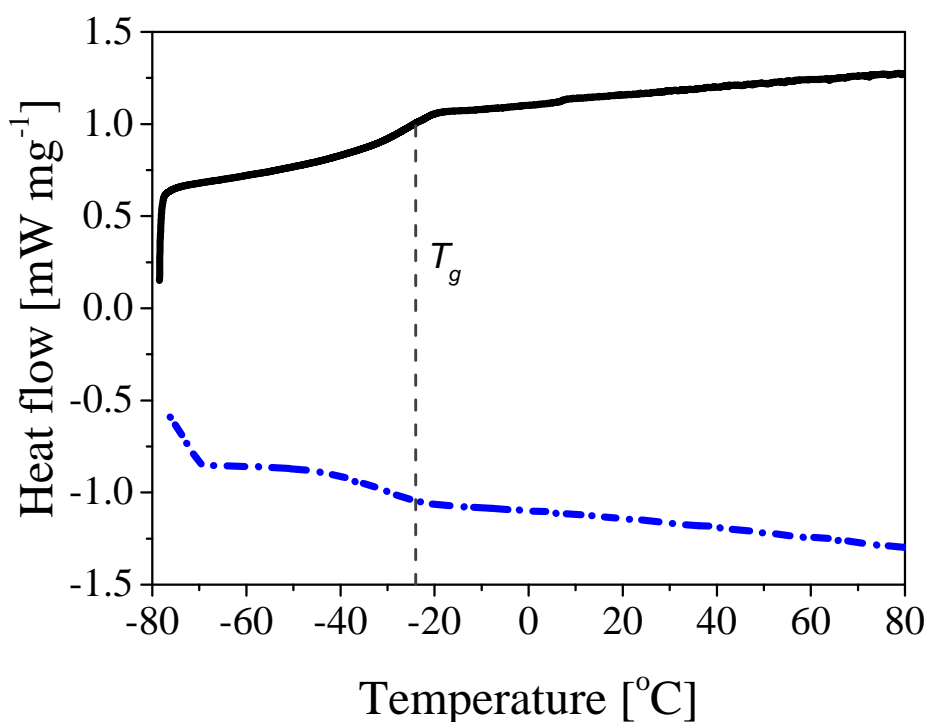


Figure 6.4: DSC curves of polymer *a*: heating (solid black) and cooling (dashed blue) heat flow profiles.

### 6.3.2 Spray drying and redispersibility

All the latexes were spray dried according to the procedure described in the experimental section. The qualitative values of the size of the obtained powder grains estimated by visual inspection are reported in Table 6.2 along with their free-

flowing ability after 24 hours of storage (*i.e.*, no caking effect) and redispersibility in water.

Polymer *j*, whose particles are made of soft core only, with a  $T_g$  of approximately -25 °C, could not be spray dried: the powder stuck to the internal wall of the tower and no dried product could be collected at the unit outlet. However all latexes with core-shell polymer particles could be effectively spray dried. In particular, the samples with low core-shell ratio and thick shell (*i.e.*, latexes *e*, *g*, *h* and *i*) showed the best performance during spray drying. Their hard shell prevented particle interpenetration after aggregation and, therefore, free-flowing, fine powders were produced. To appreciate the difference between coarse and fine powders, a picture of both - coarse powder (polymer *d*) and fine powder (polymer *i*) - is shown in Figure 6.5. Latex *d* was the only exception, since a non-free-flowing coarse powder was collected in this case. This fact can be understood by considering that this latex has the thinnest shell, probably too thin to exclude interpenetration, and the smallest particle size, both triggering film formation. On the other hand, latex *f*, having the same shell thickness as latex *d*, showed good spray-ability. This may be due to the larger overall particle size, which facilitates the spray drying: since the polymer particles exhibit lower specific surface, they are less exposed to interpenetration at constant amount of protective colloid.

From the data in Table 6.2, it is also evident that the increasing hardness of the polymer surface going from latexes *a* to *b* and *c* and from *g* to *h* and *i* did not show any visible effect on the powder quality, thus confirming that particle size and shell thickness are the most important factors limiting interpenetration. It can then be concluded that the core-shell structure improves the spray-ability while retaining film-forming properties, as confirmed by the results summarized in Table 6.2 and Table 8.6.

About the operating conditions of the spray dryer, it was observed that too



### 6.3. RESULTS AND DISCUSSION

**Table 6.2:** Results of the visual analysis of the spray dried polymer latexes. Qualitative grain sizes range from fine (*fp*) over medium (*mp*) to coarse (*cp*) powder. The samples are also classified in free-flowing (*ff*) and caking (*ca*) powders. Their redispersibility in water ranges from good (*gr*), to medium (*mr*) and to bad (*br*).

Sample	<i>a</i>	<i>b</i>	<i>c</i>	<i>d</i>	<i>e</i>	<i>f</i>	<i>g</i>	<i>h</i>	<i>i</i>
Grain size	<i>mp</i>	<i>mp</i>	<i>mp</i>	<i>cp</i>	<i>fp</i>	<i>mp</i>	<i>fp</i>	<i>fp</i>	<i>fp</i>
Free-flowing properties	<i>ff</i>	<i>ff</i>	<i>ff</i>	<i>ca</i>	<i>ff</i>	<i>ff</i>	<i>ff</i>	<i>ff</i>	<i>ff</i>
Redispersibility	<i>gr</i>	<i>mr</i>	<i>mr</i>	<i>mr</i>	<i>gr</i>	<i>gr</i>	<i>mr</i>	<i>br</i>	<i>br</i>



**Figure 6.5:** Sample *i* (left) and sample *d* (right) after spray drying.

low inlet temperatures (lower than 120 °C) resulted in insufficient drying and high residual humidity, leading to caking after 24 hours of storage. On the other hand, at too high inlet temperatures (higher than 150 °C), the polymer was too soft and the particles excessively interpenetrated, leading to too coarse powders. Concerning the amount of PVA (15 wt.%) and anti-caking agent (19 wt.%), it was observed that lower values led to coarser powders as the protective effect against interpenetration was reduced. Higher values were not investigated as they could negatively affect the crack-bridging performance of the final membrane.

As anticipated, to be properly mixed with cement and form homogeneous membranes, the spray dried polymer powders have to be well redispersible in water. Redispersibility was then analyzed as described above and the results are summarized in Table 6.2 for the different polymer powders. All samples could be easily redispersed by simple stirring and none of them formed large coagulates. However, some powders settled after resting for 24 hours, whereas others remained uniformly dispersed. The former are listed as bad redispersible (*br*) and the latter as good redispersible (*gr*) powders in Table 6.2. The results show that good spray-ability does not necessarily mean that the dried powders are well redispersible. For example, in the case of the samples shown in Figure 6.5, the coarser powder *d* is better redispersible than the finer *i*, as shown in Figure 6.6. This can be understood by taking into account the hydrophobicity of the shell: since harder shells have higher styrene contents, their more hydrophobic nature leads to more difficult wetting, which makes them difficult to be redispersed in water. This becomes evident when comparing the redispersibility of powders *a* with *b* and *c* and of the powders *g* with *h* and *i* (see Table 6.2).



Figure 6.6: Powders *i* (left) and *d* (right) redispersed after spray drying.

### 6.3.3 Crack-bridging and polymer-cement compatibility

The polymer powders *a* to *i* were used to produce 2 mm cement-based membranes by mixing the powders with quartz sand, cement and water as described in the experimental section. The membranes were tested for crack-bridging properties and the results are shown in Figure 6.7. Samples *h* and *i* could not be tested as they did not form homogeneous, crack-free membranes (see Figure 8.7 in the Appendix, Section 8.4.3). This could be imputed to the strongly hydrophobic nature of the shell of these particles which contains high amounts of STY.

The crack-bridging results showed a similar trend for all tested samples (polymers *a* to *g*). At temperatures above 20 °C the performance was poor, as the polymer is excessively soft and unable to bridge cracks in the composite material. As the temperature decreases, clear differences among the samples emerge. In the whole temperature range, samples *d* and *f* (those with thinner shell) showed the largest possible expansion of approximately 0.7 and 0.6 mm at -10 and -20 °C, respec-

tively. In comparison, polymers *e* and *g* (those with thicker shell) showed the lowest performance, reaching about 0.6 (*e*) and 0.5 mm (*g*) at -10 °C and 0.4 mm at -20 °C. This can be understood by taking into consideration that the polymer particles have to fully coalesce during drying in order to avoid cracks formation. A thicker shell does not impede film formation (cf. Table 8.6) but it increases the fraction of film with higher  $T_g$ , which does not contribute to improve the crack-bridging behavior.

Furthermore, when comparing the samples with medium shell thickness and different styrene content in the shell (polymers *a* to *c*), it is possible to see that a harder shell leads to lower performance. Indeed, the membranes prepared using samples *b* and *c* (with 90% and 99% styrene in the shell, respectively) could expand less before cracks form with respect to sample *a*, with 80% styrene in the shell. Again, harder shell makes it more difficult for the polymer particles to fully coalesce and, therefore, to form a crack-resistant film. In general, the performance of all samples decreased at low temperatures, since the polymer gets harder and more brittle as the  $T_g$  of the polymer (-25 °C) is approached.

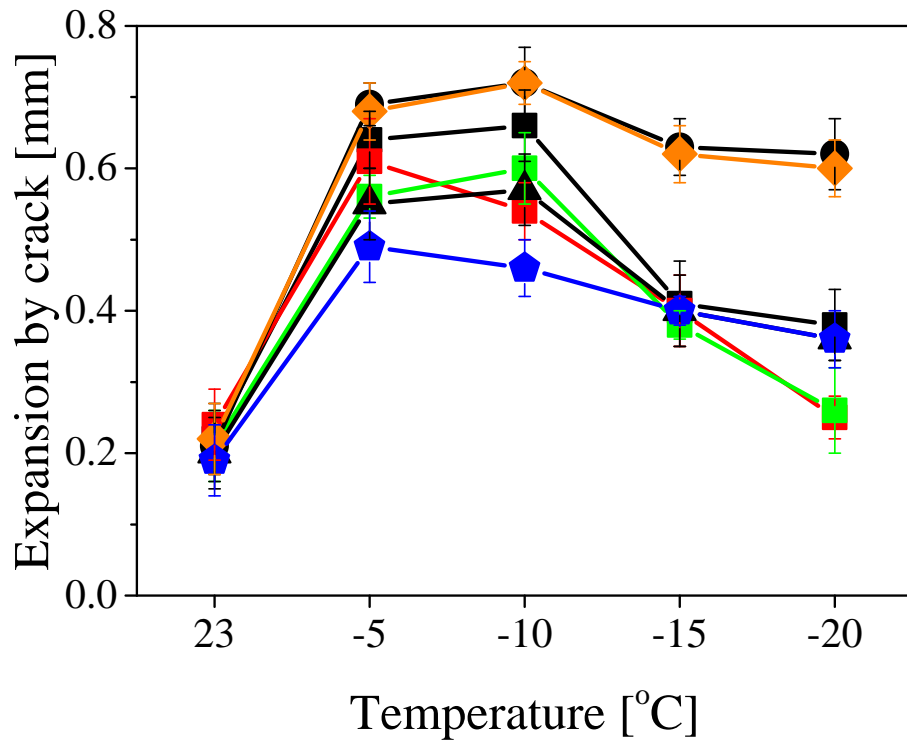


Figure 6.7: The expansion in millimeters before the membrane cracks at different temperatures for the membranes obtained with the samples *a* (black squares), *b* (red squares), *c* (green squares), *d* (black circles), *e* (black triangles), *f* (orange diamonds) and *g* (blue pentagons).

## 6.4 Conclusion

Polymer-cement mortars are widely used in the construction industry for their attractive application characteristics, particularly with respect to waterproofing. Core-shell polymer particles can be used to specifically improve the spray-ability and crack-bridging properties of the membrane obtained from these powders. In order to better understand these systems and eventually optimize the core-shell morphology, various low  $T_g$  polymer latexes made of styrene and 2-ethylhexyl acrylate were synthesized *via* semi-batch emulsion polymerization. In particular, the core-shell ratio and the shell thickness and hardness were varied systematically to analyze the system behavior. Tuning the composition of the copolymer, the core had a  $T_g$  of  $-25\text{ }^\circ\text{C}$ , whereas the shell, richer in styrene, higher than  $65\text{ }^\circ\text{C}$ . The latexes were spray dried after the addition of 15% of poly (vinyl alcohol) by weight with respect to the polymer as a protective colloid and of a mixture of 1 wt.% silica and 18 wt.% limestone powder as anti-caking agent. All obtained powders were redispersed in water and mixed with cement and quartz sand to form mortars, which were tested for crack-bridging properties at different temperatures.

It was observed that all samples with core-shell morphology could be effectively spray dried and led to redispersible polymer powders. In particular, for the system under consideration, the latexes with a particle size larger than 300 nm and a shell thicker than 10 nm exhibited the best performance during spray drying. Smaller particles and thinner shells led to more interpenetrated particles during drying and therefore formed coarser powders. Moreover, samples containing more than 80% of styrene in the shell resulted in non-uniform and non-crack-free membranes, most probably because of their excessive hydrophobic character. On the other hand, concerning the crack bridging properties, the mortars formed with the polymers having 5 nm-thick shell with 80% styrene showed best performance, as the particles could fully interpenetrate and coalesce. Therefore, the best compro-

#### 6.4. CONCLUSION

---

mise in terms of core-shell morphology for spray-ability and highest crack-bridging properties of the final mortar consists of large particles with thin shell (core-shell ratio of 97%, *i.e.*, shell thickness of a few nanometers) and styrene contents in the shell not larger than 80%, that is with limited hydrophobicity.

In conclusion, this study shows the importance of core-shell morphology in improving the performance of polymer-cement mortars, but also indicates the need for its careful design in terms of geometrical and chemical characteristics.





# Chapter 7

## Conclusions and outlook

This thesis provided an overview of some applications of composite materials based on polymers. In particular, the colloidal polymeric constituent was carefully designed in terms of composition, particle size and morphology so to have the desired properties of the final material.

In the first part of the thesis, polystyrene nanoparticles of 78 nm were synthesized as a model system to study the kinetics of shear-aggregation inside a microchannel. In particular, it was observed that, when forcing the NP dispersions to repeatedly pass through a Z-shape microchannel, the extent of aggregation of the NPs to large clusters initially increases and then reaches a plateau value that is by far smaller than unity. This result is in contrast with the typical outcome of bimolecular reactions, where the system reaches full conversion as long as the reaction time is long enough. In our experiments, the energy given to the system in the form of intense-shear is definitely large enough. However, the system does not reach full conversion, even after repeated passes through the microchannel. To explain the observations, various additional processes occurring under intense shear were considered. The erosion of particles from already existing clusters was excluded by further designed and targeted experiments, which showed that the maximum achievable conversion does not result from the equilibrium between erosion and aggregation. As a second hypothesis, it was considered that a minimum time is required for the particles to overcome the energy barrier so as to realize the shear-driven aggregation. If the residence time of the particles inside the microchannel is smaller than the minimum aggregation time, no aggregation occurs. To verify this hypothesis, two microchannels with different length but same geometry were designed so that the residence time for each pass was double. In this case, when the dispersion was processed in the longer channel, higher conversions were achieved, proving that the residence time in each pass is the key for the extent of aggregation.

---

In the third chapter of the thesis, crosslinked polystyrene microparticles of approximately  $2\ \mu\text{m}$  were synthesized, and made fluorescent by the addition of a dye, to be aggregated in shear-controlled regime and tracked by confocal microscopy to identify surface alterations and material transfer between different particles upon aggregation/breakage experiments. In particular, a mixture of fluorescently labelled and non-labelled swollen particles was destabilized by salt addition in a stirred tank and subjected to shear for 5 hours. The system was sampled and the percentage of particles showing a fluorescent signature was recorded over time. It was observed that, starting from a 1:1 mixture of fluorescent and non-fluorescent particles, upon aggregation and breakage experiments, the percentage of fluorescent particles reached after 5 hours a fraction of 70%, thus showing and proving that material exchange between the surface of swollen core-shell polymer particles could occur during processing.

Moving to the applications, a new method to form freestanding separators for lithium-ion batteries made of polymer and ionic liquid is described in the fourth chapter aimed to replace commercial materials. The latter, indeed, are made of a polyolefin membrane impregnated with an organic electrolyte which shows limited thermal stability. As in recent years, there is a constant need for higher performing batteries for large-scale applications, such as electric vehicles and smart grids, safer alternatives have to be found. One of the most studied electrolytic systems is based on the use of ionic liquids (ILs), which are characterized by low flammability, scarce volatility, and negligible toxicity. Nonetheless, the process to form freestanding IL-based separators is not straightforward, as it is often difficult to obtain thin and porous polymer matrices, which can host the IL without hindering the ionic conductivity, which is of utmost importance to achieve good performance. Our method starts from a colloidal dispersion of polymer nanoparticles of PVdF-HFP, which can be shear-aggregated in a controlled way so to

form micron-scale fractal polymer clusters (PCs) with enhanced internal porosity, higher than 80%. These PCs can be dried, ball-milled, mixed with the IL solution (Pyr13TFSI), and hot-pressed. By choosing the right operating conditions in terms of temperature and pressure, it was possible to prepare freestanding and thin membranes at increasing polymer/ionic-liquid ratio and test them for ionic conductivity and charge/discharge cyclability. It was shown that the best performance was obtained with a polymer/ionic-liquid ratio of 30/70 wt.%, when the assembled battery showed excellent results not only at low but also at high current density, showing a capacity retention higher than 88% at 2C and a cycle stability for more than 200 cycles. This result could be achieved thanks to the complete interconnection of the pores in the membrane, typical of fractal structures, which guarantees fast and uniform transfer of ions through the separator. Moreover, the developed design methodology is very versatile and could be easily applied to systems with different ILs to study the performance of the PCIL membranes at low and high temperatures.

As reported in the literature, the addition in the separator of inorganic nanoparticles, such as  $\text{SiO}_2$ ,  $\text{Al}_2\text{O}_3$ ,  $\text{TiO}_2$ , and  $\text{CeO}_2$ , can promote the ionic conductivity and improve the overall performance of the battery. However, to ensure a positive effect and maximize their contribution, these fillers have to be dispersed in the polymer matrix uniformly and at the nanoscale level, which is obviously not straightforward. Based on this methodology and having understood the concept of binary aggregation, a procedure suitable to form polymer/silica composite clusters which can be used for ionic-liquid-based separators is discussed in the fifth chapter. In particular, starting from a powder, an aqueous NP dispersion of silica is prepared and mixed with the PVdF-HFP dispersion. This binary system is then subjected to shear-driven aggregation by passing through a microchannel where the polymer NPs undergo gelation in few milliseconds, entrapping the silica nanoparticles. As

---

the process occurs in a very short time, the filler remains dispersed uniformly in the polymer clusters. Using the same procedure described above, separators based on silica, polymer, and ionic liquid are prepared at increasing amount of silica to investigate the effect of the filler on the performance of the battery assembled with these membranes. The presence of silica into the separator was shown to reduce the crystallinity of the polymer, thus stabilizing its amorphous structure and facilitating the transport of ions. As expected, the ionic conductivity reached a maximum at a SiO<sub>2</sub> content of 10%, being 1.22 mS cm<sup>-1</sup> at room temperature, compared to 0.51 mS cm<sup>-1</sup> of the pure polymer. Again, this method is very versatile and other fillers than silica could be used, provided that they can be dispersed in water at nanoscale level and they bear a negative charge so to be mixed with the polymer without inducing aggregation. Moreover, this technique to uniformly disperse a filler in a polymer matrix can have applications in different fields, such as catalysis, drugs encapsulation and delivery, *etc.*

The last part of the thesis is focused on the synthesis of a composite material for the construction industry. In particular, a soft polymer to be mixed with concrete so to form crack-resistant waterproofing cement-based membranes had to be developed. Indeed, the addition of polymers is known to improve the properties of polymer-cement mortars (PCMs), widening the range of possible applications, including floor screeds, decorative finishing, *etc.* Furthermore, in recent years, to save costs in transportation, packaging and storage, there is an increasing tendency to produce the so-called one-component systems, which consist of a dry mixture of redispersible polymer powder (RPP), cement, sand and further additives, to which only water has to be added on the construction site. On the other hand, it is not straightforward to produce RPPs of very soft polymers due to their tendency to coalesce upon drying. To avoid this, the polymer particles can be covered by a harder shell which can limit their interpenetration. Unfortunately,

the harder shell has a negative influence on the crack-bridging performance of the final material. Therefore, the optimal morphology of the polymer particles which simultaneously guarantees formation of a non-sticky powder during spray drying, good redispersibility, and enhanced crack-bridging properties of the final composite has to be identified. In this part of the thesis, the systematic study on the optimal core-shell ratio, shell thickness and surface chemical composition (hardness) of the polymer particles is therefore presented. The best geometry consisted of large particles with thin shell (core-shell ratio of 97% and a shell thickness of a few nanometers) and a styrene content in the shell not larger than 80% to limit surface hydrophobicity.

# Chapter 8

# Appendix

## 8.1 Aggregation of Stable Colloidal Dispersions under Short High-Shear Conditions

### 8.1.1 Synthesis and characterization of the polystyrene nanoparticles

Polystyrene (PS) nanoparticles (NPs) were selected in this work, and synthesized *via* emulsion polymerization in water at 70 °C using SDS (Sigma-Aldrich) and KPS (Merck) as surfactant and initiator, respectively. The average radius of the PS NPs was determined by dynamic light scattering (NanoSizer, Malvern, UK) to be  $a = 39$  nm. Before measurement, the surfactant in the colloidal system was removed by washing with hydrogen and hydroxide resins (Dowex Marathon MR-3, Sigma-Aldrich).

### 8.1.2 Manufacturing of the quartz microchannels

The microfluidic systems were fabricated from borosilicate glass (Schott BOROFLOAT® 33), which are available as 700  $\mu\text{m}$  thick wafers. A femtosecond laser (microSTRUCT c, 3D Micromac AG) was used to structure the microfluidic channels by ablation, as described in Erfle *et al.* [52] Using the same laser parameters and scanning strategy, it resulted in a channel depth of 107  $\mu\text{m}$ . The cross section of the channel shows rounded corners and channel sidewalls at an angle of 64° (Figure 8.1). Directly after laser ablation, the sidewalls and the bottom of the microchannels as well as the vicinity are covered with glass particles and filaments. To remove the particles, the substrate is immersed in a glass etching solution (phosphoric acid, hydrofluoric acid and water, mixed 20:6:9) for 90 s. After etching, the glass surfaces in the microchannels exhibit a roughness of  $Ra = 0.43$   $\mu\text{m}$  (VK-X260K, Keyence). The surface is characterized by round pits, which have



a diameter of up to 4  $\mu\text{m}$  (Figure 8.2). The open channels on the wafer were closed with a second structured wafer with a mirrored design and thermally tempered at 630  $^{\circ}\text{C}$  for six hours.

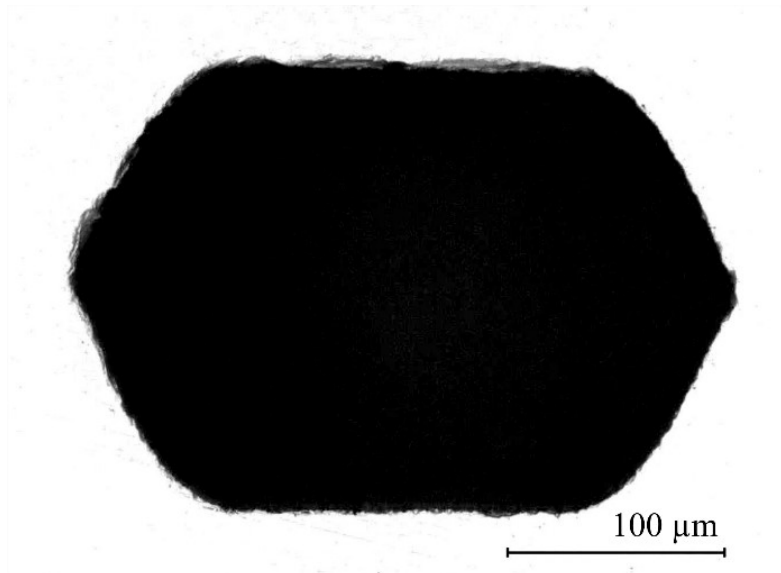


**Figure 8.1:** Microscopic image of the cross section of the closed microfluidic channel after thermal bonding of two structured wafers.

### 8.1.3 Measurement of degree of aggregation and morphology of clusters

The degree of aggregation can be determined by the conversion ( $\chi$ ) of the NPs to large clusters. As previously observed, two populations of clusters are observed when the NP dispersion is forced to pass through the MC under intense shear. The first one is composed of the NPs plus small amount of small clusters (*i.e.*, doublets and triplets), whereas the second population corresponds to large clusters, with an average diameter of at least 2 orders of magnitude larger than that of small clusters. Suitable centrifugal speed and time can be selected to separate the two populations, thus to determine the  $\chi$  value. Typically, 20 mL of sample were collected using

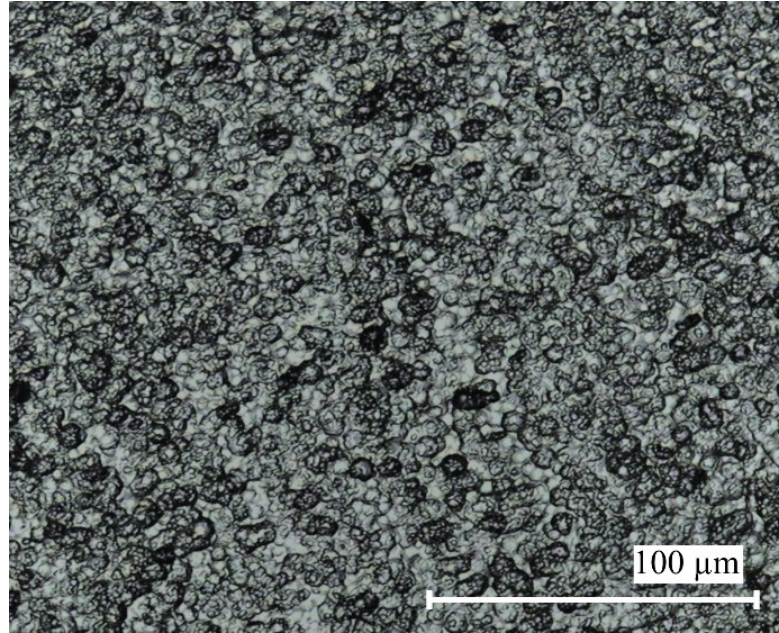


**Figure 8.2:** Microscopic image (obtained with laser scanning microscope type VK-X260K, Keyence) of the surface at the microfluidic channel bottom after the etch process.

centrifugal tube and centrifuged at 4500 rpm for 40 min. The precipitate was then rinsed with water and the procedure repeated to guarantee the precipitation of only the large clusters. The remaining solid was then extensively dried at 80 °C in vacuum and weighed to calculate the  $\chi$  value. Moreover, after each pass through the microchannel, small amount of sample was diluted with water and characterized in terms of radius of gyration ( $R_g$ ) and fractal dimension ( $d_f$ ) of the large clusters by a small-angle light scattering instrument, Mastersizer 2000 (Malvern, U.K.). In particular the radius of gyration ( $R_g$ ) can be derived using the Guinier plot of the average scattering structure factor of the clusters,  $\langle S(q) \rangle$ , as described in Section 4.2.2.

### 8.1.4 Evaluation of the average distance between two neighbor free NPs

The average distance between the surface of two neighbor free NPs ( $D_{ss}$ ) can be evaluated as:

$$D_{ss} = \left( \frac{1 - V_{tot,C}}{N_P} \right)^{\frac{1}{3}} - 2a \quad (8.1)$$

where  $a$  is the NP radius,  $N_P$  is the number concentration of the NPs, which can be estimated as:

$$N_P = \frac{\phi_0}{V_P} (1 - \chi) \quad (8.2)$$

with  $\phi_0$  being the initial volume fraction of the NPs,  $V_P$  the volume of a single NP,  $\chi$  the conversion. The total volume fraction occupied by the clusters,  $V_{tot,C}$  in Equation 8.1, can be evaluated based on the volume of one cluster multiplied by the number of clusters ( $N_C$ ), which can be estimated as:

$$N_C = \chi \frac{\phi_0}{V_P} N_{P,C} \quad (8.3)$$

where  $N_{P,C}$  is the number of NPs within one cluster, given by: [228]

$$N_{P,C} = 4.46 d_f^{-2.08} \left( \frac{R_g}{a} \right)^{d_f} \quad (8.4)$$

### 8.1.5 Details on the computational fluid dynamic simulations

The governing equations. The steady-state Favre-averaged continuity and Navier–Stokes equations are defined as follows:

$$\frac{\partial \langle U_i \rangle}{\partial x_i} = 0 \quad (8.5)$$

$$\langle U_i \rangle \frac{\partial U_i}{\partial x_j} = -\frac{1}{\rho} \frac{\partial \langle p \rangle}{\partial x_i} + \frac{\partial}{\partial x_j} \left( (\mu + \mu_t) \frac{\partial U_i}{\partial x_i} \right) \quad (8.6)$$

where  $\langle U_i \rangle$  is the Reynolds-averaged velocity component in the  $i^{th}$  direction,  $\langle p \rangle$  is the Reynolds-averaged pressure,  $\mu$  and  $\mu_t$  represent the molecular and turbulent viscosity respectively, and  $\rho$  is the density.

Operation conditions and numerical details. The governing equations are solved by the commercial software, ANSYS FLUENT 14.5.7. The unstructured hexahedral cells are created by ICEM. The grids of SZ-MC and DZ-MC consist of 1094662 and 2101720 cells, respectively. Both the grids are refined near the wall. The employed spatial numerical scheme is a second-order upwind scheme and the pressure–velocity coupling is solved with the SIMPLE algorithm. The pressure inlet boundary conditions are employed for the inflows while the pressure outlet condition is assumed at the outflow. The standard  $k$ - $\epsilon$  turbulence model coupled with the standard approach for the wall treatment is employed to simulate three dimensional flow field. The mean velocity and mean shear rate are calculated as follow:

$$v_m = \frac{\sum v \cdot V_{cell}}{\sum V_{cell}} \quad (8.7)$$

$$\dot{\gamma} = \frac{\sum \gamma \cdot V_{cell}}{\sum V_{cell}} \quad (8.8)$$

where  $V_{cell}$  is the volume of each cell at the microchannel zone,  $v$  and the  $\gamma$  are the velocity and shear rate at the computational cell, respectively.

## 8.2 PVdF-HFP and Ionic Liquid-Based, Freestanding Thin Separator for Lithium-Ion Batteries

### 8.2.1 Properties of the aqueous dispersion of PVdF-HFP NPs

The PVdF-HFP nanoparticles (NPs) contain about 5 mol% of HFP and were obtained through emulsion polymerization using an anionic surfactant as the stabilizer. The properties of the latex are reported in Table 8.1.

**Table 8.1: Physical and chemical properties of the aqueous dispersion of PVdF-HFP NPs.**

Radius	PDI	Conductivity	Surface tension	$\zeta$ potential	pH	NPs mass fraction
[nm]	[-]	$[\mu\text{S cm}^{-1}]$	$[\text{mN m}^{-1}]$	[mV]	[-]	[%]
140	0.03	920	62.70	-30	2.8	24.1

The average radius of the polymer NPs and the polydispersity index (PDI) are measured by dynamic light scattering using Zetasizer Nano ZS 3600 (Malvern Instruments). The conductivity is measured with Conductometer 712 (Metrohm) at a concentration of 5 wt.% and 25 °C. The surface tension measurements are performed with a Wilhelmy plate using DCAT 21 (Dataphysics) at a concentration of 0.5 wt.% and 25 °C. The solid content is assessed by spreading the sample over quartz sand and analyzing the weight loss at 120 °C using a HG53 Halogen Moisture Analyzer (Mettler-Toledo).

## 8.2.2 DSC results

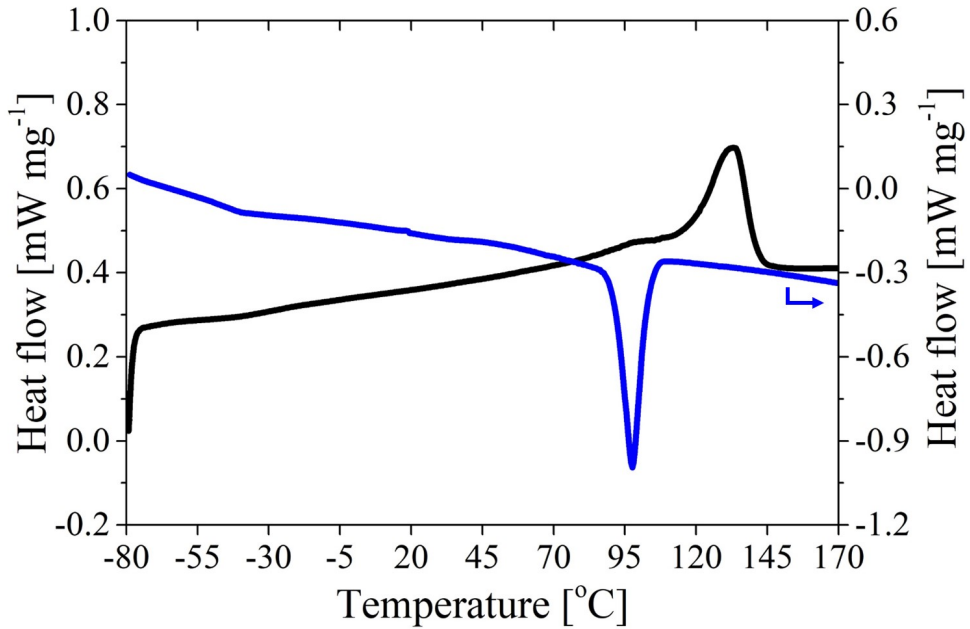


Figure 8.3: DSC curves of PVdF-HFP: heating (black) and cooling (blue) profiles.

Table 8.2: Properties of PVdF-HFP, derived from DSC curves.  $T_m$ : Melting temperature.  $T_C$ : Crystallization temperature.  $\Delta H_m$ : Enthalpy of melting.  $X_C$ : Crystallinity.

$T_m$	$T_C$	$\Delta H_m$	$X_C$
[°C]	[°C]	[J g <sup>-1</sup> ]	[%]
133.6	97.6	22.2	21.2

### 8.2.3 Morphology of the PCIL membrane prepared at PC/IL = 20/80

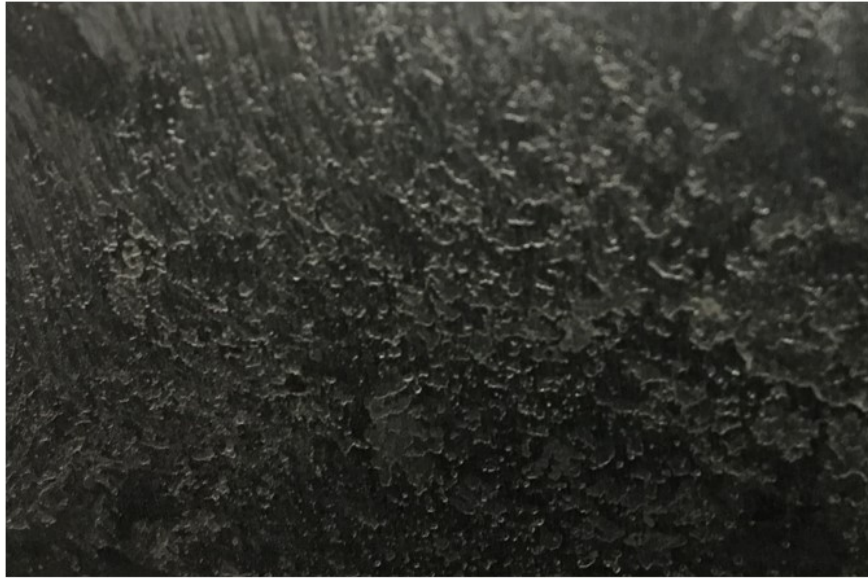


Figure 8.4: Morphology of the PCIL membrane prepared at PC/IL = 20/80.



## 8.3 Effect of SiO<sub>2</sub> Nanoparticles on the Performance of PVdF-HFP/Ionic Liquid Separator for Lithium-Ion Batteries

### 8.3.1 Ionic conductivity results

Table 8.3: Ionic conductivity of the P*Si*CIL membranes in the temperature range from 25 to 80 °C at different percentages of silica (with respect to the polymer).

wt.% of SiO <sub>2</sub>	Ionic conductivity [mS cm <sup>-1</sup> ]				
	25 °C	40 °C	55 °C	70 °C	80 °C
0	0.51	0.78	1.22	1.77	2.29
5	1.04	1.54	2.08	2.51	2.88
10	1.22	1.77	2.51	2.95	3.23
15	0.71	1.04	1.54	2.08	2.69

## 8.4 Core-Shell Morphology of Redispersible Powders in Polymer-Cement Waterproof Mortars

### 8.4.1 Syntheses conditions

The exact amounts and conditions of the synthesis of the samples are shown in Tables 8.4 and 8.5.

**Table 8.4:** Reaction formulations for different core-shell particles for samples *a-e*. All reactions were run at 80 °C with a stirring speed of 200 rpm.

	Sample	<i>a</i>	<i>b</i>	<i>c</i>	<i>d</i>	<i>e</i>
IC	MAPTAC (50 wt.%) [g]	15.1	15.1	15.1	13.6	16.6
	Water [g]	370	370	370	370	370
IS	V-50 [g]	0.9	0.9	0.9	1	1
	Water [g]	10	10	10	11	11
CF	STY [g]	42	42	42	42	42
	2-EHA [g]	126	126	126	126	126
	Feeding time [hr]	3	3	3	3	3
WT	Waiting time [hr]	1	1	1	1	1
SF	STY [g]	33.6	37.8	41.6	16.8	50.4
	2-EHA [g]	8.4	4.2	0.42	4.2	12.6
	Feeding time [hr]	1	1	1	1	1
IF	V-50 [g]	1.8	1.8	1.8	1.5	2
	Water [g]	18	18	18	19.5	20
	Feeding time [hr]	6	6	6	6	6

**Table 8.5: Reaction formulations for different core-shell particles for samples *f-j*. All reactions were run at 80 °C with a stirring speed of 200 rpm.**

	Sample	<i>f</i>	<i>g</i>	<i>h</i>	<i>i</i>	<i>j</i>
IC	MAPTAC (50 wt.%) [g]	15.1	15.1	15.1	15.1	15.1
	Water [g]	370	370	370	370	370
IS	V-50 [g]	0.95	0.9	0.9	0.9	0.9
	Water [g]	10	10	10	10	10
CF	STY [g]	47.2	35	35	35	52.5
	2-EHA [g]	141.8	105	105	105	157.5
	Feeding time [hr]	3.5	2.5	2.5	2.5	4
WT	Waiting time [hr]	1	1.5	1.5	1.5	-
SF	STY [g]	16.8	56	63	69.3	-
	2-EHA [g]	4.2	14	7	0.7	-
	Feeding time [hr]	0.5	1.5	1.5	1.5	-
IF	V-50 [g]	1.8	1.8	1.8	1.8	1.8
	Water [g]	18	18	18	18	18
	Feeding time [hr]	6	6.5	6.5	6.5	6

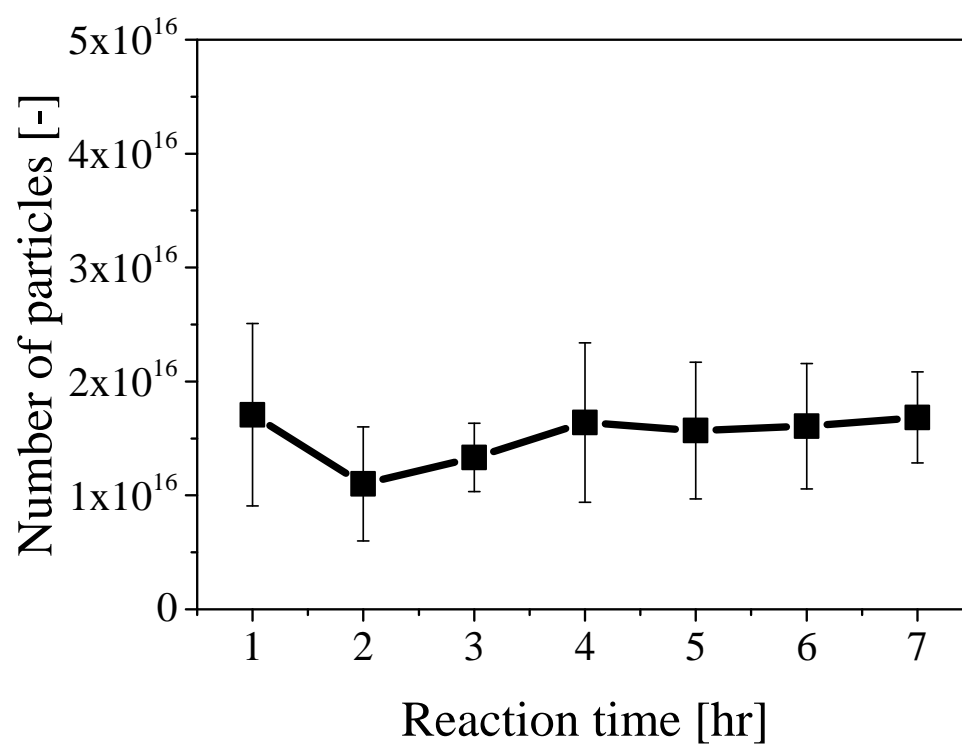


Figure 8.5: Number of polymer particles in the reactor during the synthesis of sample *a*.

### 8.4.2 Syntheses results

**Table 8.6:** Surface zeta potential, pH value and film-forming ability of the synthesized latexes.

Sample	Zeta potential [mV]	pH	Film-forming
<i>a</i>	48.8	6.75	Yes
<i>b</i>	54.5	6.32	Yes
<i>c</i>	51.8	6.69	Yes
<i>d</i>	50.8	6.69	Yes
<i>e</i>	50.9	6.75	Yes
<i>f</i>	50.5	6.46	Yes
<i>g</i>	47.4	6.44	Yes
<i>h</i>	50.8	6.11	Yes
<i>i</i>	50.0	6.52	Yes
<i>j</i>	52.2	6.27	Yes

### 8.4.3 Polymer-cement membranes

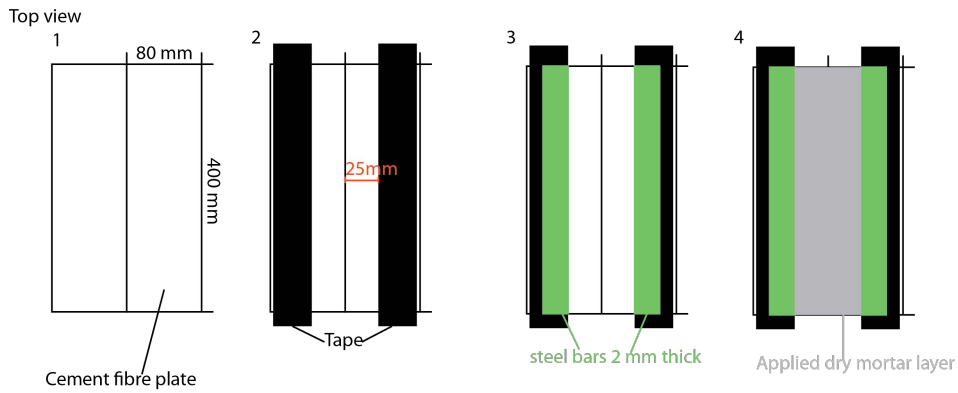


Figure 8.6: Sketch of the membrane preparation procedure for crack-bridging tests.



Figure 8.7: Cement-based membrane obtained with polymer *h* (left) and *i* (right), after spray drying.

### 8.4.4 NMR results and evaluation

The recorded NMR spectra were evaluated by integrating the peaks to measure the polymer composition. The full results are shown in Table 8.7. The samples taken after one hour had a too low concentration for a reasonable evaluation as the conversion was still relatively low.

**Table 8.7: 2-EHA mass content of the cumulative polymer particles during the reaction.**

Sample	2 hr	3 hr	4 hr	5 hr	6 hr	7 hr
<i>a</i>	0.76	0.73	0.74	0.71	0.69	0.66
<i>b</i>	0.71	0.70	0.73	0.74	0.69	0.66
<i>c</i>	0.73	0.76	0.74	0.75	0.7	0.67
<i>d</i>	0.68	0.68	0.72	0.74	0.73	0.72
<i>e</i>	0.73	0.70	0.71	0.73	0.68	0.65
<i>f</i>	0.69	0.68	0.7	0.73	0.73	0.72
<i>g</i>	0.72	0.71	0.74	0.7	0.63	0.61
<i>h</i>	0.76	0.69	0.72	0.69	0.61	0.59
<i>i</i>	0.77	0.78	0.73	0.69	0.59	0.53
<i>j</i>	0.73	0.77	0.74	0.74	0.76	0.75

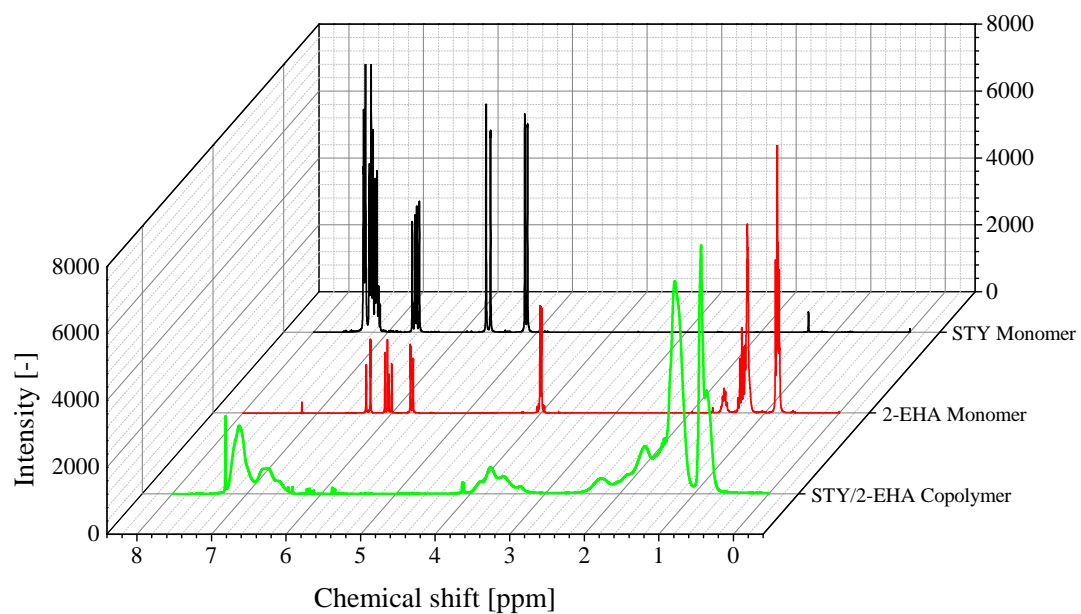


Figure 8.8: NMR spectra for the monomers STY (black curve) and 2-EHA (red curve) and for the copolymer STY/2-EHA *a* (green curve).



# Bibliography

- [1] J. N. Israelachvili, *Intermolecular and surface forces*. Academic press, 2011.
- [2] M. Smoluchowski, An experiment on mathematical theorization of coagulation kinetics of the colloidal solutions. *Z. Phys. Chem.*, 1917, 92, 129–168.
- [3] Y. Dkhissi, S. Meyer, D. Chen, H. C. Weerasinghe, L. Spiccia, Y.-B. Cheng, R. A. Caruso, Stability comparison of perovskite solar cells based on zinc oxide and titania on polymer substrates. *ChemSusChem*, 2016, 9 (7), 687–695.
- [4] A. Dias, A. Hussain, A. Marcos, A. Roque, A biotechnological perspective on the application of iron oxide magnetic colloids modified with polysaccharides. *Biotechnol. Adv.*, 2011, 29 (1), 142–155.
- [5] M. Karg, T. A. König, M. Retsch, C. Stelling, P. M. Reichstein, T. Honold, M. Thelakkat, A. Fery, Colloidal self-assembly concepts for light management in photovoltaics. *Mater. Today*, 2015, 18 (4), 185–205.
- [6] S. Kumar, J. Jagielski, N. Kallikounis, Y.-H. Kim, C. Wolf, F. Jenny, T. Tian, C. J. Hofer, Y.-C. Chiu, W. J. Stark, *et al.*, Ultrapure green light-emitting diodes using two-dimensional formamidinium perovskites: achieving recommendation 2020 color coordinates. *Nano Lett.*, 2017, 17 (9), 5277–5284.
- [7] S. K. Mishra, J. Ferreira, S. Kannan, Mechanically stable antimicrobial chitosan-PVA-silver nanocomposite coatings deposited on titanium implants. *Carbohydr. Polym.*, 2015, 121, 37–48.
- [8] N. D. Trinh, T. T. B. Nguyen, T. H. Nguyen, Preparation and characterization of silver chloride nanoparticles as an antibacterial agent. *Adv. Nat. Sci.: Nanosci. Nanotech.*, 2015, 6 (4), 045011.
- [9] H. Hamaker, The London-van der Waals attraction between spherical particles. *Physica*, 1937, 4 (10), 1058–1072.
- [10] B. Derjaguin, L. Landau, Theory of the stability of strongly charged lyophobic sols and of the adhesion of strongly charged particles in solution of electrolytes. *Acta Physicochim., USSR*, 1941, 14, 633–662.
- [11] E. J. W. Verwey, J. T. G. Overbeek, J. T. G. Overbeek, *Theory of the stability of lyophobic colloids*. Courier Corporation, 1999.

## BIBLIOGRAPHY

---

- [12] M. Lattuada, H. Wu, P. Sandkühler, J. Sefcik, M. Morbidelli, Modelling of aggregation kinetics of colloidal systems and its validation by light scattering measurements. *Chem. Eng. Sci.*, 2004, 59 (8-9), 1783–1798.
- [13] M. Lattuada, P. Sandkühler, H. Wu, J. Sefcik, M. Morbidelli, Aggregation kinetics of polymer colloids in reaction limited regime: experiments and simulations. *Adv. Colloid Interface Sci.*, 2003, 103 (1), 33–56.
- [14] v. N. Fuchs, Über die Stabilität und Aufladung der Aerosole. *Z. Phys.*, 1934, 89 (11-12), 736–743.
- [15] M. Lin, H. Lindsay, D. Weitz, R. Ball, R. Klein, P. Meakin, Universality in colloid aggregation. *Nature*, 1989, 339 (6223), 360.
- [16] A. Zaccone, H. Wu, M. Lattuada, M. Morbidelli, Correlation between colloidal stability and surfactant adsorption/association phenomena studied by light scattering. *J. Phys. Chem. B*, 2008, 112, 1976–1986.
- [17] H. Wu, S. Lodi, M. Morbidelli, Characterization of particle interaction energy through incipient turbulent aggregation. *J. Colloid Interface Sci.*, 2002, 256, 304–313.
- [18] A. Zaccone, H. Wu, M. Lattuada, M. Morbidelli, Charged molecular films on Brownian particles: structure, interactions, and relation to stability. *J. Phys. Chem. B*, 2008, 112, 6793–6802.
- [19] Y. M. Harshe, M. Lattuada, M. Soos, Experimental and modeling study of breakage and restructuring of open and dense colloidal aggregates. *Langmuir*, 2011, 27 (10), 5739–5752.
- [20] O. Okay, Macroporous copolymer networks. *Prog. Polym. Sci.*, 2000, 25, 711–779.
- [21] R. Kunin, E. Meitzner, N. Bortnick, Macroreticular ion exchange resins. *J. Am. Chem. Soc.*, 1962, 84, 305–306.
- [22] A. Lamprou, *Synthesis and application of novel polymeric materials: short surfactants via ATRP and functional macroporous particles via reactive gelation under shear*. Ph.D. thesis, ETH Zurich, 2012.
- [23] C. Gauer, Z. Jia, H. Wu, M. Morbidelli, Aggregation kinetics of coalescing polymer colloids. *Langmuir*, 2009, 25, 9703–9713.
- [24] P. Arosio, D. Xie, H. Wu, L. Braun, M. Morbidelli, Effect of primary particle morphology on the structure of gels formed in intense turbulent shear. *Langmuir*, 2010, 26, 6643–6649.
- [25] H. Wu, J. Xie, M. Lattuada, J. Kohlbrecher, M. Morbidelli, Effect of primary particle size and salt concentration on the structure of colloidal gels. *J. Phys. Chem. C*, 2011, 115, 931–936.

## BIBLIOGRAPHY

---

- [26] M. Lattuada, H. Wu, M. Morbidelli, A simple model for the structure of fractal aggregates. *J. Colloid Interface Sci.*, 2003, 268, 106–120.
- [27] P. Meakin, Fractal aggregates. *Adv. Colloid Interface Sci.*, 1988, 28, 249–331.
- [28] M. Kolb, R. Botet, R. Jullien, Scaling of kinetically growing clusters. *Phys. Rev. Lett.*, 1983, 51, 1123–1126.
- [29] B. B. Mandelbrot, *The fractal geometry of nature*, volume 1. WH freeman New York, 1982.
- [30] P. J. Flory, *Principles of polymer chemistry*. Cornell University Press, 1953.
- [31] J. M. Asua, Emulsion polymerization: from fundamental mechanisms to process developments. *J. Polym. Sci., Part A: Polym. Chem.*, 2004, 42 (5), 1025–1041.
- [32] Y. Ohama, Polymer-based admixtures. *Cem. Concr. Compos.*, 1998, 20 (2-3), 189–212.
- [33] M. Miller, *Polymers in cementitious materials*. iSmithers Rapra Publishing, 2005.
- [34] H.-G. Elias, Plastics, general survey. *Ullmann's Encyclopedia of Industrial Chemistry*, 2000.
- [35] R. Jovanović, M. Dube, Emulsion-based pressure-sensitive adhesives: a review. *J. Macromol. Sci., Polym. Rev.*, 2004, 44 (1), 1–51.
- [36] M. Yokouchi, S. Seto, Y. Kobayashi, Comparison of polystyrene, poly (styrene/acrylonitrile), high-impact polystyrene, and poly (acrylonitrile/butadiene/styrene) with respect to tensile and impact properties. *J. Appl. Polym. Sci.*, 1983, 28 (7), 2209–2216.
- [37] S. Ramakrishna, J. Mayer, E. Wintermantel, K. W. Leong, Biomedical applications of polymer-composite materials: a review. *Compos. Sci. Technol.*, 2001, 61 (9), 1189–1224.
- [38] S. Stankovich, D. A. Dikin, G. H. Dommett, K. M. Kohlhaas, E. J. Zimney, E. A. Stach, R. D. Piner, S. T. Nguyen, R. S. Ruoff, Graphene-based composite materials. *Nature*, 2006, 442 (7100), 282.
- [39] D. Gay, S. V. Hoa, *Composite materials: design and applications*. CRC press, 2007.
- [40] J. R. Vinson, T.-W. Chou, *Composite materials and their use in structures*. Halsted press, 1975.
- [41] K. K. Chawla, *Composite materials: science and engineering*. Springer Science & Business Media, 2012.

## BIBLIOGRAPHY

---

- [42] A. Zaccone, H. Wu, D. Gentili, M. Morbidelli, Theory of activated-rate processes under shear with application to shear-induced aggregation of colloids. *Phys. Rev. E*, 2009, 80 (5), 051404.
- [43] A. Zaccone, D. Gentili, H. Wu, M. Morbidelli, Shear-induced reaction-limited aggregation kinetics of brownian particles at arbitrary concentrations. *J. Chem. Phys.*, 2010, 132 (13), 134903.
- [44] X. Meng, H. Wu, M. Morbidelli, Kinetics and cluster morphology evolution of shear-driven aggregation of well-stabilized colloids. *Langmuir*, 2015, 31 (3), 1113–1119.
- [45] X. Sheng, D. Xie, X. Zhang, L. Zhong, H. Wu, M. Morbidelli, Uniform distribution of graphene oxide sheets into a poly-vinylidene fluoride nanoparticle matrix through shear-driven aggregation. *Soft Matter*, 2016, 12 (27), 5876–5882.
- [46] N. Koumakis, E. Moghimi, R. Besseling, W. C. K. Poon, J. F. Brady, G. Pektikidis, Tuning colloidal gels by shear. *Soft Matter*, 2015, 11 (23), 4640–4648.
- [47] R. C. Sonntag, W. B. Russel, Structure and breakup of flocs subjected to fluid stresses: I. shear experiments. *J. Colloid Interface Sci.*, 1986, 113 (2), 399–413.
- [48] R. C. Sonntag, W. B. Russel, Structure and breakup of flocs subjected to fluid stresses: II. theory. *J. Colloid Interface Sci.*, 1987, 115 (2), 378–389.
- [49] R. Wessel, R. Ball, Fractal aggregates and gels in shear flow. *Phys. Rev. A*, 1992, 46 (6), R3008.
- [50] D. L. Xie, H. Wu, A. Zaccone, L. Braun, H. Q. Chen, M. Morbidelli, Criticality for shear-induced gelation of charge-stabilized colloids. *Soft Matter*, 2010, 6 (12), 2692–2698.
- [51] D. W. Green, R. H. Perry, *Perry's Chemical Engineers' Handbook*. McGraw-Hill, New York, 8th edition, 2007.
- [52] P. Erfle, J. Riewe, H. Bunjes, A. Dietzel, Optically monitored segmented flow for controlled ultra-fast mixing and nanoparticle precipitation. *Microfluidics Nanofluidics*, 2017, 21 (12), 179.
- [53] T. Lorenz, S. Bojko, H. Bunjes, A. Dietzel, An inert 3D emulsification device for individual precipitation and concentration of amorphous drug nanoparticles. *Lab Chip*, 2018, 18 (4), 627–638.
- [54] P. C. Valente, J. C. Vassilicos, Universal dissipation scaling for nonequilibrium turbulence. *Phys. Rev. Lett.*, 2012, 108 (21), 214503.
- [55] S. Goto, J. Vassilicos, Unsteady turbulence cascades. *Phys. Rev. E*, 2016, 94 (5), 053108.

## BIBLIOGRAPHY

---

- [56] S. Caimi, A. Cingolani, B. Jaquet, M. Siggel, M. Lattuada, M. Morbidelli, Tracking of fluorescently labeled polymer particles reveals surface effects during shear-controlled aggregation. *Langmuir*, 2017, 33 (49), 14038–14044.
- [57] L. Ehrl, M. Soos, M. Morbidelli, Dependence of aggregate strength, structure, and light scattering properties on primary particle size under turbulent conditions in stirred tank. *Langmuir*, 2008, 24 (7), 3070–3081.
- [58] A. S. Moussa, M. Lattuada, B. O. Conchúir, A. Zaccone, M. Morbidelli, M. Soos, Flow-induced aggregation and breakup of particle clusters controlled by surface nanoroughness. *Langmuir*, 2013, 29 (47), 14386–14395.
- [59] R. C. Elgebrandt, J. A. Romagnoli, D. F. Fletcher, V. G. Gomes, R. G. Gilbert, Analysis of shear-induced coagulation in an emulsion polymerisation reactor using computational fluid dynamics. *Chem. Eng. Sci.*, 2005, 60 (7).
- [60] G. De Boer, G. Hoedemakers, D. Thoenes, Coagulation in turbulent flow: Part I. *Chem. Eng. Res. Des.*, 1989, 67, 301–307.
- [61] T. Serra, X. Casamitjana, Structure of the aggregates during the process of aggregation and breakup under a shear flow. *J. Colloid Interface Sci.*, 1998, 206 (2), 505–511.
- [62] T. Serra, X. Casamitjana, Effect of the shear and volume fraction on the aggregation and breakup of particles. *AIChE J.*, 1998, 44 (8), 1724–1730.
- [63] M. Soos, A. S. Moussa, L. Ehrl, J. Sefcik, H. Wu, M. Morbidelli, Effect of shear rate on aggregate size and morphology investigated under turbulent conditions in stirred tank. *J. Colloid Interface Sci.*, 2008, 319 (2), 577–589.
- [64] F. Sciortino, E. Zaccarelli, Reversible gels of patchy particles. *Curr. Opin. Solid State Mater. Sci.*, 2011, 15 (6), 246–253.
- [65] S. Lazzari, L. Nicoud, B. Jaquet, M. Lattuada, M. Morbidelli, Fractal-like structures in colloid science. *Adv. Colloid Interface Sci.*, 2016, 235, 1–13.
- [66] C. S. Hodges, J. A. Cleaver, M. Ghadiri, R. Jones, H. M. Pollock, Forces between polystyrene particles in water using the AFM: pull-off force vs particle size. *Langmuir*, 2002, 18 (15), 5741–5748.
- [67] C. S. Hodges, L. Looi, J. A. Cleaver, M. Ghadiri, Use of the JKR model for calculating adhesion between rough surfaces. *Langmuir*, 2004, 20 (22), 9571–9576.
- [68] D. Quesnel, D. Rimai, L. Demejo, Molecular dynamic simulation of adhesion release of particles from surfaces. *J. Adhes.*, 1998, 67 (1-4), 235–257.
- [69] E. Eiser, F. Molino, G. Porte, X. Pithon, Flow in micellar cubic crystals. *Rheol. Acta*, 2000, 39 (3), 201–208.

## BIBLIOGRAPHY

---

- [70] J. Vermant, M. Solomon, Flow-induced structure in colloidal suspensions. *J. Phys.: Condens. Matter*, 2005, 17 (4), R187.
- [71] J. B. Pawley, *Fundamental limits in confocal microscopy*. Springer, 2006, 20–42.
- [72] H. Zeng, *Polymer adhesion, friction, and lubrication*. John Wiley and Sons, 2013.
- [73] J. Brandrup, E. Immergut, E. Grulke, *Polymer Handbook*. John Wiley and Sons Inc, 1999.
- [74] L. Cova, P. Bigini, V. Diana, L. Sitia, R. Ferrari, R. M. Pesce, R. Khalaf, P. Bossolasco, P. Ubezio, M. Lupi, Biocompatible fluorescent nanoparticles for in vivo stem cell tracking. *Nanotechnology*, 2013, 24 (24), 245603.
- [75] L. Ki-Chang, W. Han-Ah, Synthesis of crosslinked polystyrene particles by seeded batch polymerization with monomer absorption. *Trans. Nonferrous Met. Soc. China*, 2011, 21, s153–s159.
- [76] M. Soos, R. Kaufmann, R. Winteler, M. Kroupa, B. Lüthi, Determination of maximum turbulent energy dissipation rate generated by a rushton impeller through large eddy simulation. *AIChE J.*, 2013, 59 (10), 3642–3658.
- [77] T. Chow, Molecular interpretation of the glass transition temperature of polymer-diluent systems. *Macromolecules*, 1980, 13 (2), 362–364.
- [78] S.-H. Kim, A. D. Hollingsworth, S. Sacanna, S.-J. Chang, G. Lee, D. J. Pine, G.-R. Yi, Synthesis and assembly of colloidal particles with sticky dimples. *J. Am. Chem. Soc.*, 2012, 134 (39), 16115–16118.
- [79] S. Sacanna, M. Korpics, K. Rodriguez, L. Colón-Meléndez, S.-H. Kim, D. J. Pine, G.-R. Yi, Shaping colloids for self-assembly. *Nat. Comm.*, 2013, 4, 1688.
- [80] S. K. Friedlander, *Smoke, dust and haze: fundamentals of aerosol behavior*. Oxford University Press, New York, 2000.
- [81] C. M. Sorensen, G. C. Roberts, The prefactor of fractal aggregates. *J. Colloid Interface Sci.*, 1997, 186 (2), 447–452.
- [82] M. U. Bäbler, A collision efficiency model for flow-induced coagulation of fractal aggregates. *AIChE J.*, 2008, 54, 1748–1760.
- [83] J.-M. Tarascon, M. Armand, Issues and challenges facing rechargeable lithium batteries. *Nature*, 2001, 414, 359–367.
- [84] J. Kalhoff, G. G. Eshetu, D. Bresser, S. Passerini, Safer electrolytes for lithium-ion batteries: state of the art and perspectives. *ChemSusChem*, 2015, 8 (13), 2154–2175.

## BIBLIOGRAPHY

---

- [85] M. Armand, J.-M. Tarascon, Building better batteries. *Nature*, 2008, 451 (7179), 652–657.
- [86] B. Scrosati, J. Garche, Lithium batteries: status, prospects and future. *J Power Sources*, 2010, 195 (9), 2419–2430.
- [87] B. Scrosati, J. Hassoun, Y.-K. Sun, Lithium-ion batteries. a look into the future. *Energy Environ. Sci.*, 2011, 4 (9), 3287–3295.
- [88] B. Dunn, H. Kamath, J.-M. Tarascon, Electrical energy storage for the grid: a battery of choices. *Science*, 2011, 334 (6058), 928–935.
- [89] M. M. Thackeray, C. Wolverton, E. D. Isaacs, Electrical energy storage for transportation—approaching the limits of, and going beyond, lithium-ion batteries. *Energy Environ. Sci.*, 2012, 5 (7), 7854–7863.
- [90] S. S. Zhang, A review on the separators of liquid electrolyte Li-ion batteries. *J. Power Sources*, 2007, 164 (1), 351–364.
- [91] B. Scrosati, *Applications of electroactive polymers*, volume 75. Springer, 1993.
- [92] C. Daniel, J. O. Besenhard, *Handbook of Battery Materials*. Wiley-VCH Verlag GmbH & Co. KGaA: Weinheim, 2011.
- [93] J. Nunes-Pereira, C. Costa, S. Lanceros-Mendez, Polymer composites and blends for battery separators: state of the art, challenges and future trends. *J. Power Sources*, 2015, 281, 378–398.
- [94] H. Lee, M. Yanilmaz, O. Toprakci, K. Fu, X. Zhang, A review of recent developments in membrane separators for rechargeable lithium-ion batteries. *Energy Environ. Sci.*, 2014, 7 (12), 3857–3886.
- [95] G. G. Eshetu, S. Grugeon, S. Laruelle, S. Boyanov, A. Lecocq, J.-P. Bertrand, G. Marlair, In-depth safety-focused analysis of solvents used in electrolytes for large scale lithium-ion batteries. *Phys. Chem. Chem. Phys.*, 2013, 15 (23), 9145–9155.
- [96] A. J. Bhattacharyya, J. Maier, Second phase effects on the conductivity of non-aqueous salt solutions: "soggy sand electrolytes". *Adv. Mater.*, 2004, 16 (9-10), 811–814.
- [97] X. Bian, L. Shi, X. Yang, X. Lu, Effect of nano-TiO<sub>2</sub> particles on the performance of PVDF, PVDF-g-(maleic anhydride), and PVDF-g-poly (acryl amide) membranes. *Ind. Eng. Chem. Res.*, 2011, 50 (21), 12113–12123.
- [98] H. Liu, J. Xu, B. Guo, X. He, Preparation and performance of silica/polypropylene composite separator for lithium-ion batteries. *J. Mater. Sci.*, 2014, 49 (20), 6961–6966.

## BIBLIOGRAPHY

---

- [99] K. Xu, Nonaqueous liquid electrolytes for lithium-based rechargeable batteries. *Chem. Rev.*, 2004, 104 (10), 4303–4418.
- [100] A. Hammami, N. Raymond, M. Armand, Lithium-ion batteries: runaway risk of forming toxic compounds. *Nature*, 2003, 424 (6949), 635–636.
- [101] P.-L. Kuo, C.-H. Tsao, C.-H. Hsu, S.-T. Chen, H.-M. Hsu, A new strategy for preparing oligomeric ionic liquid gel polymer electrolytes for high-performance and nonflammable lithium ion batteries. *J. Membr. Sci.*, 2016, 499, 462–469.
- [102] H. W. Rollins, M. K. Harrup, E. J. Dufek, D. K. Jamison, S. V. Sazhin, K. L. Gering, D. L. Daubaras, Fluorinated phosphazene co-solvents for improved thermal and safety performance in lithium-ion battery electrolytes. *J. Power Sources*, 2014, 263, 66–74.
- [103] Y.-S. Ye, J. Rick, B.-J. Hwang, Ionic liquid polymer electrolytes. *J. Mater. Chem. A*, 2013, 1 (8), 2719–2743.
- [104] D. R. MacFarlane, N. Tachikawa, M. Forsyth, J. M. Pringle, P. C. Howlett, G. D. Elliott, J. H. Davis, M. Watanabe, P. Simon, C. A. Angell, Energy applications of ionic liquids. *Energy Environ. Sci.*, 2014, 7 (1), 232–250.
- [105] Y. Lu, S. S. Moganty, J. L. Schaefer, L. A. Archer, Ionic liquid-nanoparticle hybrid electrolytes. *J. Mater. Chem.*, 2012, 22 (9), 4066–4072.
- [106] P. Arora, Z. Zhang, Battery separators. *Chem. Rev.*, 2004, 104 (10), 4419–4462.
- [107] J.-A. Choi, S. H. Kim, D.-W. Kim, Enhancement of thermal stability and cycling performance in lithium-ion cells through the use of ceramic-coated separators. *J. Power Sources*, 2010, 195 (18), 6192–6196.
- [108] I. Uchida, H. Ishikawa, M. Mohamedi, M. Umeda, AC-impedance measurements during thermal runaway process in several lithium/polymer batteries. *J. Power Sources*, 2003, 119–121, 821–825.
- [109] X. Cao, X. He, J. Wang, H. Liu, S. Röser, B. R. Rad, M. Evertz, B. Streipert, J. Li, R. Wagner, High voltage  $\text{LiNi}_{0.5}\text{Mn}_{1.5}\text{O}_4/\text{Li}_4\text{Ti}_5\text{O}_{12}$  lithium ion cells at elevated temperatures: carbonate-versus ionic liquid-based electrolytes. *ACS Appl. Mater. Interfaces*, 2016, 8 (39), 25971–25978.
- [110] V. Borgel, E. Markevich, D. Aurbach, G. Semrau, M. Schmidt, On the application of ionic liquids for rechargeable Li batteries: high voltage systems. *J. Power Sources*, 2009, 189 (1), 331–336.
- [111] R. A. Di Leo, A. C. Marschilok, K. J. Takeuchi, E. S. Takeuchi, Battery electrolytes based on saturated ring ionic liquids: physical and electrochemical properties. *Electrochim. Acta*, 2013, 109, 27–32.



## BIBLIOGRAPHY

---

- [112] S. F. Lux, M. Schmuck, G. B. Appetecchi, S. Passerini, M. Winter, A. Balducci, Lithium insertion in graphite from ternary ionic liquid–lithium salt electrolytes: II. evaluation of specific capacity and cycling efficiency and stability at room temperature. *J. Power Sources*, 2009, 192 (2), 606–611.
- [113] R. W. Schmitz, P. Murmann, R. Schmitz, R. Müller, L. Krämer, J. Kasnatscheew, P. Isken, P. Niehoff, S. Nowak, G.-V. Roeschenthaler, Investigations on novel electrolytes, solvents and SEI additives for use in lithium-ion batteries: systematic electrochemical characterization and detailed analysis by spectroscopic methods. *Prog. Solid State Chem.*, 2014, 42 (4), 65–84.
- [114] P. Wasserscheid, W. Keim, Ionic liquids–new “solutions” for transition metal catalysis. *Angew. Chem. Int. Ed.*, 2000, 39 (21), 3772–3789.
- [115] J. L. Anderson, J. Ding, T. Welton, D. W. Armstrong, Characterizing ionic liquids on the basis of multiple solvation interactions. *J. Am. Chem. Soc.*, 2002, 124 (47), 14247–14254.
- [116] J. Dupont, R. F. de Souza, P. A. Suarez, Ionic liquid (molten salt) phase organometallic catalysis. *Chem. Rev.*, 2002, 102 (10), 3667–3692.
- [117] J.-H. Shin, W. A. Henderson, S. Passerini, PEO-based polymer electrolytes with ionic liquids and their use in lithium metal-polymer electrolyte batteries. *J. Electrochem. Soc.*, 2005, 152 (5), A978–A983.
- [118] M. Armand, F. Endres, D. R. MacFarlane, H. Ohno, B. Scrosati, Ionic-liquid materials for the electrochemical challenges of the future. *Nat. Mater.*, 2009, 8 (8), 621–629.
- [119] M. Watanabe, M. L. Thomas, S. Zhang, K. Ueno, T. Yasuda, K. Dokko, Application of ionic liquids to energy storage and conversion materials and devices. *Chem. Rev.*, 2017, 117 (10), 7190–7239.
- [120] H. Ohno, *Electrochemical aspects of ionic liquids*. John Wiley & Sons, 2005.
- [121] A. Matic, B. Scrosati, Ionic liquids for energy applications. *MRS Bull.*, 2013, 38 (7), 533–537.
- [122] N. Plylahan, M. Kerner, D.-H. Lim, A. Matic, P. Johansson, Ionic liquid and hybrid ionic liquid/organic electrolytes for high temperature lithium-ion battery application. *Electrochim. Acta*, 2016, 216, 24–34.
- [123] R. Leones, C. Costa, A. Machado, J. Esperança, M. M. Silva, S. Lanceros-Mendez, Effect of ionic liquid anion type in the performance of solid polymer electrolytes based on poly (vinylidene fluoride-trifluoroethylene). *Electroanalysis*, 2015, 27 (2), 457–464.

## BIBLIOGRAPHY

---

- [124] S. Ferrari, E. Quartarone, P. Mustarelli, A. Magistris, M. Fagnoni, S. Protti, C. Gerbaldi, A. Spinella, Lithium ion conducting PVdF-HFP composite gel electrolytes based on N-methoxyethyl-N-methylpyrrolidinium bis (trifluoromethanesulfonyl)-imide ionic liquid. *J. Power Sources*, 2010, 195 (2), 559–566.
- [125] D. R. MacFarlane, J. Huang, M. Forsyth, Lithium-doped plastic crystal electrolytes exhibiting fast ion conduction for secondary batteries. *Nature*, 1999, 402 (6763), 792–794.
- [126] D. R. MacFarlane, M. Forsyth, P. C. Howlett, J. M. Pringle, J. Sun, G. Anat, W. Neil, E. I. Izgorodina, Ionic liquids in electrochemical devices and processes: managing interfacial electrochemistry. *Acc. Chem. Res.*, 2007, 40 (11), 1165–1173.
- [127] G. B. Appetecchi, S. Scaccia, C. Tizzani, F. Alessandrini, S. Passerini, Synthesis of hydrophobic ionic liquids for electrochemical applications. *J. Electrochem. Soc.*, 2006, 153 (9), A1685–A1691.
- [128] S. P. Ong, O. Andreussi, Y. Wu, N. Marzari, G. Ceder, Electrochemical windows of room-temperature ionic liquids from molecular dynamics and density functional theory calculations. *Chem. Mater.*, 2011, 23 (11), 2979–2986.
- [129] Q. Zhou, P. D. Boyle, L. Malpezzi, A. Mele, J.-H. Shin, S. Passerini, W. A. Henderson, Phase behavior of ionic liquid-LiX mixtures: Pyrrolidinium cations and TFSI-anions-linking structure to transport properties. *Chem. Mater.*, 2011, 23 (19), 4331–4337.
- [130] G. B. Appetecchi, M. Montanino, A. Balducci, S. F. Lux, M. Winterb, S. Passerini, Lithium insertion in graphite from ternary ionic liquid-lithium salt electrolytes: I. electrochemical characterization of the electrolytes. *J. Power Sources*, 2009, 192 (2), 599–605.
- [131] G. A. Elia, U. Ulissi, F. Müller, J. Reiter, N. Tsiouvaras, Y. Sun, B. Scrosati, S. Passerini, J. Hassoun, A long-life lithium ion battery with enhanced electrode/electrolyte interface by using an ionic liquid solution. *Chem. Eur. J.*, 2016, 22 (20), 6808–6814.
- [132] D. MacFarlane, P. Meakin, J. Sun, N. Amini, M. Forsyth, Pyrrolidinium imides: a new family of molten salts and conductive plastic crystal phases. *J. Phys. Chem. B*, 1999, 103 (20), 4164–4170.
- [133] L. Xue, C. W. Padgett, D. D. DesMarteau, W. T. Pennington, Synthesis and structures of alkali metal salts of bis[(trifluoromethyl) sulfonyl]imide. *Solid State Sci.*, 2002, 4 (11), 1535–1545.
- [134] M. Montanino, M. Moreno, M. Carewska, G. Maresca, E. Simonetti, R. L. Presti, F. Alessandrini, G. Appetecchi, Mixed organic compound-ionic liquid electrolytes for lithium battery electrolyte systems. *J. Power Sources*, 2014, 269, 608–615.

## BIBLIOGRAPHY

---

- [135] J. Kalhoff, D. Bresser, M. Bolloli, F. Alloin, J. Sanchez, S. Passerini, Enabling LiTFSI-based electrolytes for safer lithium-ion batteries by using linear fluorinated carbonates as (co)solvent. *ChemSusChem*, 2014, 7 (10), 2939–2946.
- [136] V. Aravindan, J. Gnanaraj, S. Madhavi, H. Liu, Lithium-ion conducting electrolyte salts for lithium batteries. *Chem. Eur. J.*, 2011, 17 (51), 14326–14346.
- [137] J.-H. Shin, W. A. Henderson, S. Passerini, An elegant fix for polymer electrolytes. *Electrochim. Solid-State Lett.*, 2005, 8 (2), A125–A127.
- [138] P. Johansson, S. P. Gejji, J. Tegenfeldt, J. Lindgren, The imide ion: potential energy surface and geometries. *Electrochim. Acta*, 1998, 43 (10), 1375–1379.
- [139] J. Foropoulos Jr, D. D. DesMarteau, Synthesis, properties, and reactions of bis((trifluoromethyl)sulfonyl)imide,  $(\text{CF}_3\text{SO}_2)_2\text{NH}$ . *Inorg. Chem.*, 1984, 23 (23), 3720–3723.
- [140] M. Kerner, N. Pylahan, J. Scheers, P. Johansson, Ionic liquid based lithium battery electrolytes: fundamental benefits of utilising both TFSI and FSI anions? *Phys. Chem. Chem. Phys.*, 2015, 17 (29), 19569–19581.
- [141] A. Kumar, M. Deka, *Nanofiber Reinforced Composite Polymer Electrolyte Membranes*. InTech, 2010, 13–38.
- [142] C.-G. Wu, M.-I. Lu, C.-C. Tsai, H.-J. Chuang, PVdF-HFP/metal oxide nanocomposites: the matrices for high-conducting, low-leakage porous polymer electrolytes. *J. Power Sources*, 2006, 159 (1), 295–300.
- [143] A. M. Stephan, K. Nahm, Review on composite polymer electrolytes for lithium batteries. *Polymer*, 2006, 47 (16), 5952–5964.
- [144] A. M. Stephan, K. S. Nahm, T. P. Kumar, M. A. Kulandainathan, G. Ravi, J. Wilson, Nanofiller incorporated poly (vinylidene fluoride–hexafluoropropylene)(PVdF-HFP) composite electrolytes for lithium batteries. *J. Power Sources*, 2006, 159 (2), 1316–1321.
- [145] M. Stolarska, L. Niedzicki, R. Borkowska, A. Zalewska, W. Wieczorek, Structure, transport properties and interfacial stability of PVdF/HFP electrolytes containing modified inorganic filler. *Electrochim. Acta*, 2007, 53 (4), 1512–1517.
- [146] S. Chaurasia, R. Singh, S. Chandra, Thermal stability, complexing behavior, and ionic transport of polymeric gel membranes based on polymer PVdF-HFP and ionic liquid, [BMIM][BF<sub>4</sub>]. *J. Phys. Chem. B*, 2013, 117 (3), 897–906.
- [147] C. Sirisopanaporn, A. Fernicola, B. Scrosati, New, ionic liquid-based membranes for lithium battery application. *J. Power Sources*, 2009, 186 (2), 490–495.

## BIBLIOGRAPHY

---

- [148] A. Farnicola, F. Weise, S. Greenbaum, J. Kagimoto, B. Scrosati, A. Soletto, Lithium-ion-conducting electrolytes: from an ionic liquid to the polymer membrane. *J. Electrochem. Soc.*, 2009, 156 (7), A514–A520.
- [149] H. Wu, A. Zaccone, A. Tsoutsoura, M. Lattuada, M. Morbidelli, High shear-induced gelation of charge-stabilized colloids in a microchannel without adding electrolytes. *Langmuir*, 2009, 25 (8), 4715–4723.
- [150] H. Wu, M. Lattuada, P. Sandkühler, J. Sefcik, M. Morbidelli, Role of sedimentation and buoyancy on the kinetics of diffusion limited colloidal aggregation. *Langmuir*, 2003, 19 (26), 10710–10718.
- [151] J.-H. Shin, W. A. Henderson, S. Scaccia, P. P. Prosini, S. Passerini, Solid-state Li/LiFePO<sub>4</sub> polymer electrolyte batteries incorporating an ionic liquid cycled at 40 °C. *J. Power Sources*, 2006, 156 (2), 560–566.
- [152] H. Ye, J. Huang, J. J. Xu, A. Khalfan, S. G. Greenbaum, Li ion conducting polymer gel electrolytes based on ionic liquid/PVDF-HFP blends. *J. Electrochem. Soc.*, 2007, 154 (11), A1048–A1057.
- [153] J. W. Fergus, Ceramic and polymeric solid electrolytes for lithium-ion batteries. *J. Power Sources*, 2010, 195 (15), 4554–4569.
- [154] A. Guyomard-Lack, J. Abusleme, P. Soudan, B. Lestriez, D. Guyomard, J. L. Bideau, Hybrid silica-polymer ionogel solid electrolyte with tunable properties. *Adv. Energy Mater.*, 2014, 4 (8), 1301570.
- [155] F. Croce, G. Appetecchi, L. Persi, B. Scrosati, Nanocomposite polymer electrolytes for lithium batteries. *Nature*, 1998, 394 (6692), 456.
- [156] E. Quartarone, P. Mustarelli, A. Magistris, PEO-based composite polymer electrolytes. *Solid State Ionics*, 1998, 110 (1-2), 1–14.
- [157] D. Bamford, A. Reiche, G. Dlubek, F. Alloin, J.-Y. Sanchez, M. Alam, Ionic conductivity, glass transition, and local free volume in poly (ethylene oxide) electrolytes: single and mixed ion conductors. *J. Chem. Phys.*, 2003, 118 (20), 9420–9432.
- [158] B. Wang, S. Li, S. Wang, Correlation between the segmental motion and ionic conductivity of poly (ether urethane)-LiClO<sub>4</sub> complex studied by positron spectroscopy. *Phys. Rev. B*, 1997, 56 (18), 11503.
- [159] C. Schreiner, S. Zugmann, R. Hartl, H. J. Gores, Fractional Walden rule for ionic liquids: examples from recent measurements and a critique of the so-called ideal KCl line for the Walden plot. *J. Chem. Eng. Data*, 2009, 55 (5), 1784–1788.

## BIBLIOGRAPHY

---

- [160] I. Stepniak, E. Andrzejewska, A. Dembna, M. Galinski, Characterization and application of N-methyl-N-propylpiperidinium bis(trifluoromethanesulfonyl)imide ionic liquid-based gel polymer electrolyte prepared in situ by photopolymerization method in lithium ion batteries. *Electrochim. Acta*, 2014, 121, 27–33.
- [161] Y. Tong, M. Que, S. Su, L. Chen, Design of amphiphilic poly(vinylidene fluoride-co-hexafluoropropylene)-based gel electrolytes for high-performance lithium-ion batteries. *Ionics*, 2016, 22 (8), 1311–1318.
- [162] Y. Liao, C. Sun, S. Hu, W. Li, Anti-thermal shrinkage nanoparticles/polymer and ionic liquid based gel polymer electrolyte for lithium ion battery. *Electrochim. Acta*, 2013, 89, 461–468.
- [163] C. M. Costa, H. M. Rodrigues, A. Gören, A. V. Machado, M. M. Silva, S. Lanceros-Mendez, Preparation of poly (vinylidene fluoride) lithium-ion battery separators and their compatibilization with ionic liquid - a green solvent approach. *ChemistrySelect*, 2017, 2 (19), 5394–5402.
- [164] J. Kallhoff, G. G. Eshetu, D. Bresser, S. Passerini, Safer electrolytes for lithium-ion batteries: state of the art and perspectives. *ChemSusChem*, 2015, 8 (13), 2154–2175.
- [165] M. Nádherná, J. Reiter, J. Moškon, R. Dominko, Lithium bis (fluorosulfonyl) imide-PYR<sub>14</sub>TFSI ionic liquid electrolyte compatible with graphite. *J. Power Sources*, 2011, 196 (18), 7700–7706.
- [166] S. Chung, Y. Wang, L. Persi, F. Croce, S. Greenbaum, B. Scrosati, E. Plichta, Enhancement of ion transport in polymer electrolytes by addition of nanoscale inorganic oxides. *J. Power Sources*, 2001, 97, 644–648.
- [167] M. Wachtler, D. Ostrovskii, P. Jacobsson, B. Scrosati, A study on PVdF-based SiO<sub>2</sub>-containing composite gel-type polymer electrolytes for lithium batteries. *Electrochim. Acta*, 2004, 50 (2-3), 357–361.
- [168] G. Vijayakumar, S. Karthick, A. S. Priya, S. Ramalingam, A. Subramania, Effect of nanoscale CeO<sub>2</sub> on PVDF-HFP-based nanocomposite porous polymer electrolytes for Li-ion batteries. *J. Solid State Electrochem.*, 2008, 12 (9), 1135–1141.
- [169] P. Raghavan, X. Zhao, J.-K. Kim, J. Manuel, G. S. Chauhan, J.-H. Ahn, C. Nah, Ionic conductivity and electrochemical properties of nanocomposite polymer electrolytes based on electrospun poly (vinylidene fluoride-co-hexafluoropropylene) with nano-sized ceramic fillers. *Electrochim. Acta*, 2008, 54 (2), 228–234.
- [170] P. Raghavan, J.-W. Choi, J.-H. Ahn, G. Cheruvally, G. S. Chauhan, H.-J. Ahn, C. Nah, Novel electrospun poly (vinylidene fluoride-co-hexafluoropropylene)-in situ SiO<sub>2</sub> composite membrane-based polymer electrolyte for lithium batteries. *J. Power Sources*, 2008, 184 (2), 437–443.

## BIBLIOGRAPHY

---

- [171] H.-S. Jeong, S.-Y. Lee, Closely packed SiO<sub>2</sub> nanoparticles/poly (vinylidene fluoride-hexafluoropropylene) layers-coated polyethylene separators for lithium-ion batteries. *J. Power Sources*, 2011, 196 (16), 6716–6722.
- [172] V. Deimede, C. Elmasides, Separators for lithium-ion batteries: a review on the production processes and recent developments. *Energy Technol.*, 2015, 3 (5), 453–468.
- [173] K. J. Bishop, C. E. Wilmer, S. Soh, B. A. Grzybowski, Nanoscale forces and their uses in self-assembly. *Small*, 2009, 5 (14), 1600–1630.
- [174] S. Caimi, H. Wu, M. Morbidelli, PVdF-HFP and ionic liquid-based, free-standing thin separator for lithium-ion batteries. *ACS Appl. Energy Mater.*, 2018, 1 (10), 5224–5232.
- [175] A. Cingolani, D. Baur, S. Caimi, G. Storti, M. Morbidelli, Preparation of perfusive chromatographic materials via shear-induced reactive gelation. *J. Chromatogr. A*, 2018.
- [176] D. Saikia, A. Kumar, Ionic conduction in P(VDF-HFP)/PVDF-(PC+DEC)-LiClO<sub>4</sub> polymer gel electrolytes. *Electrochim. Acta*, 2004, 49 (16), 2581–2589.
- [177] X. Meng, H. Wu, G. Storti, M. Morbidelli, Effect of dispersed polymeric nanoparticles on the bulk polymerization of methyl methacrylate. *Macromolecules*, 2016, 49 (20), 7758–7766.
- [178] Z. Li, G. Su, X. Wang, D. Gao, Micro-porous P(VDF-HFP)-based polymer electrolyte filled with Al<sub>2</sub>O<sub>3</sub> nanoparticles. *Solid State Ionics*, 2005, 176 (23–24), 1903–1908.
- [179] W. Wiczorek, J. Stevens, Z. Florjańczyk, Composite polyether based solid electrolytes. the Lewis acid-base approach. *Solid State Ionics*, 1996, 85 (1–4), 67–72.
- [180] Y. Liu, J. Lee, L. Hong, In situ preparation of poly (ethylene oxide)-SiO<sub>2</sub> composite polymer electrolytes. *J. Power Sources*, 2004, 129 (2), 303–311.
- [181] B. Scrosati, F. Croce, S. Panero, Progress in lithium polymer battery R&D. *J. power sources*, 2001, 100 (1–2), 93–100.
- [182] F. Croce, L. Persi, B. Scrosati, F. Serraino-Fiory, E. Plichta, M. Hendrickson, Role of the ceramic fillers in enhancing the transport properties of composite polymer electrolytes. *Electrochim. Acta*, 2001, 46 (16), 2457–2461.
- [183] F. L. Maranhão, V. M. John, Bond strength and transversal deformation aging on cement-polymer adhesive mortar. *Constr. Build. Mater.*, 2009, 23 (2), 1022–1027.
- [184] R. Bayer, H. Lutz, Dry mortars. *Ullmann's Encyclopedia of Industrial Chemistry*, 2002.

## BIBLIOGRAPHY

---

- [185] R. Wang, P.-M. Wang, Action of redispersible vinyl acetate and versatate copolymer powder in cement mortar. *Constr. Build. Mater.*, 2011, 25 (11), 4210–4214.
- [186] J. Mirza, M. Mirza, R. Lapointe, Laboratory and field performance of polymer-modified cement-based repair mortars in cold climates. *Constr. Build. Mater.*, 2002, 16 (6), 365–374.
- [187] Y. Ohama, *Handbook of polymer-modified concrete and mortars: properties and process technology*. William Andrew, 1995.
- [188] A. Jenni, L. Holzer, R. Zurbriggen, M. Herwegh, Influence of polymers on microstructure and adhesive strength of cementitious tile adhesive mortars. *Cem. Concr. Res.*, 2005, 35 (1), 35–50.
- [189] M. U. K. Afridi, Z. U. Chaudhary, Y. Ohama, K. Demura, M. Z. Iqbal, Strength and elastic properties of powdered and aqueous polymer-modified mortars. *Cem. Concr. Res.*, 1994, 24 (7), 1199–1213.
- [190] R. Wang, D. Ma, P. Wang, G. Wang, Study on waterproof mechanism of polymer-modified cement mortar. *Mag. Concrete Res.*, 2015, 67 (18), 972–979.
- [191] X. Fan, L. Niu, Performance of redispersible polymer powders in wall coatings. *J. Adhes. Sci. Technol.*, 2015, 29 (4), 296–307.
- [192] L. Niu, L. Lei, Z. Xia, Redispersible polymer powder functionalized with NMA and its adhesive properties in dry-mixed coatings. *J. Adhes. Sci. Technol.*, 2013, 27 (13), 1432–1445.
- [193] F. Franks, Freeze-drying of bioproducts: putting principles into practice. *Eur. J. Pharm. Biopharm.*, 1998, 45 (3), 221–229.
- [194] A. Gharsallaoui, G. Roudaut, O. Chambin, A. Voilley, R. Saurel, Applications of spray-drying in microencapsulation of food ingredients: an overview. *Food Res. Int.*, 2007, 40 (9), 1107–1121.
- [195] K. Christensen, G. Pedersen, H. Kristensen, Preparation of redispersible dry emulsions by spray drying. *Int. J. Pharm.*, 2001, 212 (2), 187–194.
- [196] R. Baumann, S. D. Hofmann, H. Kuehn, M. Perello, Redispersible polymer powder from polyolefin dispersions and the use thereof in construction applications. 2014, uS Patent 8,802,767.
- [197] B. Bett, J. Richard, Water-redispersible powders of film-forming polymers with a "core/shell" structure. 1999, uS Patent 5,872,189.
- [198] X. Zhang, Y. Pei, D. Xie, H. Chen, Modeling spray drying of redispersible polyacrylate powder. *Drying Technol.*, 2014, 32 (2), 222–235.

## BIBLIOGRAPHY

---

- [199] K. Masters, *Spray drying handbook*. George Godwin Ltd., 1985.
- [200] A. Du Chesne, A. Bojkova, J. Gapinski, D. Seip, P. Fischer, Film formation and redispersion of waterborne latex coatings. *J. Colloid Interface Sci.*, 2000, 224 (1), 91–98.
- [201] N. B. Halima, Poly (vinyl alcohol): review of its promising applications and insights into biodegradation. *RSC Adv.*, 2016, 6 (46), 39823–39832.
- [202] P. P. Nampi, S. Kume, Y. Hotta, K. Watari, M. Itoh, H. Toda, A. Matsutani, The effect of polyvinyl alcohol as a binder and stearic acid as an internal lubricant in the formation, and subsequent sintering of spray-dried alumina. *Ceram. Int.*, 2011, 37 (8), 3445 – 3450.
- [203] D.-J. Jang, E. J. Jeong, H.-M. Lee, B.-C. Kim, S.-J. Lim, C.-K. Kim, Improvement of bioavailability and photostability of amlodipine using redispersible dry emulsion. *Eur. J. Pharm. Sci.*, 2006, 28 (5), 405 – 411.
- [204] L. M. Saija, M. Uminski, Water-redispersible low- $T_g$  acrylic powders for the modification of hydraulic binder compositions. *J. Appl. Polym. Sci.*, 1999, 71 (11), 1781–1787.
- [205] X. Chen, B. Zheng, J. Shen, Morphologies of polymer grains during spray drying. *Drying Technol.*, 2013, 31 (4), 433–438.
- [206] L. M. Calvo, J. Garuti Jr., Compositions for use in construction and methods of applying the same. 2012, uS Patent 8,187,375.
- [207] Z. Xia, X. Zhang, Y. Situ, H. Chen, C. Mei, Dry-powder latex coating for internal wall and its production. 2009, cN patent 101481584 A.
- [208] L. Hong, L. Chen, M. Ladika, Y. Li, L. Kim-Habermehl, R. Bergman, Impact of particle size and surface charge density on redispersibility of spray-dried powders. *Colloids Surf., A: Physicochem. Eng. Aspects*, 2014, 459, 274–281.
- [209] F. Wang, Y. Luo, B.-G. Li, S. Zhu, Synthesis and redispersibility of poly (styrene-block-n-butyl acrylate) core-shell latexes by emulsion polymerization with RAFT agent-surfactant design. *Macromolecules*, 2015, 48 (5), 1313–1319.
- [210] A. Rauh, M. Rey, L. Barbera, M. Zanini, M. Karg, L. Isa, Compression of hard core–soft shell nanoparticles at liquid–liquid interfaces: influence of the shell thickness. *Soft Matter*, 2017, 13 (1), 158–169.
- [211] D.-G. Yu, J.-J. Li, G. R. Williams, M. Zhao, Electrospun amorphous solid dispersions of poorly water-soluble drugs: a review. *J. Controlled Release*, 2018.
- [212] J.-J. Li, Y.-Y. Yang, D.-G. Yu, Q. Du, X.-L. Yang, Fast dissolving drug delivery membrane based on the ultra-thin shell of electrospun core-shell nanofibers. *Eur. J. Pharm. Sci.*, 2018, 122, 195–204.



## BIBLIOGRAPHY

---

- [213] X. Liu, Y. Yang, D.-G. Yu, M.-J. Zhu, M. Zhao, G. R. Williams, Tunable zero-order drug delivery systems created by modified triaxial electrospinning. *Chem. Eng. J.*, 2018.
- [214] C. C. Raines, P. H. Starmer, Free flowing particles of an emulsion polymer having SiO<sub>2</sub> incorporated therein. 1991, uS Patent 5,017,630.
- [215] J. A. Gonzalez-Leon, S.-W. Ryu, S. A. Hewlett, S. H. Ibrahim, A. M. Mayes, Core-shell polymer nanoparticles for baroplastic processing. *Macromolecules*, 2005, 38 (19), 8036–8044.
- [216] H. B. Yamak, Emulsion polymerization: effects of polymerization variables on the properties of vinyl acetate based emulsion polymers. in *Polymer Science*, InTech, 2013, 35–72.
- [217] E. Pungor, G. Horvai, *A practical guide to instrumental analysis*. CRC press, 1994.
- [218] Liquid-applied water impermeable products for use beneath ceramic tiling bonded with adhesives - Requirements, test methods, evaluation of conformity, classification and designation. Standard, European Standards, 2017.
- [219] T. G. Fox, Influence of diluent and of copolymer composition on the glass temperature of a polymer system. *Bull. Am. Phys. Soc.*, 1956, 1, 123.
- [220] P. C. Hiemenz, T. P. Lodge, *Polymer chemistry*. CRC press, 2007.
- [221] Z. Lu, X. Kong, C. Zhang, Y. Cai, Q. Zhang, Y. Zhang, Effect of polymer latexes with varied glass transition temperature on cement hydration. *J. Appl. Polym. Sci.*, 2017, 134 (36), 45264.
- [222] Z. Liu, H. Xiao, N. Wiseman, Emulsifier-free emulsion copolymerization of styrene with quaternary ammonium cationic monomers. *J. Appl. Polym. Sci.*, 2000, 76 (7), 1129–1140.
- [223] S. J. Bohórquez, J. M. Asua, Particle nucleation in high solids batch miniemulsion polymerization stabilized with a polymeric surfactant. *J. Polym. Sci., Part A: Polym. Chem.*, 2008, 46 (19), 6407–6415.
- [224] C. Gauthier, O. Sindt, G. Vigier, A. Guyot, H. Schoonbrood, M. Unzue, J. Asua, Reactive surfactants in heterophase polymerization. XVII. influence of the surfactant on the mechanical properties and hydration of the films. *J. Appl. Polym. Sci.*, 2002, 84 (9), 1686–1700.
- [225] A. Guyot, Advances in reactive surfactants. *Adv. Colloid Interface Sci.*, 2004, 108, 3–22.
- [226] C. Fang, Y. Jing, Z. Lin, The application research of environment-friendly reactive surfactants in acrylate emulsion pressure sensitive adhesives. *Int. J. Adhes. Adhes.*, 2017, 73, 1 – 7.

- [227] J. Mulvihill, A. Toussaint, M. D. Wilde, Onset, follow up and assessment of coalescence. *Prog. Org. Coat.*, 1997, 30 (3), 127 – 139.
- [228] L. Ehrl, M. Soos, M. Lattuada, Generation and geometrical analysis of dense clusters with variable fractal dimension. *J. Phys. Chem. B*, 2009, 113 (31), 10587–10599.

# List of publications

## Publications

- **Tracking of Fluorescently Labeled Polymer Particles Reveals Surface Effects during Shear-Controlled Aggregation**, S. Caimi, A. Cingolani, B. Jaquet, M. Siggel, M. Lattuada, M. Morbidelli, *Langmuir*, **2017**, 33(49), 14038-14044, (DOI: 10.1021/acs.langmuir.7b03054).
- **Preparation of perfusive chromatographic materials via shear-induced reactive gelation**, A. Cingolani, D. Baur, S. Caimi, G. Storti, M. Morbidelli, *Journal of Chromatography A*, **2018**, 1538, 25-33, (DOI: 10.1016/j.chroma.2018.01.025).
- **A hydrophobic low-complexity region regulates aggregation of the yeast pyruvate kinase Cdc19 into amyloid-like aggregates *in vitro***, E. Grignaschi, G. Gereghetti, F. Grigolato, M.R.G. Kopp, S. Caimi, L. Faltova, S. Saad, M. Peter, P. Arosio, *J. Biol. Chem.*, **2018**, 293(29), 11424-11432, (DOI: 10.1074/jbc.RA117.001628).
- **A methodologic approach for the selection of bio-resorbable polymers in the development of medical devices: the case of poly(L-lactide-co- $\epsilon$ -caprolactone)**, A. Cingolani, T. Casalini, S. Caimi, A. Klaue, M. Sponchioni, F. Rossi, G. Perale, *Polymers*, **2018**, 10(8), 851, (DOI: 10.3390/polym10080851).
- **PVdF-HFP and Ionic-Liquid-Based, Freestanding Thin Separator for Lithium-Ion Batteries**, S. Caimi, H. Wu, M. Morbidelli, *ACS Applied Energy Materials*, **2018**, 1(10), 5224-5232, (DOI: 10.1021/acsaem.8b00860).
- **Core-Shell Morphology of Redispersible Powders in Polymer-Cement Waterproof Mortars**, S. Caimi, E. Timmerer, M. Banfi, G. Storti, M. Morbidelli, *Polymers*, **2018**, 10(10), 1122, (DOI: 10.3390/polym10101122).

- **Effect of SiO<sub>2</sub> Nanoparticles on the Performance of PVdF-HFP/Ionic Liquid Separator for Lithium-Ion Batteries**, S. Caimi, A. Klaue, H. Wu, M. Morbidelli, *Nanomaterials*, **2018**, 8(11), 926, (DOI: 10.3390/nano8110926).
- **Mechanical phase inversion of Pickering emulsions via metastable wetting of rough colloids**, M. Zanini, A. Cingolani, C.-P. Hsu, A. Beltzung, S. Caimi, M. A. Fernandez-Rodriguez, D. Mitrano, G. Storti, L. Isa, *submitted*.
- **Recovery of Oil from Underground Electrical Cables**, S. Caimi, C. Colombo, R. Ferrari, G. Storti, M. Morbidelli, *submitted*.

## Publications in preparation

- **Aggregation of Stable Colloidal Dispersions under Short High-Shear Conditions**, J. Lu, S. Caimi, A. Cingolani, H. Wu, M. Morbidelli, *in preparation*.
- **Integrated conjugation and separation of IgG by reactive MCSGP**, N. Ulmer, S. Caimi, L. Volta, S. Vogg, M. Morbidelli, *in preparation*.

## Patents

- S. Caimi, H. Wu, M. Morbidelli, **Removal of oil from oil-filled power cables**, **2018**, filed.
- S. Caimi, G. Storti, M. Morbidelli, **A process for the preparation of a solid polymer electrolyte for batteries**, **2018**, filed.

# Conference and Poster proceedings

- **Tracking of fluorescently labelled polymer particles reveals surface effects during shear-controlled aggregation**, S. Caimi, A. Cingolani, B. Jaquet, M. Morbidelli, M. Lattuada, *ECIS*, 31<sup>st</sup> Conference of The European Colloid and Interface Society, **2017**, Madrid, Spain.
- **Synthesis of macro-porous materials via controlled aggregation of colloidal polymer particles**, A. Cingolani, M. Lorenz, S. Caimi, G. Storti, M. Morbidelli, *ECIS*, 30<sup>th</sup> Conference of The European Colloid and Interface Society, **2016**, Rome, Italy.
- **Macro-porous materials by controlled aggregation of colloidal polymer particles**, A. Cingolani, S. Caimi, G. Storti, M. Morbidelli, *Euro-MOF2015*, 1<sup>st</sup> European Conference on Metal Organic Frameworks and Porous Polymers, **2015**, Postdam, Germany.